BIMETALLIC-WAVEGUIDE COUPLED SENSORS

FOR TUNABLE PLASMONIC DEVICES

by

KUNAL K. TIWARI

Presented to the Faculty of the Graduate School of

The University of Texas at Arlington in Partial Fulfillment

of the Requirements

for the Degree of

DOCTOR OF PHILOSOPHY

THE UNIVERSITY OF TEXAS AT ARLINGTON

December 2015

ACKNOWLEDGEMENTS

Firstly, I would like to express my sincere gratitude to my supervising professor, Dr. Suresh C. Sharma, for his invaluable advising and for constantly motivating and encouraging me throughout the course of my dissertation. I will continue to follow the work ethics and leadership qualities that I have learnt from him in my future endeavors.

I would like to extend my sincere thanks to the dissertation committee, Dr. Nader Hozhabri, Dr. Ali Koymen, Dr. Alex Weiss, and Dr. Qiming Zhang, for taking out time from their busy schedule and providing their valuable suggestions. I am especially grateful to our collaborators, Dr. N. Hozhabri and Dr. Richard Chambers from Nanotechnology Research Center, for assistance with the thin film deposition. I would like to further extend my thanks to Douglas Coyne, for the technical support related to lasers in our lab, and the Physics department staff, Margie, Stacey, Bethany, and Angel, for their help all these years.

Finally, I cannot thank enough to my family members, especially my parents Dr. Krishna Chandra Tiwari and Gayatri Tiwari, and my grandma Asha Tiwari, for making me the person I am today and for their unconditional love and support throughout this journey. I want to express my deepest gratitude to my lovely sister Namrata Tiwari, and my adorable fiancée Deepika Singh, for their faith in me and their constant encouragement. Lastly but not the least, I would like to extend my sincere thanks to several of my friends, Ankit, Prasad, Karthik, Munuve, Digvijay, Budhyant, Azmat, Rakesh, Kinjal, Pranab, Brian, Sunil, and my room-mates who have been very supportive throughout my studies.

November 6, 2015

ABSTRACT

BIMETALLIC-WAVEGUIDE COUPLED SENSORS

FOR TUNABLE PLASMONIC DEVICES

Kunal K. Tiwari, PhD

The University of Texas at Arlington, 2015

Supervising Professor: Suresh C. Sharma

Surface plasmon resonance (SPR) has been a widely used optical technique for the real time and label free sensing applications in biomedicine, homeland security, food safety, environmental monitoring, etc. Surface plasmons (SPs) being extremely sensitive to the surrounding media, their characteristics can be modulated by tuning their dielectric environment. The unique property of the nematic liquid crystalline materials that their dielectric constant can be tuned by externally applied electric fields formed the basis for development of tunable plasmonic sensor for monitoring changes at metal/dielectric interfaces. Even though sensors with high sensitivity are available, it remains highly desirable to enhance sensor resolution and evanescent fields for many such applications. Through computer simulations and SPR measurements, we have investigated SPR sensor

architectures fabricated with single metallic, bimetallic, and bimetallic-waveguide coupled (Bi-WC) thin film structures. We present evidence for substantial enhancements in; resolution, sensitivity and decay length of evanescent fields from the developed Bi-WC SPR structures. A unique fixed detector Kretschman configuration optical system is employed, which is capable of carrying out pump-probe spectroscopy for simultaneous measurements of SPR related effects on PL characteristics of semiconductor quantum dots. Detailed results from these investigations will be presented and discussed.

TABLE OF CONTENTS

LIST OF ILLUSTRATIONS

LIST OF TABLES

Chapter 1

INTRODUCTION

It is known that the electro-optical properties of liquid-crystal (LC) and polymer-dispersed liquid crystal (PDLC) materials can be very significantly modified by incorporating small concentrations of metal nanoparticles (NPs) [1]. Display panels, light shutters, and smart windows are among devices that make use of the PDLC technology. That is why it becomes very important from the industrial point of view to investigate such LC and composite structures (PDLCs) doped with metallic NPs. As far as the physical mechanism(s) behind the observed changes in the electro optical properties of these materials is concerned, the local electric fields associated with surface plasmons (SPs) at Au-NPs/LC interface have been suggested and thereby investigated [2]. SPs are quanta of surface-charge density oscillations at a metal/dielectric interface, which when coupled with electromagnetic waves are called SP polaritons (SPPs) [3]. In the earliest stage of this dissertation research, we have reported the direct evidence of surface plasmons (SPs) in LC thin films containing small dispersions of gold (Au) NPs. These findings were important towards understanding the effects of doping PDLCs with Au NPs.

The SPs are extremely sensitive to the dielectric properties of the surrounding medium and so their characteristics can be modulated by tuning the dielectric environment at the interface. The unique property of the nematic liquid crystalline materials that their dielectric constant can be tuned by externally applied electric fields formed the basis for development of sensors for physical, chemical, and biomedical applications [4,5]. In cases, in which LC is one of the materials at the interface, SPR modulation can be accomplished

by externally applied electric fields. This idea has been utilized in our recent work [5], which shows relatively large changes in the SPPs resonance curves as functions of *ac* electric fields. The extremely high sensitivity of our device, may be useful in the design of certain types of surface plasmon polaritons (SPP) and LC based opto-electronic switches that respond to loss in reflectivity or change in the SPPs resonance angle.

The performance of a surface plasmon resonance based sensor can be characterized by; (i) sensitivity to changes in the refractive index of a medium at the interface, $S_n = \partial\theta_{SPR}/\partial n$, where θ_{SPR} is the SP resonance angle, (ii) figure-of-merit, FOM = S_n/FWHM (where FWHM is full-width at half-maximum of the resonance curve) and (iii) resolution, $\partial R/\partial\theta$. Though, SPP sensors with high sensitivity are available, it remains highly desirable to enhance sensor resolution, as well as, the evanescent fields for numerous applications. In a recently published work [6], we have investigated relative performance of six different sensors fabricated by using single metal, bi-metal, and bimetallic waveguide-coupled (Bi-WC) multilayer structures (quartz/Ag/Si_3N_4/Au). Several multilayer structures with varying thickness of intermediate Si_3N_4 waveguide layer (50-150 nm) were deposited in *class-100* clean room and evaluated as functions of the thickness of dielectric waveguide by SPR measurements and computer simulations. We present evidence for substantial enhancements in; the resolution, sensitivity and decay length of evanescent fields from the developed multilayered SPR structures.

With the long decay lengths of SP related fields from these sensors, it becomes possible to design experiments by which the influence of these fields on materials in contact with the sensor can be examined at such penetration depths. Computational

modelling of such multilayered thin film structures for its SPR characteristics can be efficiently achieved by using the famous transfer matrix method in MATLAB. The current research work involves parametric investigation of another dielectric material, hafnia (HfO_2), for its use as a waveguide media in such multilayered structure. In an ongoing project, as an important application of the developed Bi-WCSPR sensors, we also investigate the influence of strong plasmon related fields on the photoluminescence characteristics of semiconductor quantum dots (CdSe/ZnS).

Chapter 2

THEORY

2.1 Plasmons

The interaction of a material with electromagnetic fields is characterized by its dielectric constant ε. Materials with bound electrons get polarized in the direction of the applied field and hence, have a positive value for susceptibility χ (= ε - 1). Such materials are known as dielectrics, having a real, positive and isotropic value of ε. Whereas, certain materials like metals, respond by polarizing in a way so as to oppose the applied fields, as shown in figure 2.1. Such materials have a negative value for χ, and thereby a negative dielectric constant ε. Plasmons are described as collective oscillations of free electron gas density with respect to the fixed positive ions in metals, in response to certain optical frequencies. Thus it can be considered a quasiparticle as it arises from the quantization of plasma oscillations [3,7].

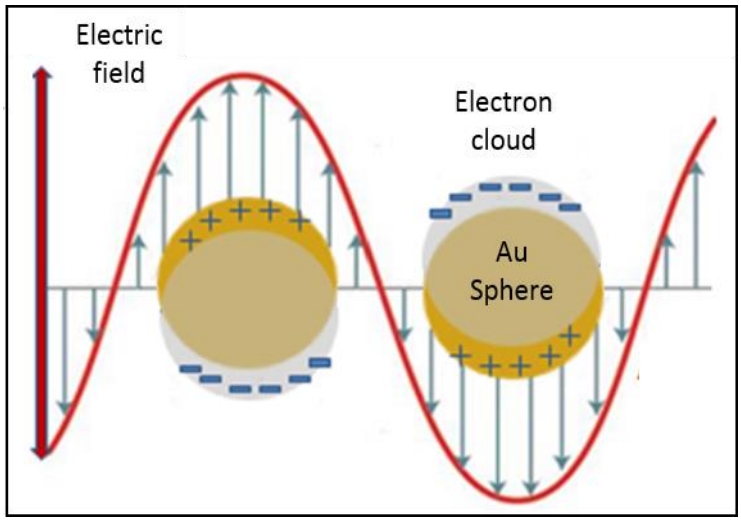

Figure 2.1 Schematic of plasmon oscillation for a metallic (Au) nanosphere, in presence of electromagnetic field of certain frequency [9]

All the interesting optical properties of metal nanoparticles, as reflected in their bright intense colors, are attributed to their interaction with light. The optical properties of metals can be explained by the Drude model, according to which their dielectric constant is a frequency dependent complex value, i.e., $\varepsilon(\omega) = \varepsilon_1(\omega) + i\varepsilon_2(\omega)$. In case of metals, plasmons play a significant role in terms of their optical properties. Incident radiation with frequency higher than the plasma frequency get transmitted, since the electrons cannot respond fast enough to the electric field of the photons so as to screen them. On the other hand, incident radiation with frequency lesser than the plasma frequency get reflected from the metal surface due to the screening effect of these electrons. Most of the metals have plasma frequency in ultra violet range, with energies within 5 to 15 eV, rendering their surface shiny and reflective in the visible range. The Lorentz harmonic oscillator model describes the equation of motion of a free electron, which combined with the Drude model (for dielectric constant) can give an estimate of the plasmon energy, as given below [8,9]

$$E_p = \hbar\sqrt{\frac{ne^2}{m\varepsilon_0}} = \hbar\omega_p \tag{2.1}$$

Here, ħ = reduced Plank constant, e = electron charge, n = conduction electron density, m = effective mass of electron, ε_o = permittivity of free space, and ω_p = plasmon frequency

Thus, plasmons can be excited as a consequence of interaction between photons and free electron gas density of metals, i.e. metal nanostructures. Depending upon whether a metal in contact with dielectric is in the form of a thin film or isolated nano-particles (NPs) incorporated into the bulk of a dielectric media, two types of plasmon excitations are of interest: 1) surface plasmons, and 2) bulk plasmons.

2.1.1 Surface Plasmons

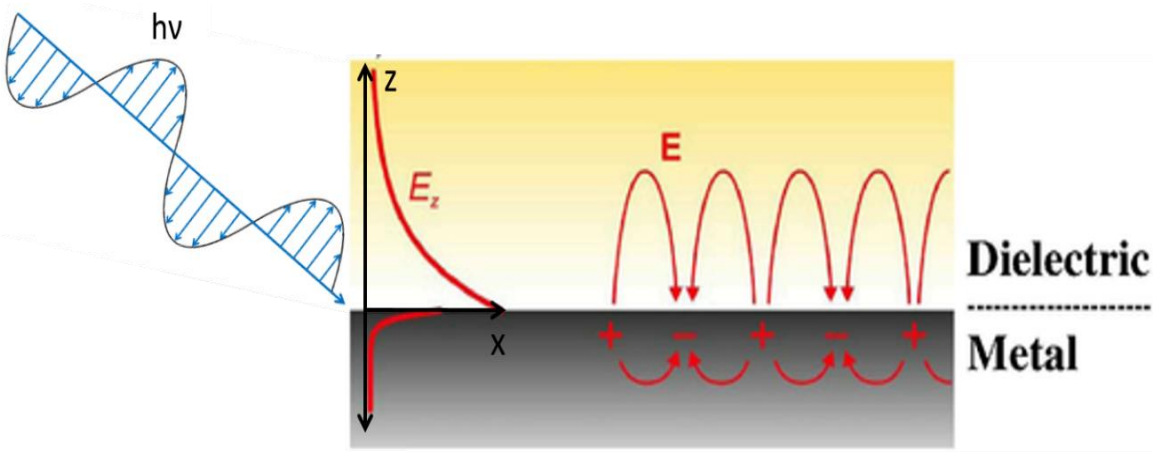

Figure 2.2 Schematic of incident radiation of a certain frequency exciting surface plasmons at a metal-dielectric interface [8]

Excitation of plasmons with the help of an incident radiation of certain frequency at the interface of two materials, for which the real part of the dielectric constant changes sign across the interface, are called surface plasmons (SPs). As discussed earlier, the dielectric function of metals being a frequency dependent complex value, the metal-dielectric interface can support the excitation of SPs at certain optical frequencies. At such an interface, it is possible to have normal components of electric fields in both media, which are both directed towards, or away from the interface, giving rise to the trapped surface mode. Figure 2.2 shows the schematic of an incident radiation of frequency ν, for which the dielectric function changes sign from positive to negative while travelling from dielectric to metal, resulting into collective excitation of SPs. The induced electromagnetic field on the metal surface decays exponentially into both the media (as shown in the figure), but tied to the oscillating surface charge density, propagates along the interface.

The coupled state between an elementary excitation and a photon is termed as polariton, whereas the term plasmon polariton signifies a coupled state between a plasmon and a photon. Thus, plasmons coupled with the incident electromagnetic fields that can propagate along the metal-dielectric interface, are termed as surface plasmon polaritons (SPPs). It can be excited by matching the momentum of the incident photons to that of the SPs or so called surface plasmon resonance (SPR) condition. These SPPs can propagate for long distances along the surface of metal until all the energy is lost, either due to absorption by the metal or radiated into the surrounding environment. The plasmon oscillations in case of metallic nano-structures as shown in figure 2.1, coupled with confined electromagnetic fields are called localized SPPs. Since the induced field is very sensitive to the variations of the dielectric medium in vicinity of the metal surface, any changes in the optical properties of the dielectric medium can be quantitatively analyzed for sensing purposes.

2.1.2 Derivation of bulk plasmons

Maxwell's equations describe the properties of the electric and magnetic fields under an electromagnetic perturbation. The electromagnetic waves associated with bulk plasmons and surface plasmons can be described by using the four Maxwells's equations listed below [3]:

$$\vec{\nabla}.\vec{E} = \frac{1}{\varepsilon_0}\rho \tag{2.2}$$

$$\vec{\nabla}.\vec{B} = 0 \tag{2.3}$$

$$\vec{\nabla} \times \vec{E} = -\frac{\partial \vec{B}}{\partial t} = -\mu\frac{\partial \vec{H}}{\partial t} \tag{2.4}$$

$$\vec{\nabla} \times \vec{B} = \mu_0 \vec{J} + \mu_0 \varepsilon_0 \frac{\partial \vec{E}}{\partial t} \tag{2.5}$$

The key to understand plasmons is the Drude model for dielectric constant of free electrons, described in the schematic shown in figure 2.3. The electrons in case of metals, though bound, are considered free to move with a uniform, immobile, positive ionic background of the atomic nucleus. When these free electrons are displaced, in presence of external electric fields, they create a polarization that acts as a restoring force, and thus are a collective harmonic oscillator. The harmonic frequency of such an electron system is known as plasma frequency ω_p. As a first step towards understanding SPR, we derive an expression for dielectric function of such conductors, as shown below:

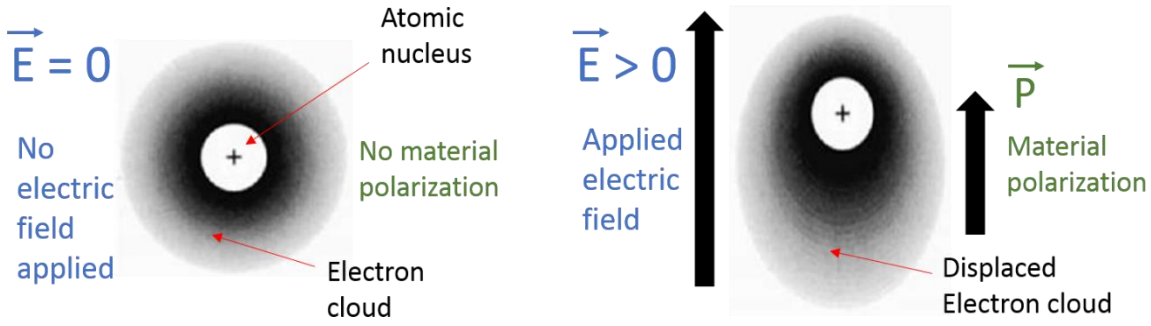

Figure 2.3 Drude's free electron model, showing displacement of free electrons in a metal as a response to applied electric field

Assuming a large number of free electrons moving in a positively charged background. As shown in the figure above, in presence of external field the electrons get displaced thereby polarizing the material, given as

$$\vec{p} = -ne\vec{\mu} \tag{2.6}$$

Here, $\vec{p}$ = polarization, n = number of free electrons, e = electron charge, and $\vec{\mu}$ = displacement of electrons

In case of free electrons, the displacement observes Newton's law:

Therefore, $$\vec{F} = nm\frac{d^2\vec{\mu}}{dt^2} \tag{2.7}$$

$$-en\vec{E} = nm\frac{d^2\vec{\mu}}{dt^2} = \frac{nm}{ne}\frac{d^2\vec{p}}{dt^2} \tag{2.8}$$

$$\vec{E} = \frac{m}{ne^2}\frac{d^2\vec{p}}{dt^2} \tag{2.9}$$

Now, since $\vec{E}$ is oscillatory in nature, lets take

$$\vec{E} = \overrightarrow{E_0}(r)e^{-iwt} \tag{2.10}$$

And so the polarization can be rewritten as,

$$\vec{p} = \overrightarrow{p_0}(r)e^{-iwt} \tag{2.11}$$

$$\frac{d^2\vec{p}}{dt^2} = -\omega^2\overrightarrow{p_0}(r)e^{-iwt} \tag{2.12}$$

Therefore, $$\vec{E}(\vec{r},\omega) = -\frac{\omega^2 m}{ne^2}\vec{p}(\vec{r},\omega) \tag{2.13}$$

$$\vec{p}(\vec{r},\omega) = -\frac{ne^2}{\omega^2 m}\vec{E}(\vec{r},\omega) \tag{2.14}$$

Now since the dielectric displacement is given as,

$$\vec{D} = \epsilon_0\vec{E} + \vec{p} = \varepsilon_0\varepsilon\vec{E} \tag{2.15}$$

We get, $$\vec{D}(\vec{r},\omega) = \varepsilon_0\vec{E}(\vec{r},\omega)\left[1 - \frac{ne^2}{\omega^2 m\varepsilon_0}\right] \tag{2.16}$$

Thus the frequency dependent dielectric permittivity can be obtained as,

$$\varepsilon(\omega) = 1 - \frac{ne^2}{m\varepsilon_0}\left(\frac{1}{\omega^2}\right) \tag{2.17}$$

Where, the plasma frequency is defined as,

$$\omega_p^2 = 1 - \frac{ne^2}{m\varepsilon_0} \tag{2.18}$$

Therefore, $$\varepsilon(\omega) = 1 - \left(\frac{\omega_p^2}{\omega^2}\right) \quad (2.19)$$

Here, $\varepsilon(\omega)$ = frequency dependent dielectric permittivity, ω = frequency of applied electric field, ω_p = plasma frequency, m = mass of the electron, ε_0 = free space dielectric permittivity

An important case to be noted over here is, when $\omega < \omega_p$, the dielectric function becomes negative, i.e. $\varepsilon(\omega) < 0$.

Now, in order to determine the dispersion relation, we explore the simple equation connecting frequency and wavelength, i.e.

$$\nu = f \bullet \lambda \quad (2.20)$$

Also, using $\omega = 2\pi f$ and $k = \frac{2\pi}{\lambda}$, we get

$$k = \frac{\omega}{\nu} = \frac{\omega}{c}\sqrt{\mu\varepsilon} \quad (2.21)$$

(since, the phase speed in medium is $\nu = \frac{c}{\sqrt{\mu\varepsilon}}$)

In case of non-magnetic materials (for example glass), μ = 1. So, $\nu = \frac{c}{n}$ and the dielectric function is simply given by, $\varepsilon = n^2$. If the dielectric function ε of a material depends on ω, the material disperses light.

With the equation for frequency dependent dielectric permittivity, $\varepsilon(\omega)$, equation 2.21 can be rewritten as,

$$c^2k^2 = \omega^2 - \omega_p^2 \quad (2.22)$$

This equation represents the dispersion relation for the bulk plasmons propagating in the metallic film. It gives the time dependence of the electromagnetic wave (ω), and the spatial

variation (k). The nature for the dispersion relation of bulk plasmons in comparison with dispersion relation of free space ($\omega = ck$) is shown in figure 2.4.

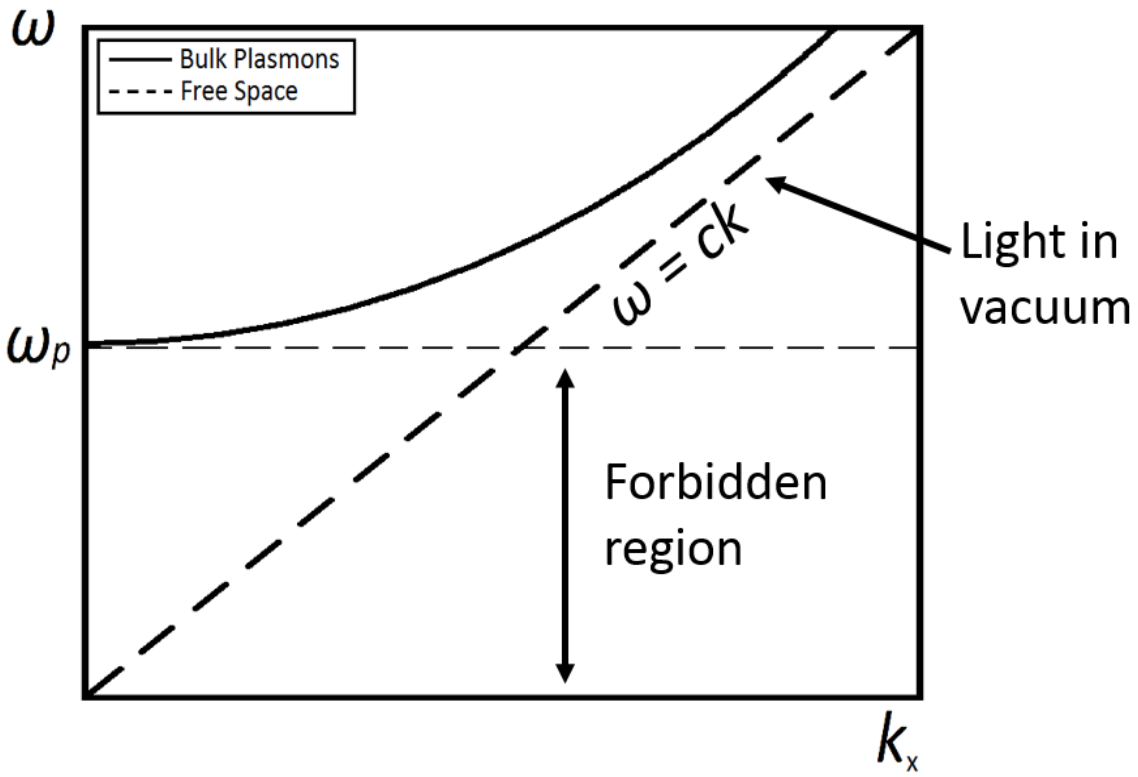

Figure 2.4 Dispersion relation for bulk plasmons [3,9]

It is evitable from the above graph, that the metal supports propagating waves for $\omega > \omega_p$ only, and the region below ω_p can be considered forbidden for wave propagation. In case of $\omega < \omega_p$, the wave vector k becomes imaginary and so the evanescent waves thus generated decay exponentially inside the metal. The bulk plasmons, that can exist even deep inside a metal, do not exist for $\omega < \omega_p$. There is an additional solution to Maxwell's equation for these low frequencies, termed as surface plasmons.

2.1.3 Derivation of surface plasmons

In order to excite surface plasmon modes, it is necessary to introduce a boundary separating two media of different dielectric constants, and look for solutions to Maxwell's equations at this boundary. This boundary enable the plasmons to form a surface mode, which can take frequencies lower than ω_p. Because of the requirement of the normal E fields to create surface charges, we need to consider only the p-polarized electromagnetic waves.

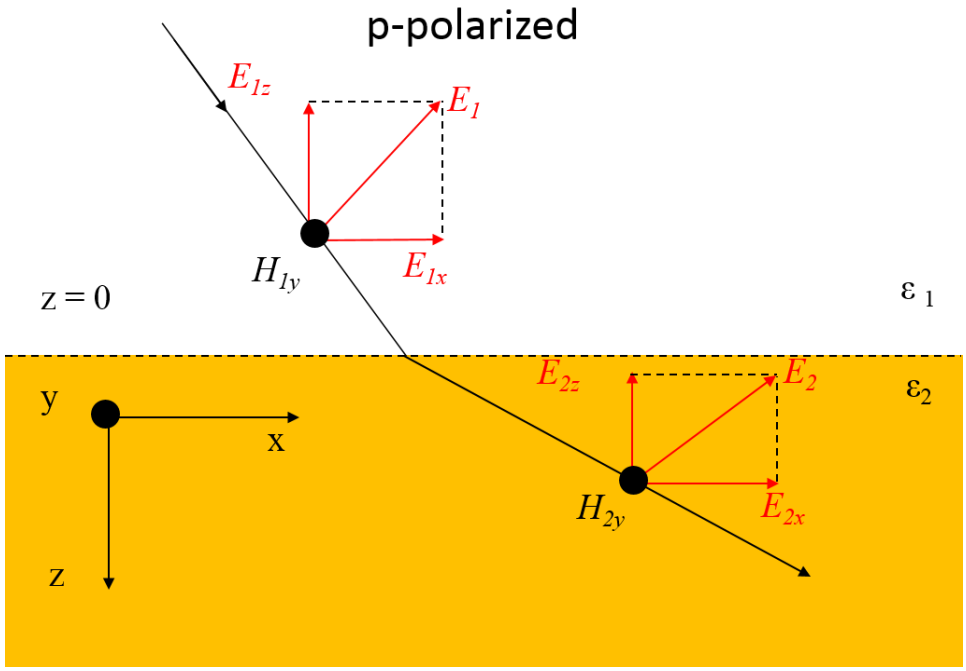

Figure 2.5 Electromagnetic field components for a p-polarized beam propagating from a denser to rarer medium [10]

The solution to Maxwell's equation that we are interested in is the evanescent wave solution. As shown in figure 2.5, consider an incident p-polarized wave propagating from a denser medium (ε_1) to a rarer medium (ε_2). Taking the x-y plane to be the plane of interface and the positive z half space as the rarer medium, then for the wave propagation in the x-direction only, the expression for the fields above and below the interface are:

$$E_1 = (E_{x1}, 0, E_{z1})e^{i(k_x x - \omega t)}e^{ik_{z1}z} \tag{2.23}$$

$$H_1 = (0, H_{y1}, 0)e^{i(k_x x - \omega t)}e^{ik_{z1}z} \tag{2.24}$$

$$E_2 = (E_{x2}, 0, E_{z2})e^{i(k_x x - \omega t)}e^{ik_{z2}z} \tag{2.25}$$

$$H_2 = (0, H_{y2}, 0)e^{i(k_x x - \omega t)}e^{ik_{z2}z} \tag{2.26}$$

If we apply Maxwell's equation (2.2), we get

$$\overrightarrow{E_{z1}} = -\overrightarrow{E_{x1}}\frac{k_x}{k_{z1}} \tag{2.27}$$

$$\overrightarrow{E_{z2}} = -\overrightarrow{E_{x2}}\frac{k_x}{k_{z2}} \tag{2.28}$$

In order to find the relation between H_y and E_x, we use Maxwell's equation (2.4) with $\mu = \mu_o$, giving us relationships between the field components (H_{y1}, H_{y2}), the permittivities (ε_1, ε_2) , and the normal component of the wave-vectors (k_{z1}, k_{z2}) in the two media:

$$H_{y1} = \frac{\omega E_{x1}\varepsilon_1\varepsilon_0}{k_{z1}} \tag{2.29}$$

$$H_{y2} = \frac{\omega E_{x2}\varepsilon_2\varepsilon_0}{k_{z2}} \tag{2.30}$$

Since the tangential H is continuous and so is tangential E, we apply boundary conditions at z = 0, i.e. $H_{y1} = H_{y2}$ and $E_{x1} = E_{x1}$, to get the most significant equation relating the relative permittivities and normal components of the wave vectors in both the media:

$$\frac{\varepsilon_1}{k_{z1}} = \frac{\varepsilon_2}{k_{z2}} \tag{2.31}$$

Also we get $k_{z1} = -i(k_x^2 - \varepsilon_1 k^2)^{\frac{1}{2}}$, which requires $k_x^2 > \varepsilon_1 k^2$ (2.32)

and $k_{z2} = i(k_x^2 - \varepsilon_2 k^2)^{\frac{1}{2}}$, which requires $k_x^2 > \varepsilon_2 k^2$ (2.33)

In order for the generated wave to be truly a trapped surface wave which decays exponentially into both media, we need to have $ik_{z1} > 0$ and $ik_{z2} < 0$. Therefore, both the $k_z s$ are imaginary with opposite signs and so ε_1 and ε_2 also have opposite signs.

The first required condition (2.32), tells us that the surface mode wave vector is greater than the maximum photon wavevector available in the dielectric, $\sqrt{\varepsilon_1}k$. Whereas, the second condition, for metal, is automatically met by having ε_2 negative.

By plugging the equations for k_{z1} and k_{z2} from 2.32 and 2.33 into 2.31, we get the dispersion relation for the propagating surface plasmon mode as follows:

$$k_x = k\left(\frac{\varepsilon_1\varepsilon_2}{\varepsilon_1+\varepsilon_2}\right)^{\frac{1}{2}} = \frac{\omega}{c}\left(\frac{\varepsilon_1\varepsilon_2}{\varepsilon_1+\varepsilon_2}\right)^{\frac{1}{2}} \tag{2.34}$$

Thus, for k_x to be real, the requirement for a propagating mode, with ε_2 negative, is that $|\varepsilon_2| > \varepsilon_1$.

In a special case (metal-air interface), for dielectric ε_1 = 1 and for metal from equation (2.19), $\varepsilon = 1 - \left(\frac{\omega_p^2}{\omega^2}\right)$, the dispersion relation for the surface plasmon modes modifies as below:

$$\omega^2 = \frac{\omega_p^2}{2} + (ck_x)^2 - \sqrt{(ck_x)^4 + \frac{\omega_p^4}{4}} \tag{2.35}$$

The dispersion curve obtained for surface plasmons (using equation 2.35), in relation with that of bulk plasmons (equation 2.22) and free space (ω = ck) are all plotted together, as shown in figure 2.6.

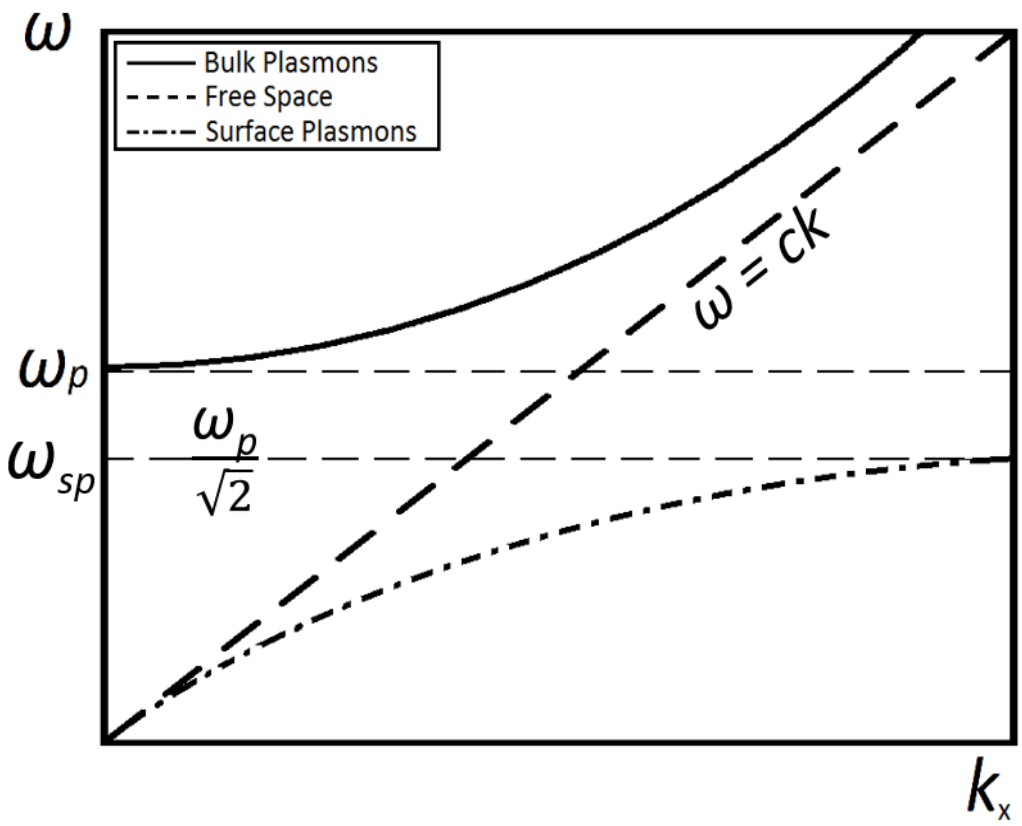

Figure 2.6 Dispersion relation for bulk plasmons, free-space light, and surface plasmons [3]

As observed in the above graph for dispersion of the three modes, the wave-vector of surface plasmon polaritons mode (k_{spp}) always lies to the right of the free space wave vector (k_o). Therefore, wavelength of the SPP mode (λ_{spp}) is always smaller than the wavelength of light in free space (λ_o), i.e. $\lambda_{spp} < \lambda_o$. This signifies that the illumination with free space radiation can never excite the surface plasmon modes directly. In other words, the free space radiation do not enough momentum to excite the surface plasmon. As the frequency (ω) increases, k_{spp} gets larger and larger, moving even further away from k_o. Also, as k_{spp} increases, the surface plasmon wavelength decreases, rendering the wave more tightly bound to the surface.

2.1.4 Excitation of surface plasmon polaritons (SPPs)

The SPPs are generated along the metal/dielectric interface by "manipulating" the wave vector of a p-polarized incident laser beam (electric field of the laser beam being parallel to the plane of incidence) such that its tangential component is larger than the wave vector of light in free space. The above mentioned manipulation requires that the metal/dielectric interface be chosen so as to fulfill the requirement for the existence of an interface mode, according to which one of the dielectric functions must be negative with absolute value exceeding that of the other medium. In order to meet the resonant surface plasmon excitation condition, the wave vector of the p-polarized incident beam must match with the wave vector of the excitations produced, as shown in figure 2.7.

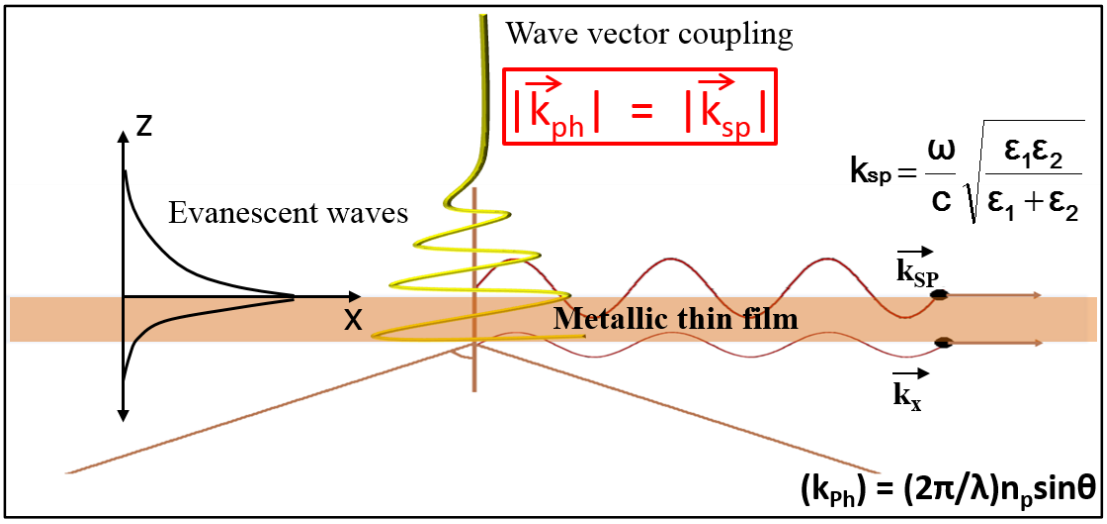

Figure 2.7 Schematic showing the coupling condition between a photon and a plasmon

Because of the energy momentum-mismatch, the incident radiation does not couple directly with the plasmon mode unless the coupling is facilitated by attenuated total reflection (ATR) in the Kretschmann or Otto configurations [11, 12]. The excitation of

SPPs has been achieved using several techniques, but the most versatile technique of exciting SPPs in planar geometries is the method of attenuated total reflection, which was independently demonstrated by Otto, and then by Kretschmann and Raether [11,12]. Most of the standard experimental systems often utilized to study the surface plasmon excitations uses one of the two configurations, as shown by the schematic in figure 2.8.

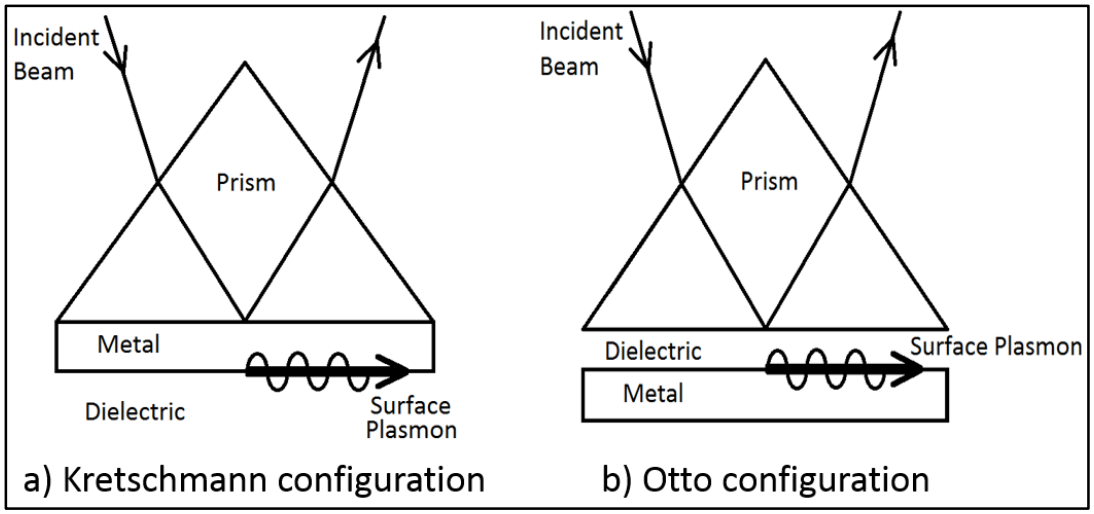

Figure 2.8 Schematic of Kretschmann and Otto configuration used for excitation of SPPs [11,12].

We have employed the Kretschmann configuration optical system equipped with (θ, 2θ) goniometer in all of our SPR measurements (detailed in section 4.1.1). These well-known configurations often utilize a high-index prism coated with thin film of a noble metal ($\leq$ 50 nm), which forms the interface with the sample (dielectric) under investigation. In case of Kretschmann configuration, the sample under investigation can be coupled to the metal film by spin-coating a film of a dispersion of the sample material over the metal film. Sometimes, it may be convenient to spin coat a dispersion of the sample material onto the metal coated glass slide, which can then be coupled to the prism by using a refractive index matched fluid. Depending upon which one of these methods is used to couple the

sample to the noble metal film, and assuming that in each case the refractive index of the prism is higher than that of the sample, ATR will be observed at the prism/sample and glass-slide/sample interfaces.

In the Otto configuration, on the other hand, there usually is a gap between the noble metal film and the sample. An air gap less than a few radiation wavelengths thick, for example, a gap of less than about 2 μm for the visible radiation, provides an evanescent tunnel barrier across which the radiation couples, from the totally reflected scenario, to excite the surface plasmon at the air (dielectric) metal interface. At sufficiently large separation between the two interfaces (gap width), the evanescent wave is only weakly coupled to the metal. The nature of the reflected intensity vs incident angle at the prism base varies strongly with the gap width. Whereas for small gap widths the resonance is broadened and shifted due to radiation damping, it disappears for large gap widths for which SPPs can no longer be excited. In certain cases the metal/dielectric interfaces may be formed when metal NPs are embedded in a dielectric medium, giving rise to localized surface plasmons (LSPs). The LSPs can be excited with light of appropriate frequency and polarization irrespective of the wave vector of the exciting light. They are characterized by discrete, complex frequencies and dielectric function of the NPs.

2.2 Liquid Crystals (LCs)

In 1888, an Austrian botanical physiologist, Friederich Reinitzer, found that a type of cholesterol benzoate exhibited an intermediate phase between the liquid and solid phases [13]. He observed that this cholesterol benzoate does not melt in the same manner as other compounds, and has two melting points. It transforms into a cloudy liquid (translucent) when heated to 145.5^{o} C and then into a completely clear (transparent) liquid when heated further, upto 178.5^{o} C. He also found that this phase transformation phenomena is reversible and the phase was later on termed as "liquid crystal" (LC) by a physicist Otto Lehmann in 1889 [14].

2.2.1 Liquid crystal physical properties

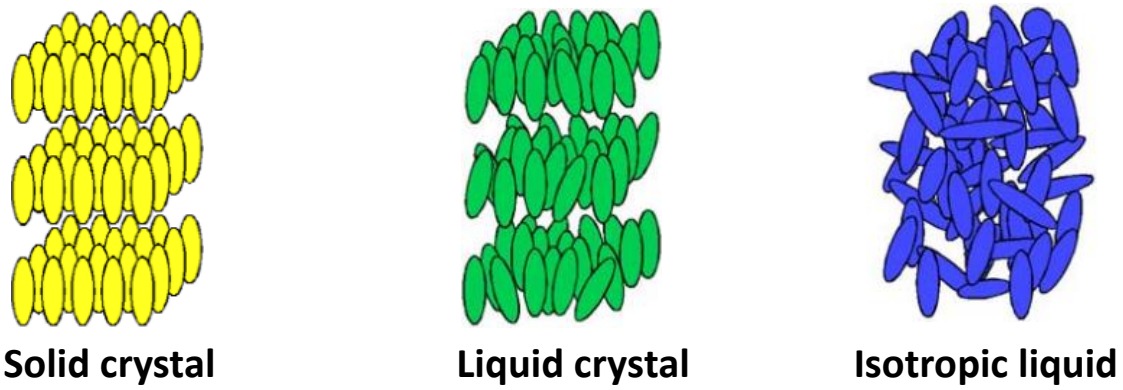

Figure 2.9 Schematic of constituent molecules of matter in three different phases

Liquid crystals are materials having properties intermediate between an isotropic liquid and a crystalline solid. Liquid crystals are wonderful materials since in this phase they retain the ability to flow like ordinary liquids, yet possess some physical properties which are characteristic of crystals (like molecular orientations). Materials that exhibit such unusual phases are often called mesogens (i.e., they are mesogenic) [15]. Liquid crystals

are significant for a variety of applications owing to; i) their mechanical properties, e.g., high fluidity, formation and coalescence of droplets, ii) variety of phases differing in structural and physical properties, and iii) similarity to crystals in exhibiting anisotropy in their optical, mechanical, electrical properties and presence of long-range orientational order. They are observed as thermodynamically stable phases between the crystalline solid and ordinary isotropic liquid states (thermotropic liquid crystals). They also possess properties not found in both of them.

2.2.2 Molecular shape anisotropy in LCs

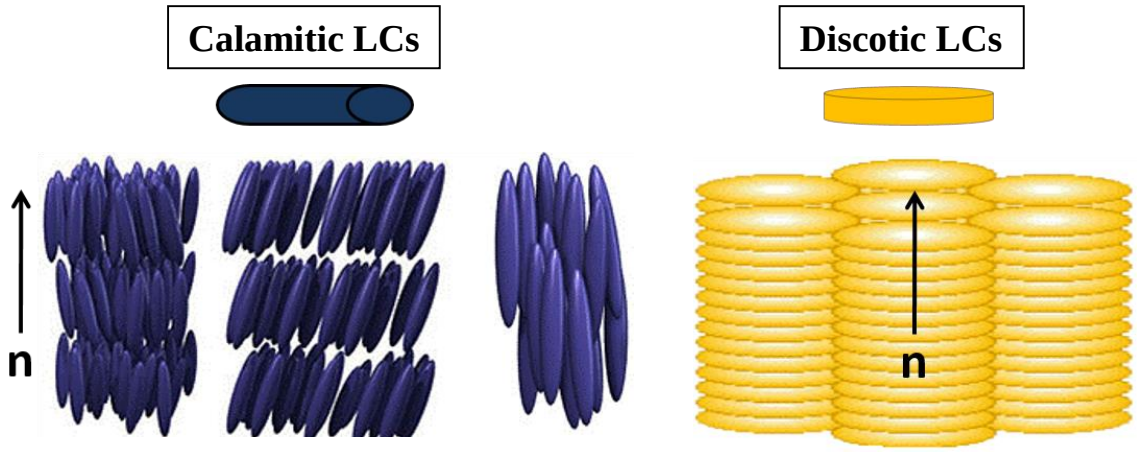

Figure 2.10 Molecular shape anisotropy in LCs classified into, i) Calamitic LCs and ii) Discotic LCs.

The most important property of a LC is their molecular anisotropy and the nature of this shape anisotropy falls within two categories; calamitic liquid crystals, which are shaped like rods, and discotic liquid crystals which are shaped like disks. The LC molecules are, however, directionally correlated; they are all aligned in an average direction of the molecular long axes defined by a unit vector termed as director, denoted by $\vec{\mathbf{n}}$ [16]. The calamitic LCs consist of elongated molecules where the direction of the long axis of the molecule is along the director, shown in figure 2.10. In case of discotic LCs, the axis

perpendicular to the plane of each molecule tends to orient along the director $\vec{n}$. LC molecules are centro-symmetric in nature since their physical properties are the same in the $+\vec{n}$ and the $-\vec{n}$ directions. Thus the directors in each case of LCs are apolar vectors, as $+\vec{n}$ and $-\vec{n}$ are equivalent. In other words, if the individual LC molecules carry permanent electric dipole, they will assemble in such a manner that the bulk dipole moment vanishes. Our research focus is mainly on **calamitic** type of LC as they're most important for their electro-optical applications.

2.2.3 Liquid crystal phases

The liquid crystals are classified into three categories depending upon the physical parameters and environment controlling their existence. As shown in the classification chart in figure 2.11, these distinct types of liquid crystals are; *lyotropic*, *polymeric*, and *thermotropic* [17].

The lyotropic type of liquid crystals are obtained by dissolving an appropriate concentration of a material in some solvent. In this case, the most important variable controlling the existence of the liquid crystalline phase is the amount of solvent (concentration). Examples of these kinds of molecules are soaps, detergents, lipids, etc. Lyotropic liquid crystals are mainly of interest in biological studies. Polymeric liquid crystal are compounds in which the mesogen is chemically attached to a reactive monomer, which can be polymerized to yield a high molecular weight compound with liquid crystalline properties. In general, this type of liquid crystals are characterized by much

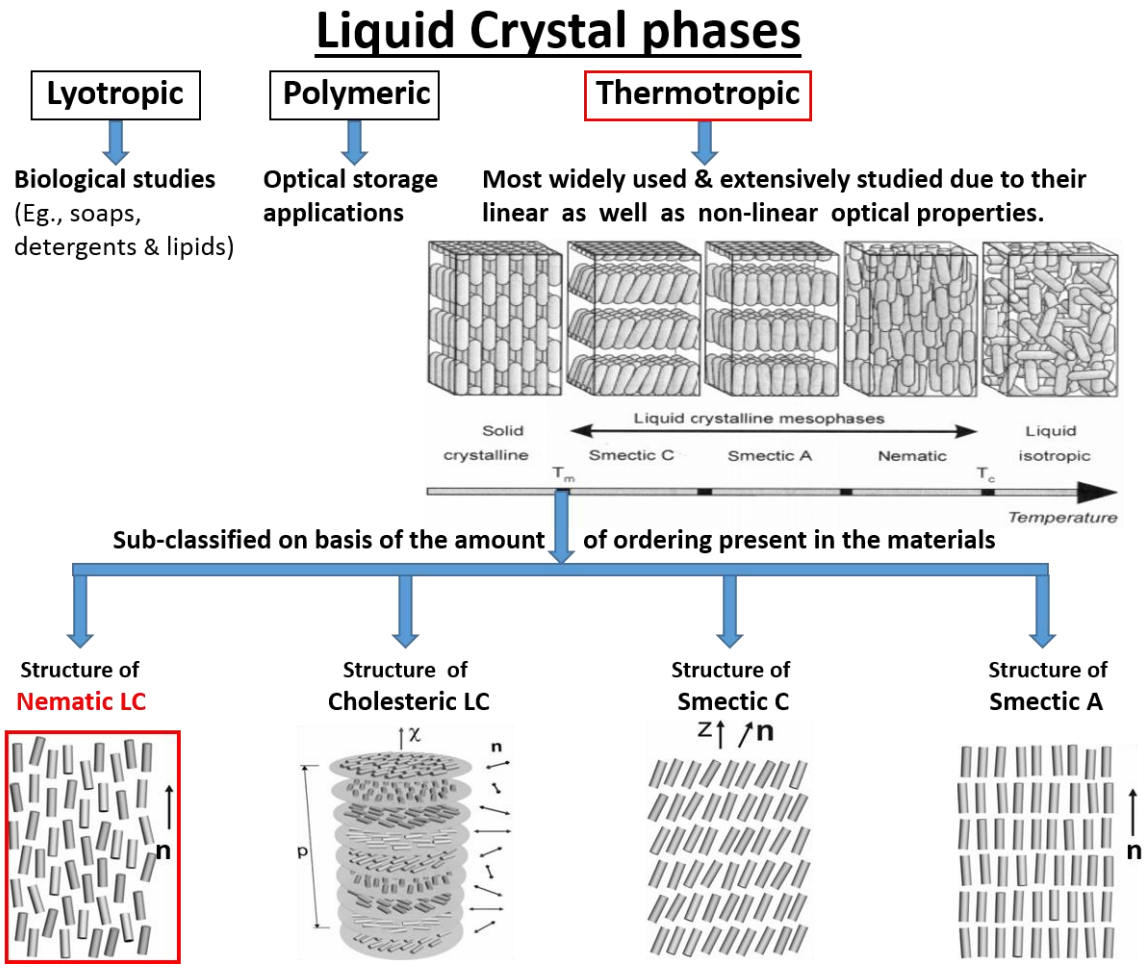

Figure 2.11 Schematic showing classification of various phases of liquid crystals [17, 18]

higher viscosity than that of monomers, and they are very useful for optical storage applications.

The third type, thermotropic liquid crystal, is the most widely used and extensively studied, for their linear as well as non-linear optical properties. They exhibit various liquid crystalline phases as a function of temperature. There are three main classes of thermotropic liquid crystals: nematic, cholesteric, and smectic. In accordance with the positional and directional arrangements (ordering), the smectic liquid crystals are again

sub-classified in several types. In this work, we primarily focus on calamitic type of liquid crystals only for their significant electro-optical applications. Below the melting point, T_m, the liquid crystals are solid, crystalline and anisotropic, whereas above the clearing point, Tc (where $T_c > T_m$) they appear as clear isotropic liquid. In the mesophase region, between T_c and T_m (as shown in the figure), the liquid crystal has the appearance of a milky liquid, but still exhibiting an ordered phase.

Smectic LCs, unlike nematics, possess positional order; that is, the position of the molecules is correlated in some ordered pattern. The two most common subclasses of smectic LC are; the smectic A phase and the smectic C phase. Smectic C phase is the first phase above melting point, T_m. Smectic C exhibits two dimensional ordering with molecules arranged with random deviations tilted to the plane of the layer. In case of smectic A, the molecular directors are aligned with random deviations, perpendicular to the plane of the layers. Cholesteric LCs, often called chiral nematic LCs, resemble nematic LCs in all physical properties except that the molecules tend to align in a helical manner, as depicted in figure 2.12. Lastly, nematic LC is the most disordered phase, having no translational order, but the molecules in this phase, on an average, orient about a particular direction ($\vec{n}$, as discussed earlier). The nematic phase appears with only a one-dimensional ordering (orientational), and are the last phase before the clearing point, T_c. All thermotropic LC phases are characterized by long-range orientational order of the mesophases, though the extent of translational order varies. In this dissertation, we focus on nematic LCs, which has much lower viscosity (~ 0.1 Pa • s), making them suitable for fast switching electro-optical applications.

2.2.4 Order parameter

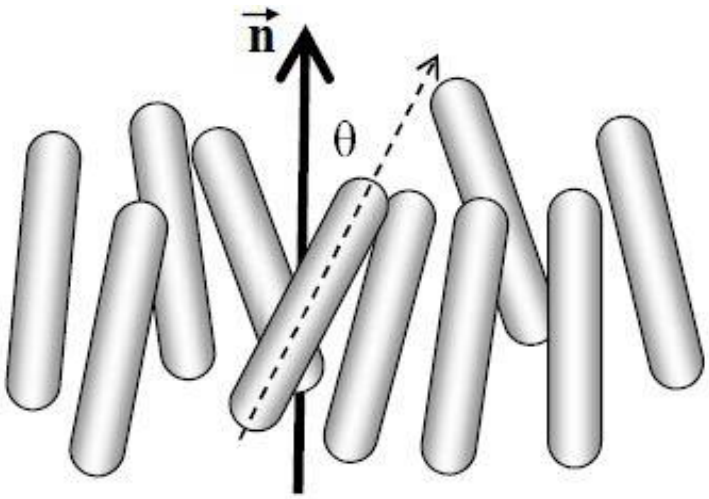

Figure 2.12 Orientational order between the nematic LC molecules. The nematic director is indicated by $\vec{\boldsymbol{n}}$ whereas, θ indicates the angle between the director and the individual molecular symmetry axis [17]

The physics of LCs is best described in terms of the so-called order parameters. In nematic phase, a molecular axis tends to point along a preferred direction, and an ensemble average of this preferred direction is called the nematic ensemble director, denoted by the unit vector $\vec{\mathbf{n}}$. An order parameter quantifies the degree or amount of orientational ordering in a liquid crystal. If we use the long axis of the molecule as a reference and denote it as k, the microscopic scalar order parameter $\boldsymbol{S}$ for a nematic liquid crystal can be constructed as follows:

$$\boldsymbol{S} = \frac{1}{2}\langle 3\left(\hat{k}\cdot\hat{n}\right)\left(\hat{k}\cdot\hat{n}\right) - 1\rangle$$

$$= \frac{1}{2}\langle 3\cos^2\theta - 1\rangle \qquad (2.36)$$

Here, θ is the angle made by the molecular symmetry axis with the director axis as shown in figure 2.12. The parenthesis ⟨ ⟩ denotes that the average is taken over the whole ensemble. This kind of order is usually termed as long-range order, and is called microscopic because it describes the average response of a molecule. In case if all the LC molecules are perfectly aligned as shown below in figure 2.13, i.e., $\theta_i = 0^o$ for all *i*, then the magnitude of order parameter $S = 1$. Whereas, in a liquid phase the system has no

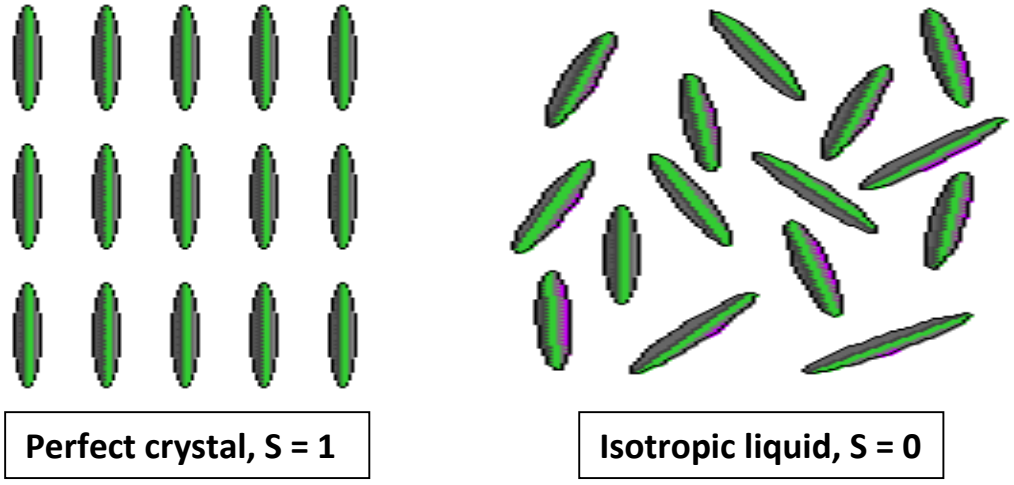

Figure 2.13 Schematic showing the variation in order parameter S, as the LC transforms from a crystalline to an isotropic liquid phase

orientational order, and so is expected to have any value with equal probability and the ensemble averaging gives $S = 0$.

The typical order parameter of nematic LCs is ~ 0.5 to 0.7. The temperature dependence of order parameter for all the thermotropic LCs can be described by the graph shown in figure 2.14, according to the Maier-Saupe mean field theory (1960) [19]. As the temperature increases, the order parameter decreases and jumps to zero at the nematic-isotropic transition temperature, or clearing temperature T_c.

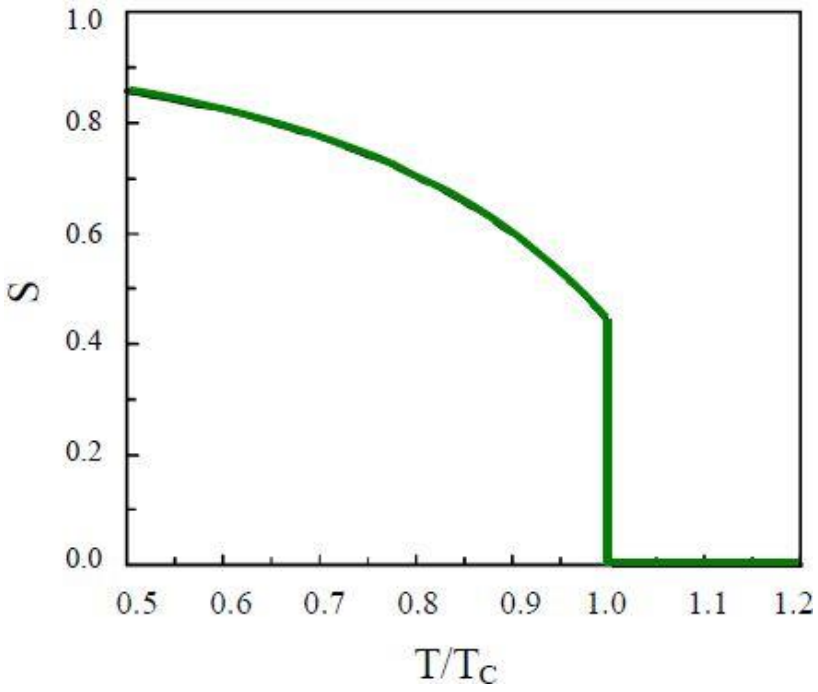

Figure 2.14 Temperature dependence of order parameter for nematic liquid crystal phase [19]

The order parameter is strongly correlated to the macroscopic properties of the LCs, such as dielectric/optical anisotropy, and so it has a lot of significance. For example, the optical birefringence (Δn) of LCs decrease with an increase in temperature, i.e. a decrease of the order parameter S.

2.2.5 Liquid crystal anisotropy and effects in electric fields

The unique phase ordering properties of LCs arise from their shape anisotropy, which manifests itself in other physical properties of the material such as dielectric constant and magnetic susceptibility. These physical parameters can have significantly different values (as many as three- one for each axis of symmetry), depending upon the direction of measurement. In case of nematic LCs, two of the directions are equivalent and so these materials are termed as uniaxial.

LC materials consist of polar molecules and the response of LC molecules to externally applied electric field is the major characteristic utilized in industrial applications. The ability of LC molecular director to align itself along the external field is caused by the electric nature of the molecules. Considering the case of nematic LC in an applied electric field, which changes the charge distribution in the molecules thereby inducing a permanent dipole moment. The induced polarization of nematic LC, in the weak field limit, is given as,

$$P = \varepsilon_o \chi E \tag{2.37}$$

where, ε_o is the permittivity of free space, and χ is the macroscopic electric susceptibility tensor of the material which is strongly associated to the orientational order [20]. Due to the shape anisotropy of LC molecule, electric susceptibility has two different values, $\chi_\perp$ and $\chi_\parallel$, depending on the direction of applied field. The difference between these two values is

$$\Delta\chi = \chi_\parallel - \chi_\perp \tag{2.38}$$

Which is expressed as the dielectric anisotropy

$$\Delta\varepsilon = \varepsilon_\parallel - \varepsilon_\perp \tag{2.39}$$

where, $\varepsilon = 1 + \chi$, and $\varepsilon_\parallel$, $\varepsilon_\perp$ are the dielectric permittivities parallel and perpendicular to the molecular symmetry axis, respectively. The induced dipole moment will serve to reorient LC director such that its symmetry axis is parallel ($\Delta\varepsilon > 0$) or perpendicular ($\Delta\varepsilon < 0$) to the applied field direction.

The electric displacement in presence of applied electric field is given as,

$$D = \varepsilon_o E + P \quad \text{or} \quad D = \varepsilon E \tag{2.40}$$

where, $\varepsilon = \varepsilon_o (1 + \chi)$, and 1 is a unit tensor. The component of applied electric field parallel to the director, i.e.

$$E_{\parallel} = E \bullet n \tag{2.41}$$

gives rise to an induced polarization, which is also parallel to the director

$$P_{\parallel} = \varepsilon_o \chi_{\parallel} E_{\parallel} \tag{2.42}$$

Similarly, in the case where the component of applied electric field is perpendicular to the director, i.e.

$$E_{\perp} = |E - (E \bullet n)\, n| \tag{2.43}$$

produces an Induced polarization acting perpendicular to the director

$$P_{\perp} = \varepsilon_o \chi_{\perp} E_{\perp} \tag{2.44}$$

Therefore, the total polarization at any instant is given by,

$$P = \varepsilon_o [\chi_{\perp} E + \Delta\chi (E \bullet n)\, n] \tag{2.45}$$

And, the electric energy per unit volume (energy density) can be written as

$$\mathrm{U} = -\frac{1}{2} \varepsilon_o [E^2 + \Delta\chi (E \bullet n)^2] = -\frac{1}{2} [\varepsilon_o E^2 + \Delta\varepsilon (E \bullet n)^2] \tag{2.46}$$

On taking average over an optical cycle, in case of interaction with optical fields, the energy density can be written as

$$\mathrm{U} = -\frac{1}{2} [\varepsilon_o \langle E^2 \rangle + \Delta\varepsilon \langle (E \bullet n)^2 \rangle] \tag{2.47}$$

Thus, in presence of an electric field, the nematic LC molecules will realign themselves in order to minimize this energy, specifically, the orientation dependent part of

the above two equations. In other words, the applied electric field does not increase the order of the LCs directly, instead it only causes the alignment of the director.

The material parameters of the LC mixture from E- and TL-series are listed below in table 2.1. The E44 LC mixture have been used in all the experiments presented in this dissertation.

Table 2.1 Material parameters of liquid crystal mixtures [85].

Parameters	**E-series**	**TL-series**
Mixture	E44	TL213
Viscosity (cSt, 20 ^{o}C)/(mm ^{2} s $^{-1}$, 20 ^{o}C)	47	49
$\Delta\varepsilon$ (1 kHz, 20 ^{o}C)	16.8	5.7
$\varepsilon\|\|$ (1 kHz, 20 ^{o}C)	22	10
Δn (589nm, 20 ^{o}C)	0.2627	0.239
n_o (589nm, 20 ^{o}C)	1.5277	1.527
$K_{11}/10^{-12}$ N (20 ^{o}C)	15.5	16.8
$K_{33}/10^{-12}$ N (20 ^{o}C)	28.0	22.0

2.3 Quantum Dots (QDs)

The history of colloidal semiconductor nanocrystals (NCs), also termed as "quantum dots" (QDs), starts back in the 1970s and 1980s, when the solid state physicists began investigating quantum structures. The earliest structure of such kind was quantum well [21, 22]. Since colloidal QDs were investigated by L. E. Brus et al. [23], they have attracted a keen attention as color saturated, highly luminescent and robust lumophors, due to their unique optical properties, such as facile bandgap tunability, wide absorption range,

spectral purity and photo-/chemical stability. The electronic characteristics of semiconducting QDs are closely related to the size and shape of the individual crystals. Fundamentally, the quantum confinement effect results in an increasing semiconductor bandgap with decreasing QD size as shown in figure 2.15, which allows size dependent tuning of the semiconductor photoluminescence emission wavelength throughout the visible spectrum. Smaller the size of the crystal, the larger the band gap, the greater the difference in energy between the highest valence band and the lowest conduction band becomes. This means that their electronic properties can be tuned by controlling their size. The unique optical and electronic properties of QDs are being exploited in a number of applications including flat panel displays and coloured lighting along with fluorescent imaging in biological and medical diagnostics. It is envisaged that QDs may replace many of the existing organic dyes and inorganic phosphors currently used in imaging, display and lighting devices.

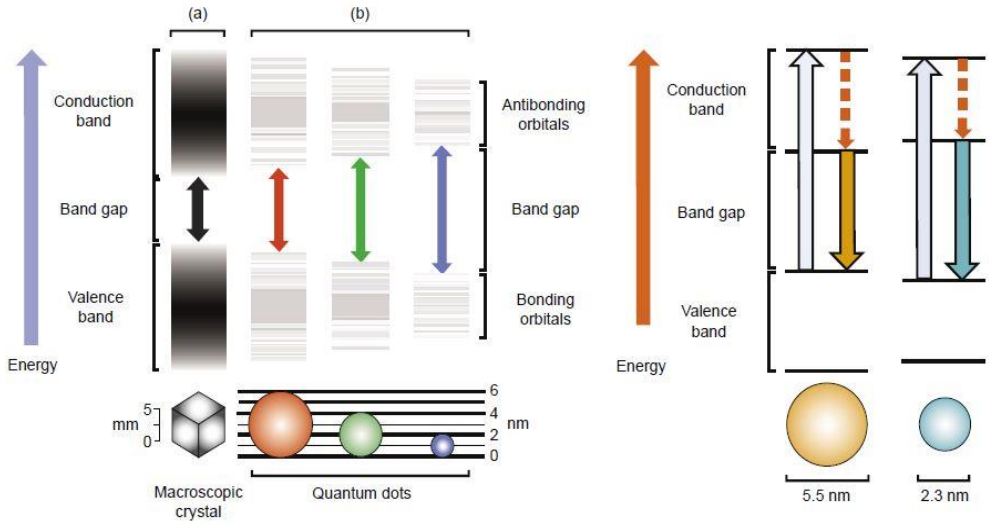

Figure 2.15 Size dependent luminescence of quantum dots. Larger QDs have narrow band gaps (red QD), comparing to small QDs (blue QD) [24]

Among various colloidal QDs based on II-VI (i.e., CdS, CdSe, CdTe, ZnSe, or ZnO), III-V (i.e., InAs and InP), IV-VI (i.e., PbSe and PbS), and IV (i.e., Si) compounds, II-VI QDs comprising cadmium and zinc chalcogenides have shown considerable progress in terms of high color purity (full-width at half maximum: 20~40 nm) and photoluminescence quantum efficiency (PL QE, above 70%) in the visible range [25]. Quantum confinement of electrons in semiconductor crystals with well-defined 3-dimensional nanoscale size is the origin of unique QD properties compared to conventional materials. In case of core-shell structures, the QD core consists of a few hundred to few thousand atoms of semiconducting material such as cadmium selenide (CdSe), indium phosphate (InP) or lead selenide (PbSe). This core is coated with a second semiconductor shell having a larger bandgap (usually zinc sulphide - ZnS), for the purpose of improving the optical properties of the nanocrystal. In order to further improve the utility of QDs, an extra polymer coating (an organic layer of surfactant molecules (ligands)) is attached that serves as a site for conjugation with biomolecule moieties. Due to its very sharp emission spectrum and high quantum efficiency, the QDs are ideal luminophor candidates for many opto-electronics and imaging applications.

2.3 Core/Shell Quantum Dots

The surface atoms in case of single crystal QDs are not completely bonded to the inner bulk, which results into the formation of dangling bonds at their surface. These dangling bonds act as trap sites for the charge carriers created during excitation of the crystal. These charge carrier trapping on QDs increases the probability of non-radiative recombination, resulting into a decrease in the fluorescence quantum efficiency. Coating

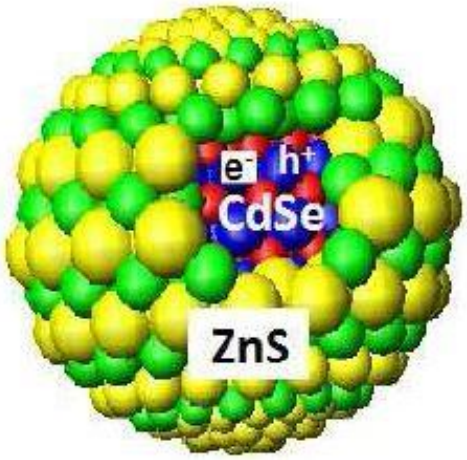

Figure 2.16 Representative image of a core-shell nano-crystal [26]

the surface with another material can substantially minimize the problem of charge carrier trapping. One way is to use the organic ligands to bind these dangling bonds, whereas the other way is to grow an epitaxial-like shell of inorganic material onto the core of the QDs [24, 25]. For example, usage of tri-n-octylphosphine oxide (TOPO) and trioctylphospine (TOP) to control the growth conditions and passivate the surface traps of high quality CdSe quantum dots have provided narrow size distribution and good crystallinity, but with a quantum yields of ~5-15%. The main difficulty in using such organic ligands is the simultaneous passivation of both, cationic and anionic surface traps. Instead, growing an epitaxial shell of inorganic semiconductor over the quantum dots can inhibit photo-oxidation and enables passivation of both anionic and cationic surface traps. The shell provides a physical barrier between the optically active core and the surrounding medium, thereby protecting the NCs from environmental changes, surface chemistry, and photo-oxidation effects. Figure 2.16 shows a representative image of such a core-shell nanocrystal.

Core-shell semiconducting nanocrystals (CSSNCs) are termed as materials having properties intermediate between those of small, individual molecules and those of bulk, crystalline semiconductors [25]. The core and shell are typically composed of type II-VI, IV-VI, and II-V semiconductors, having configurations such as CdS/ZnS, CdSe/ZnS, CdSe/CdS, and InAs/CdSe, wherein the conventional notation is: core/shell. The band alignment in the bulk materials of some of the most common semiconductors used for the QD NC synthesis are as shown in figure 2.17.

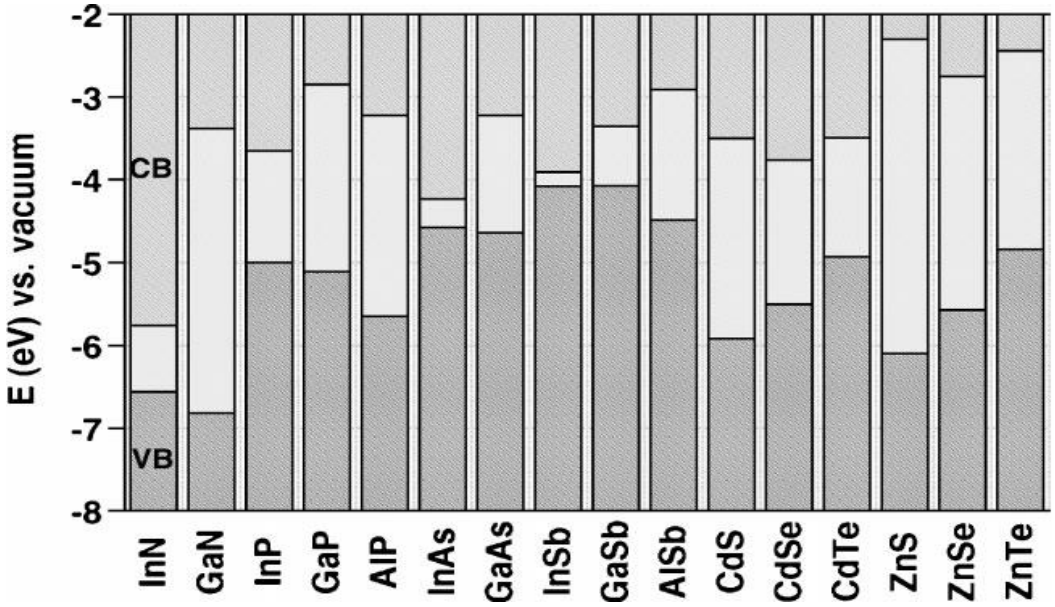

Figure 2.17 Electronic energy levels of selected III-V and II-VI semiconductors [27]. (VB: valence band, CB: conductance band)

These core-shell semiconducting NCs are classified into different types, depending on the bandgaps and the relative position of electronic energy levels of the involved semiconductors, as follows [25]:

2.3.1 Type-I Core/Shell Quantum Dots

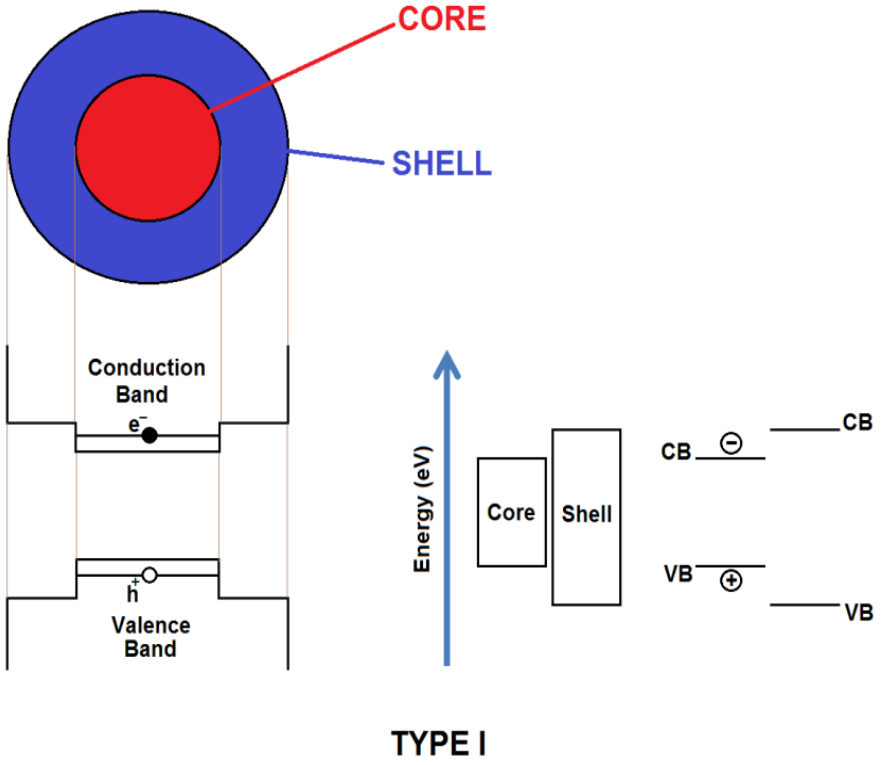

Figure 2.18 Schematic representation of energy level alignment in type-I core/shall QDs [27, 28]. Examples: CdSe/CdS, CdSe/ZnS, and InAs/CdSe.

In case of type-I semiconductor hetero-structures (where the core & shell are of different materials), the bandgap of the core is smaller than that of the shell. Thus, the valence and the conduction band edges of the core lie within the bandgap of the shell, and so the charge carriers tend to localize within the core of the quantum dot. In such structures, the shell is used to passivate the surface of core with a goal to improve its optical properties. The first published prototype system of this type was CdSe/ZnS. As seen in figure 2.18, the electron and hole of an exciton at the core/shell interface occupy energy states within the core (CdSe), corresponding to the lowest available energy separation. Therefore the emission wavelength due to radiative electron-hole recombination within the core is slightly red shifted compared to uncoated CdSe.

2.3.2 Reverse type-I Core/Shell Quantum Dots

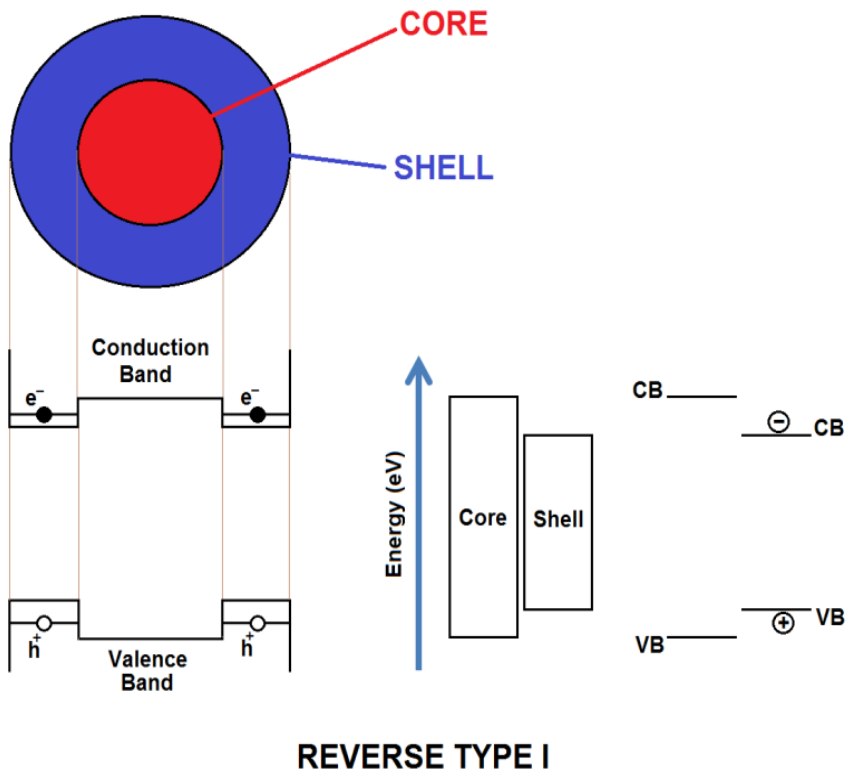

Figure 2.19 Schematic representation of energy level alignment in reverse type-I core/shell QDs [27, 28]. Examples: CdS/HgS, CdS/CdSe, and ZnSe/CdSe.

In this type of core/shell QD, a material of narrower bandgap is overgrown onto the core with wider bandgap. Thus the conduction and valence band edges of the shell lie within those of the core. The lowest available exciton energy separation occurs when the charge carriers are localized in the shell, thereby allowing us to tune the emission wavelength by changing the shell thickness. The most extensively analyzed systems of this type includes; CdS/HgS, CdS/CdSe, and ZnSe/CdSe.

2.3.3 Type-II Core/Shell Quantum Dots

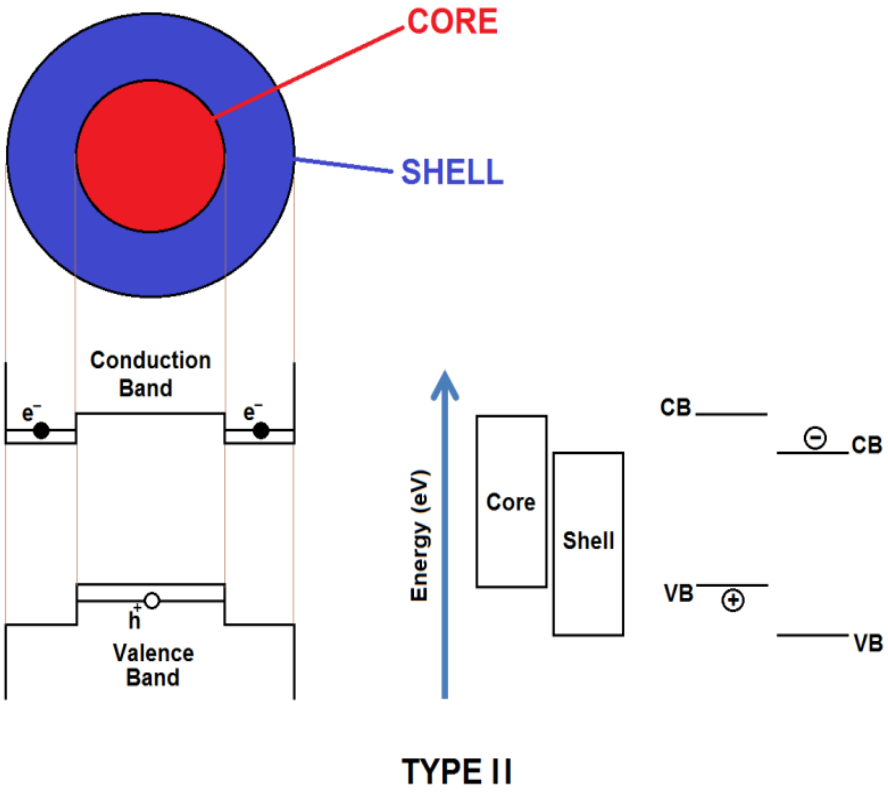

Figure 2.20 Schematic representation of energy level alignment in reverse type-II core/shell QDs [27, 28]. Examples: ZnTe/CdSe, CdTe/CdSe, CdS/ZnSe

In this type of configuration, the valence and conduction band edge of the core are both lower or higher than the band edges of the shell. Such a staggered band gap alignment leads to a smaller effective bandgap than each one of the constituting core and shell materials. Such NCs have been developed in particular for near-infrared emission, using for example CdTe/CdSe or CdSe/ZnTe. The lowest energy separation between the electron and the hole will occur when the hole is confined in the ZnTe core valence band whereas the electron is confined within the CdSe shell conduction band. The wavelength of the emitted radiation is determined by the energy difference of these occupied states, which is lower than the energy of either of the individual bandgaps. The photo-luminescence decay

times in this type of core/shell QD structure are strongly prolonged due to the lower overlap of the electron and hole wavefunctions, when compared to type-I systems.

2.4 Photoluminescence (PL)

The process by which any form of matter, organic or inorganic, absorb and subsequently re-radiates light, is described as photo-luminescence. The time interval elapsed between the absorption of excitation light and emission of re-radiated light classifies the photoluminescence phenomena into either fluorescence or phosphorescence. The phenomena is termed as phosphorescence in case if the emission of light persists for up to few seconds after the excitation source is turned off, whereas its termed as fluorescence if the emission of light persists for an extremely short duration only (~order of femto-second).

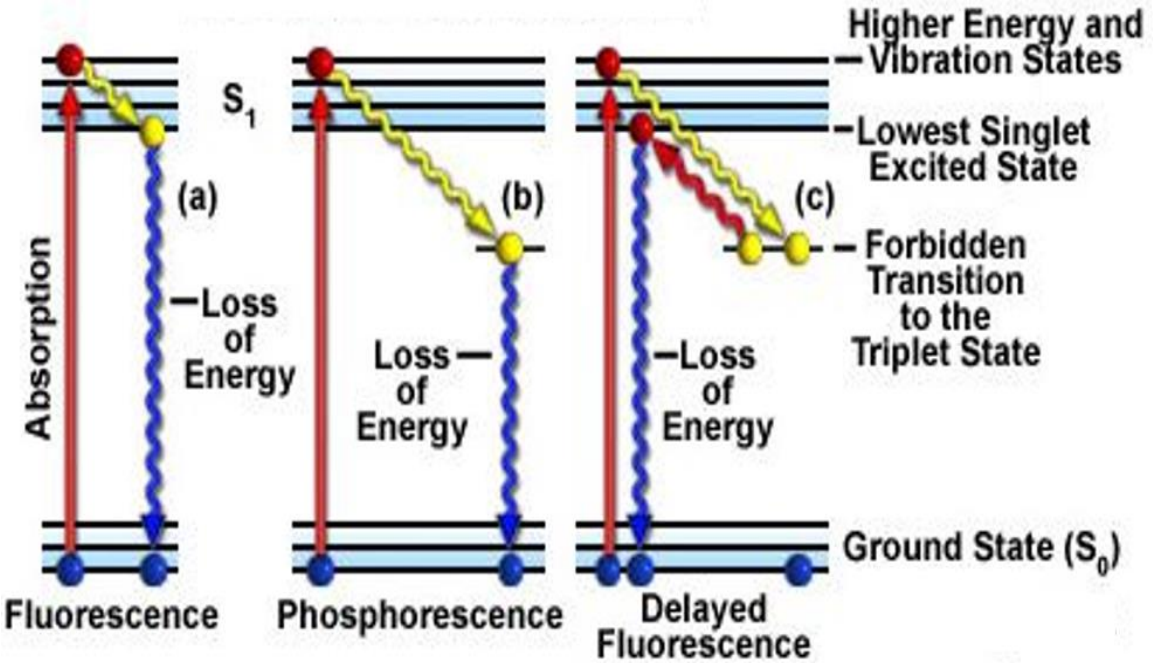

Figure 2.21 Classical Jablonski diagram describing absorption and emission phenomena [29]

Figure 2.21 shows a schematic representation of classical Jablonski diagram proposed by Alexander Jablonski in 1935, to describe the absorption and emission of light [30]. The singlet ground electronic states are shown as parallel bars labelled as S_0, whereas the singlet first excited states are shown as parallel bars labelled as S_1. Each electronic state is again subdivided into a series of closely spaced lines called vibrational energy levels, where a fluorophore can exist. Here, the solid sphere represents an electron whereas the vertical red lines indicate their transition from ground state to excited state. The electronic configuration of a molecule is described to be in ground state in the absence of any excitation source. A fluorophore can be excited to a higher vibrational energy level in the first excited state S_1 after absorbing a light energy corresponding to the difference of the two states. Before rapidly relaxing to the ground state, the fluorophore can undergo transition from upper to lower bars in S_1 by a process called vibrational relaxation or internal conversion, a process occurring in about a pico-second or even lesser time. Usually vibrational relaxation process occurs four orders of magnitude faster than the fluorescence lifetimes.

In certain cases, the excited electron makes a forbidden transition to an excited triplet state instead of relaxing to the lowest singlet state through vibrational interactions. The electron undergoes a spin conversion into the forbidden triplet state, a process commonly termed as intersystem crossing. The relaxation of electron from this forbidden triplet state to the ground state occurs with an emission of radiation that is considerably delayed, up to several seconds or more, a phenomena termed as phosphorescence [31]. The emission in case of phosphorescence (from these triplet states) occurs with a relatively

lower energy than in the case of fluorescence, thereby emitting photons of longer wavelengths. In some cases, the excited electrons trapped in the forbidden/triplet excited state may transit back into the lowest excited singlet state and then observe the normal course of relaxing to the ground state by emitting the fluorescent light. This action is termed as “delayed fluorescence” as it takes little longer (about a micro-second or two) than the usual fluorescence phenomena.

Chapter 3

MATLAB SIMULATIONS OF SURFACE PLASMONS

3.1 Computational details

The Transfer matrix method (TMM) is the most widely used technique for mathematical study of wave transmission in one-dimensional structures as it not only allows the calculations of reflection, transmission & emission spectra, but also facilitates evaluations of the guided modes and band diagrams for multilayered structures [32,33].The computational simulations are carried out by using TMM and MATLAB program. The TMM method treats Fresnel reflection and transmission at the interface of two media as a matrix, and the propagation of the light in a particular medium as another matrix. This allows for the multiplication of a stack of matrices to obtain the transmission and reflection by a stack of dielectric layers. However, it must be mentioned that the TMM simulations reflect results for multilayer structures having “ideal” macrostructures in the sense that the method does not take into account any deviations in materials’ properties on micro scale, like lattice defects, lattice mismatch at interfaces, and the microstructure of the interface itself. Nonetheless, the method is highly useful for predicting overall performance of devices having well defined macrostructures.

3.1.1 Single metal thin film on a dielectric

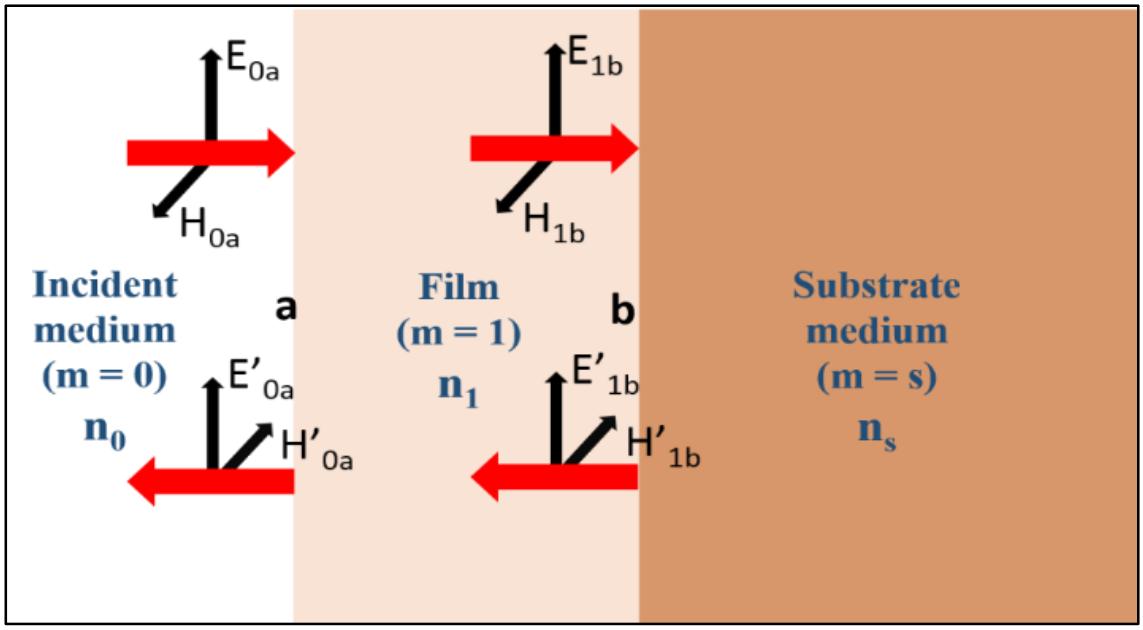

Figure 3.1. Schematic of electromagnetic wave propagating through a single thin film coated on a glass substrate.

We begin with simulations for the well-known and widely-used structure of a single metal thin film on quartz substrate. This exercise provides baseline results, which can be compared with published data and help assess the validity of the simulation program. As shown in figure 3.1, a monochromatic plane polarized beam is incident normally on the surface of a simple metal-on-glass substrate, such that the electric and magnetic field vectors are parallel to the interfaces. Amplitudes of the forward and backward propagating waves in a particular medium (labelled m) are denoted by E_m, H_m and E'_m, H'_m respectively. In this system, the incident medium is air, with a refractive index $n = n_0$ and the substrate medium is glass with a refractive index $n = n_s$. The thin film, having a refractive index $n = n_1$, forms simple boundaries **a** and **b** with air ($n = n_0$) and glass ($n = n_s$)

as shown in figure 3.1. We assume that the incident beam is reflected back from boundary b, between the film and the substrate, and no fields penetrate into the substrate.

Neglecting the common phase factors, the tangential components of the fields at interface b are:

$$E_b = E_{1b} + E'_{1b} \tag{3.1}$$

$$H_b = \eta_1 H_{1b} + \eta_1 H'_{1b} \tag{3.2}$$

Here, η_1 is the optical admittance of the thin film which is related to its refractive index n_1 by:

$$n_1 = \eta_1/\eta_0 \tag{3.3}$$

where $\eta_0 = (\frac{1}{377})\ \Omega^{-1}$, is the optical admittance of the free space. The optical admittance is usually normalized to be the same in magnitude as the refractive index of the film for normally incident electromagnetic waves. Using equations (3.1)-(3.3), the traveling wave expressions can be obtained as:

$$E_{1b} = \frac{1}{2}\left(\frac{H_b}{\eta_1} + E_b\right); \qquad E'_{1b} = \frac{1}{2}\left(-\frac{H_b}{\eta_1} + E_b\right) \tag{3.4}$$

$$H_{1b} = \eta_1 E_{1b} = \frac{1}{2}(H_b + \eta_1 E_b); \quad H'_{1b} = -\eta_1 E'_{1b} = \frac{1}{2}(H_b - \eta_1 E_b) \tag{3.5}$$

Equations (3.4) and (3.5) describe the amplitudes of the electric and magnetic fields at the interface b. The amplitude of the electromagnetic wave traversing through a material falls off exponentially as it moves away from the entrance boundary. Therefore the field amplitudes at boundary **a** have similar expressions except for the fact that their

exponentially decaying nature is governed by an appropriate phase factor, exp ($\pm i\phi_m$). The incoming (forward propagating) wave, which by the customary sign convention is assumed to be positive, is multiplied by exp ($+i\phi_m$) and the reflected (backward propagating) wave is multiplied by exp ($-i\phi_m$).

Here, ϕ_m is the phase factor given by;

$$\phi_m = k_{zm} d_m = (2\pi/\lambda)\,(n_m \cos\theta_m) \times d_m \tag{3.6}$$

(here, θ_m = angle of light travelling in medium m, k_{zm} = normal projection of wave vector in medium m, and d_m = thickness of layer m, and λ is the wavelength of the laser used).

In the present case of a single layer model, the only region where the fields are affected by the phase factor is within the thin film. Therefore $\phi_m = \phi_1 = \phi$ and so the E and H field amplitudes at the boundary **a** are given as:

$$E_{1a} = E_{1b}\, e^{i\phi} = \frac{1}{2}\left(\frac{H_b}{\eta_1} + E_b\right) e^{i\phi} \tag{3.7}$$

$$E'_{1a} = E'_{1b}\, e^{-i\phi} = \frac{1}{2}\left(-\frac{H_b}{\eta_1} + E_b\right) e^{-i\phi} \tag{3.8}$$

$$H_{1a} = H_{1b}\, e^{i\phi} = \eta_1 E_{1b}\, e^{i\phi} = \frac{1}{2}(H_b + \eta_1 E_b)\, e^{i\phi} \tag{3.9}$$

$$H'_{1a} = H'_{1b}\, e^{-i\phi} = -\eta_1 E'_{1b}\, e^{-i\phi} = \frac{1}{2}(H_b - \eta_1 E_b)\, e^{-i\phi} \tag{3.10}$$

Thus the overall field amplitudes at boundary a are:

$$E_a = E_{1a} + E'_{1a} = \frac{1}{2}\left(\frac{H_b}{\eta_1} + E_b\right) e^{i\phi} + \frac{1}{2}\left(-\frac{H_b}{\eta_1} + E_b\right) e^{-i\phi}$$

$$= \frac{H_b}{2\eta_1} e^{i\phi} + \frac{E_b}{2} e^{i\phi} - \frac{H_b}{2\eta_1} e^{-i\phi} + \frac{E_b}{2} e^{-i\phi}$$

$$= E_b \left(\frac{e^{i\phi} + e^{-i\phi}}{2}\right) + H_b \left(\frac{e^{i\phi} - e^{-i\phi}}{2\eta_1}\right)$$

$$= E_b \cos\phi + H_b \frac{i \sin\phi}{\eta_1} \tag{3.11}$$

and $H_a = H_{1a} + H'_{1a} = \frac{1}{2}(H_b + \eta_1 E_b)\, e^{i\phi} + \frac{1}{2}(H_b - \eta_1 E_b)\, e^{-i\phi}$

$$= \frac{H_b}{2} e^{i\phi} + \frac{E_b}{2}\eta_1 e^{i\phi} + \frac{H_b}{2} e^{-i\phi} - \frac{E_b}{2}\eta_1 e^{-i\phi}$$

$$= E_b \eta_1 \left(\frac{e^{i\phi} - e^{-i\phi}}{2}\right) + H_b \left(\frac{e^{i\phi} + e^{-i\phi}}{2}\right)$$

$$= E_b\, i\, \eta_1 \sin\phi + H_b \cos\phi \tag{3.12}$$

Equations (3.11) and (3.12) relate the electric and magnetic field amplitudes at boundaries **a** and **b** and can be represented by a 2x2 matrix:

$$\begin{bmatrix} E_a \\ H_a \end{bmatrix} = \begin{bmatrix} \cos\phi & i \sin\phi / \eta_1 \\ i\, \eta_1 \sin\phi & \cos\phi \end{bmatrix} \begin{bmatrix} E_b \\ H_b \end{bmatrix} \tag{3.13}$$

This equation (3.13) is termed as the characteristic matrix equation of the single thin film system. As there will be only a forward propagating wave in the substrate and no backward waves within the substrate, and since the tangential components of the fields are continuous across the boundary, the characteristic matrix equation (3.13) relates the tangential components at the incident interface with those transmitted through the final interface.

Thus, the input optical admittance of the single layer system (Y) can be expressed as the ratio of the amplitudes of the input fields at boundary **a**, i.e., $Y = \frac{H_a}{E_a}$. The reflection coefficient for the interface between incident medium and the thin film can thus be written as:

$$r = \frac{\eta_0 - Y}{\eta_0 + Y} \qquad \text{(where } \eta_0 = \eta_{air}\text{)}. \tag{3.14}$$

The reflectance for such a system can be easily calculated from:

$$\mathrm{R} = |r|^2 = \left(\frac{\eta_0 - Y}{\eta_0 + Y}\right)\left(\frac{\eta_0 - Y}{\eta_0 + Y}\right)^* \tag{3.15}$$

Here * indicates the complex conjugate of the value within the parenthesis.

Normalizing the characteristic matrix equation (3.13) to get a relationship between the electric field amplitude at boundary **a** with that at boundary **b** of the thin film system, we get the following form;

$$\begin{bmatrix} 1 \\ Y \end{bmatrix} = E_a = \begin{bmatrix} \cos\phi & i\sin\phi / \eta_1 \\ i\,\eta_1 \sin\phi & \cos\phi \end{bmatrix} \begin{bmatrix} 1 \\ \eta_{sub} \end{bmatrix} E_b \tag{3.16}$$

Here $Y = H_{norm} / E_{norm}$, where E_{norm} and H_{norm} are the normalized electric and magnetic fields at the boundary **a** thereby defining the optical admittance of the film.

3.1.2 Double metal thin film layered structure

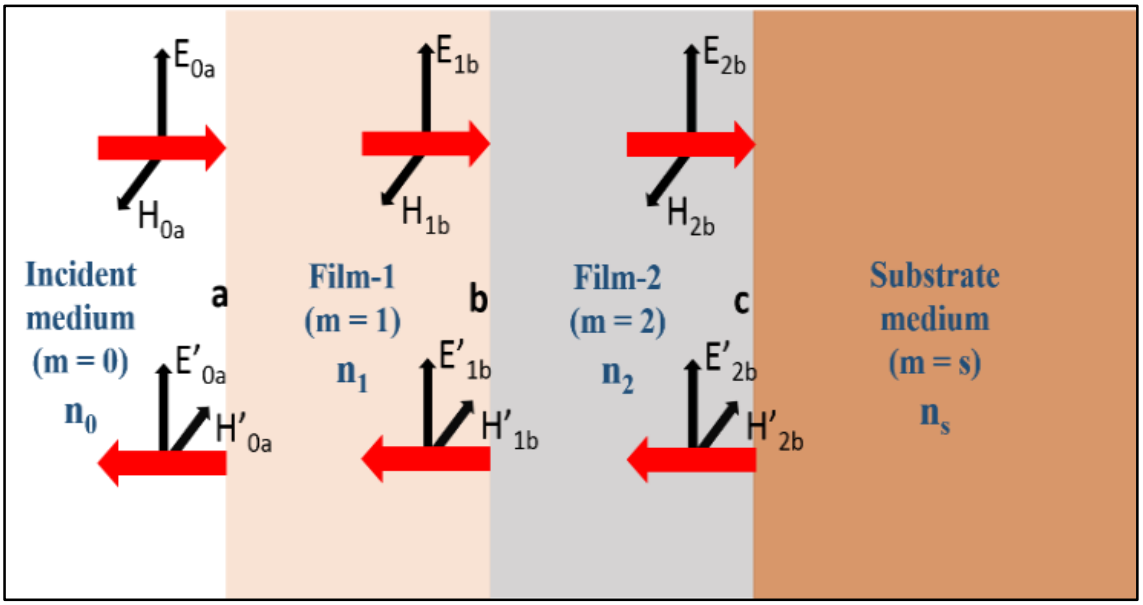

Figure 3.2. Schematic of electromagnetic wave propagating through a double film layered structure.

Figure 3.2 depicts schematic of electromagnetic waves traversing through three interfaces **a**, **b** and **c** of a double layered structure. Following the labeling schemes and sign conventions of the single layered structure, the characteristic matrix equation for film-2is given by:

$$\begin{bmatrix} E_b \\ H_b \end{bmatrix} = \begin{bmatrix} \cos\phi_2 & i\,\sin\phi_2/\eta_2 \\ i\,\eta_2 \sin\phi_2 & \cos\phi_2 \end{bmatrix} \begin{bmatrix} E_c \\ H_c \end{bmatrix} \tag{3.17}$$

Whereas, the characteristic matrix equation for the whole double layered system is:

$$\begin{bmatrix} E_a \\ H_a \end{bmatrix} = \begin{bmatrix} \cos\phi_1 & i\,\sin\phi_1/\eta_1 \\ i\,\eta_1 \sin\phi_1 & \cos\phi_1 \end{bmatrix} \begin{bmatrix} \cos\phi_2 & i\,\sin\phi_2/\eta_2 \\ i\,\eta_2 \sin\phi_2 & \cos\phi_2 \end{bmatrix} \begin{bmatrix} E_c \\ H_c \end{bmatrix} \tag{3.18}$$

The characteristic equation (3.18) after normalizing (as in the earlier case) can be re-written as:

$$\begin{bmatrix} E_{norm} \\ H_{norm} \end{bmatrix} = \begin{bmatrix} \cos\phi_1 & i\sin\phi_1/\eta_1 \\ i\,\eta_1\sin\phi_1 & \cos\phi_1 \end{bmatrix} \begin{bmatrix} \cos\phi_2 & i\sin\phi_2/\eta_2 \\ i\,\eta_2\sin\phi_2 & \cos\phi_2 \end{bmatrix} \begin{bmatrix} 1 \\ \eta_{sub} \end{bmatrix} \quad (3.19)$$

The optical admittance for this case is again defined as Y = H_{norm}/E_{norm}.

3.1.3 Generalization to a multilayered structure

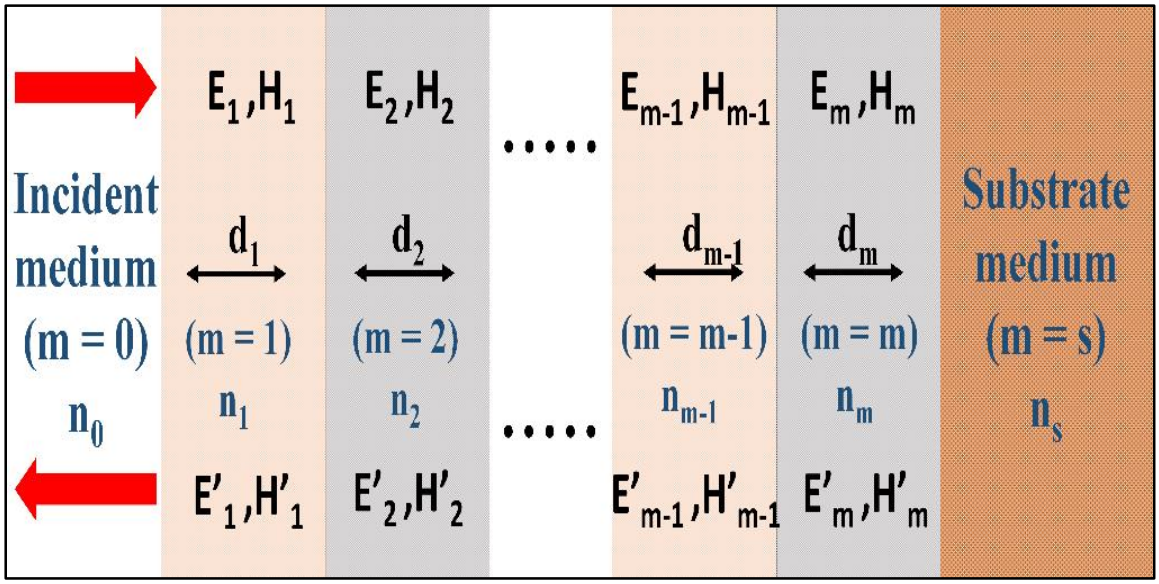

Figure 3.3 Schematic of EM waves propagating through a multilayered generalized structure.

Consider a stack of multilayered film structure with different geometrical thicknesses d_1, d_2,…. d_{m-1}, d_m , and having refractive indices as n_1, n_2, …. n_{m-1}, n_m , respectively. Here m indicates the number of layers in the stack, whereas m=0 and m=s are labelled as the incident and the substrate media respectively. The characteristic matrix

equation obtained by applying the boundary condition for the propagation of EM waves at the interface between the last (m) and second last (m-1) layer is;

$$\begin{bmatrix} E_{m-1} \\ H_{m-1} \end{bmatrix} = \begin{bmatrix} \cos\phi_m & i\,sin\phi_m / \eta_m \\ i\,\eta_m sin\phi_m & \cos\phi_m \end{bmatrix} \begin{bmatrix} E_m \\ H_m \end{bmatrix} \tag{3.20}$$

Again, here the refractive indices of each layers are related to their corresponding optical admittances by the relation:

$$n_m = \eta_m / \eta_0 \tag{3.21}$$

Thus the above relation can be generalized for an N-layered model as below:

$$\begin{bmatrix} E_0 \\ H_0 \end{bmatrix} = \prod_{m=1}^{N} M_m \begin{bmatrix} E_N \\ H_N \end{bmatrix} \tag{3.22}$$

$$\text{where, } M_m = \begin{bmatrix} \cos\phi_m & i\,sin\phi_m / \eta_m \\ i\,\eta_m sin\phi_m & \cos\phi_m \end{bmatrix} \tag{3.23}$$

$$\text{and } \begin{bmatrix} E_N \\ H_N \end{bmatrix} = \begin{bmatrix} 1 \\ \eta_s \end{bmatrix} E_s \tag{3.24}$$

The characteristic matrix over here (M) describes behavior of all the intervening layers.

The equation (3.24) can be written in terms of the optical admittance Y as:

$$E_N \begin{bmatrix} 1 \\ Y \end{bmatrix} = \begin{bmatrix} 1 \\ \eta_s \end{bmatrix} E_s \tag{3.25}$$

Where Y is the ratio of the total electric and magnetic field amplitudes, i.e., Y =H/E.

Thus for a generalized N-layered system shown in figure 3.3, the characteristic matrix equation can be obtained from the product of individual matrices in the respective order as given below:

$$\begin{bmatrix} E \\ H \end{bmatrix} = \left\{ \prod_{m=1}^{N} \begin{bmatrix} \cos\phi_m & i\,\sin\phi_m / \eta_m \\ i\,\eta_m \sin\phi_m & \cos\phi_m \end{bmatrix} \right\} \begin{bmatrix} 1 \\ \eta_s \end{bmatrix} \tag{3.26}$$

This equation can be employed to determine the reflectance of an assembly of any number of thin films and the transmittance for the same can be obtained from the relation T = 1 – R (for lossless media);

$$R = \left(\frac{\eta_0 E_{norm} - H_{norm}}{\eta_0 E_{norm} + H_{norm}} \right) \left(\frac{\eta_0 E_{norm} - H_{norm}}{\eta_0 E_{norm} + H_{norm}} \right)^{*} \tag{3.27}$$

and $$T = \frac{4\eta_0\, Re\, \eta_{sub}}{(\eta_0 E_{norm} + H_{norm})(\eta_0 E_{norm} + H_{norm})^{*}} \tag{3.28}$$

The MATLAB computational platform can be conveniently used for TMM as it can efficiently manipulate matrices. The reflectance of multilayered model and the corresponding reflection coefficient for a p-polarized (TM or TE) mode are formulated in MATLAB using the Fresnel's equation. From the generalized N-layer model, a characteristic matrix for a 3 layered structure is given as $M = M_1 * M_2 * M_3$, where M_1, M_2 and M_3 depicts the characteristic matrix for individual layers, i.e. for our multilayered structure, the inner metal (silver), waveguide (silicon nitride) and outer metal (gold), respectively (as discussed later).

3.2 Simulation results and discussion

In the present work, we carry out a systematic computational investigation of different SPR based sensors, viz., single metal (Au or Ag), bimetallic (Ag/Au) and waveguide (dielectric) coupled (Ag/Si_3N_4/Au), followed by supporting experimental results for the same. The metallic film in all the simulated results is assumed to be coated at the base of a high index prism, the same prism that is used in our experiments. The prism material N-SF11 (Edmund optics) has a high refractive index n = 1.7847 at a wavelength of 632.8 nm, which is the wavelength from 10mW He-Ne laser used in our experiments. All the reflectivity based SPR simulations (reflectance *vs* incident angle) presented in this work were carried out for the same high index prism, keeping the wavelength constant @ 632.8 nm for a TM (*p*-polarized) incident He-Ne laser. At the optical frequencies of interest, the dielectric constants of gold and silver are comprised of a large negative real number and a small imaginary number. Also at a wavelength of 630 nm, the experimental values of the dielectric constants vary from −10.8 + i1.47 to −12.8 + i1.36 for gold and −17.6 + i0.67 to −19.2 + i0.89 for silver [34]. The dielectric constant values for gold and silver used in all our simulations were -10.8 + i1.47 and -17.6 + i0.67 respectively, which were also used in our previously published work [2,5,35]. The performance of a sensor can be characterized by; (i) sensitivity to changes in the refractive index of a medium at sensor surface, $S_n = \partial\theta_{SPR} / \partial n$, where θ_{SPR} is the resonance angle, (ii) figure-of-merit, *FOM* = $S_n/FWHM$, where *FWHM* is full-width at half-maximum of the resonance curve and (iii) resolution, which scales with *FOM*, i. e., higher *FOM* corresponds to higher resolution.

Even though, SPP sensors with high S_n values are available, it remains highly desirable to enhance sensor resolution, as well as, the evanescent fields for numerous applications. In a recent publication, we had reported high sensitivity of an SPR sensor to *ac* electric field induced changes in the refractive index of nematic liquid crystal; this sensitivity ($\partial\theta_{SPR}/\partial n$) was actually 28-times higher than the sensitivity of similar known sensors [5]. It remains desirable to further enhance the sensitivity, resolution, and the surface plasmon polariton penetration depth for medical, environmental, and chemical applications. As it will become evident from the data presented in this work, in comparison to the single-metal (Au) sensor, our optimized multilayer structure sensor offers 7-times higher resolution, 13-times narrower FWHM, and much wider range of angles accessible for SPR measurements.

3.2.1 Simulation results for single metal based SPR sensor

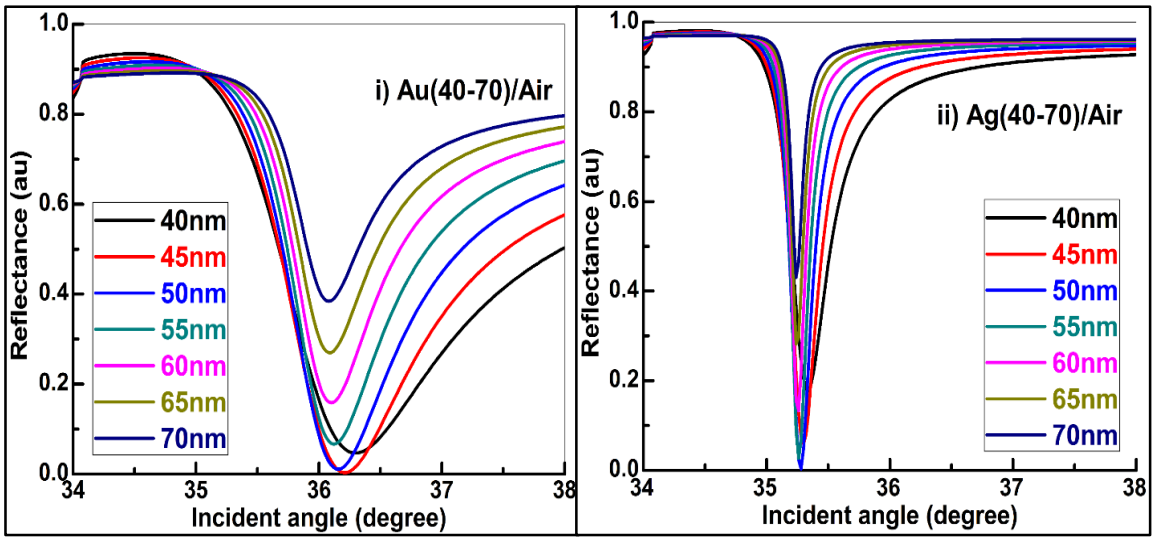

Figure 3.4 Reflectance vs angular curves for; i) Au film and ii) Ag film based single metal SPR sensor.

Figure 3.4 shows computed SPR curves for thin film Au and Ag, separately coated on quartz, SPR sensors with the metal film thickness varying from 40 nm to 70 nm. The angle of incidence at which minimum reflection occurs corresponds to the maximum energy loss due to excitation of surface plasmons and is identified by the surface plasmon resonance angle (θ_{SPR}). It is evident from these simulated results that the overall nature of the SPR curve can be dramatically affected by varying the metal film thickness in this range (40-70 nm). As the metal thickness is increased from 40 to 70 nm, the following changes in the SPR characteristics are evident: 1) the reflectance suffers dramatic loss at resonance, 2) the surface plasmon resonance angle (θ_{SPR}) shifts to a lower angle, 3) resonance curves become sharper, the FWHM narrows, and 4) the magnitude of the loss in reflectivity decreases. The most striking difference between the SPR curves of the two metals films of the same thickness is that the linewidth of the plasmon resonance curve for silver film is much sharper than that of the Au film based sensor. Stated differently and as it is well known that: (1) a silver film sensor displays narrower SPR curve offering higher signal-to-noise ratio, but suffers from chemical instability, and (2) a gold film sensor displays larger shift in θ_{SPR} due to changes in the refractive index of analytes and is chemically stable.

Figure 3.5 summarizes differences between the SPR curves of silver and gold films. The percentage loss in reflectivity due to plasmon excitation is the highest (100% loss) for 47 nm thick gold and 50 nm thick silver, respectively. The FWHM of the SPR curves are inversely related to the thicknesses of the metal film. The FWHM of the SPR curve for the Ag thin film sensor is 5 to 7 times narrower than that of the Au thin film sensor for metal

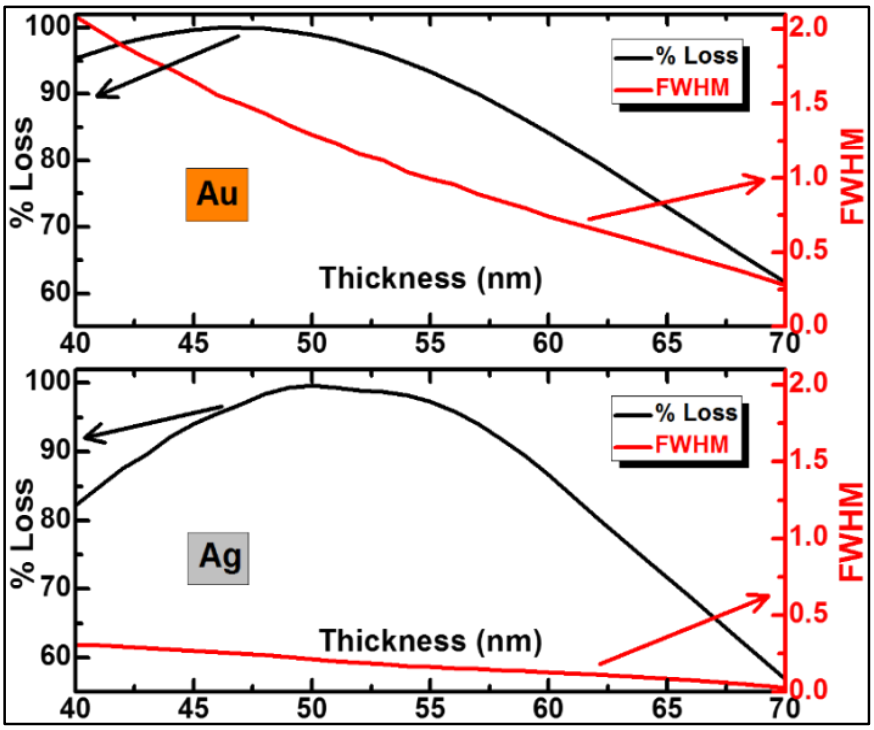

Figure 3.5 Loss in reflectance and FWHM of the resonance curves as functions of film thickness.

film thickness ranging from 40 to 70 nm. The correct thickness and type of metal film (Ag or Au) required for an SPR sensor of a specific application can be easily determined from these results. As we present here a systematic comparison between different sensor structures, the optimum film thickness of a single metal based SPR sensor has to be such that the resonance curve produced by a sensor structure under consideration not only shows the maximum possible loss in reflectivity but also produces the narrowest possible FWHM of the reflectivity curve. Guided by these considerations, the optimum thickness range for a Au film based SPR sensor would be 42-52 nm, and the thickness range for a Ag film based sensor would be 45-55 nm.

3.2.2 Simulation results for bimetallic (Ag/Au) sensor

In order to enhance the sensitivity of SPR sensors using angular interrogation method (prism coupling), it is desirable to narrow down the line-width (FWHM) of the reflectivity curve so that extremely small shifts in θ_{SPR} could be easily discerned. For the most efficient/tight coupling of SP modes with the incident photon component along the metal film interface, it is essential that the total thickness of the metallic film be confined within the window of 30 nm to 70 nm. Also, the effect of Ag to Au ratio is found to be incomparably superior in terms of evanescent field enhancements, than that observed for a simple Au/Ag approach [36, 37].

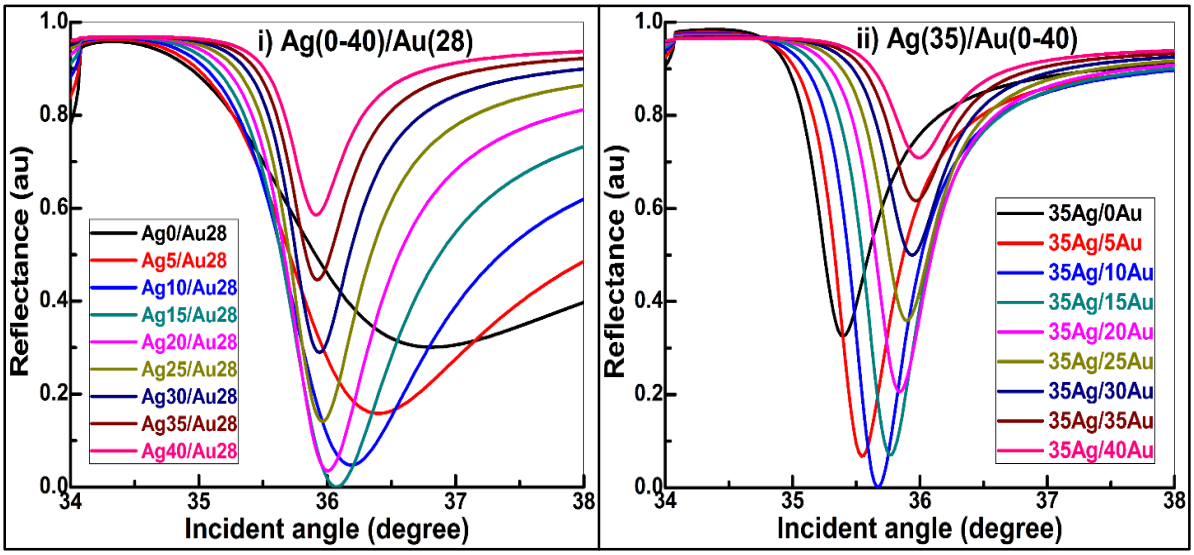

Figure 3.6. Reflectance vs incident angle curves for bimetallic (Ag/Au) film SPR sensors with different thickness ratios; i) Fixed Au film and variable Ag film thicknesses, ii) Fixed Ag film and variable Au film thicknesses.

Figure 3.6 shows computed SPR curves for bimetallic Ag/Au based SPR sensors having different thickness ratios of silver to gold. Figure 3.6(i) exhibits SPR curves for

bimetallic sensors having gold film thickness fixed to 28 nm whereas the silver film thickness varying in the range of 0 to 40 nm. On the contrary, figure 3.6(ii) shows SPR curves for bimetallic sensors having a silver film thickness fixed to 35 nm whereas the gold film thickness varies from 0 to 40 nm.

Since the change in SPR angle (θ_{SPR}) in figure 3.6 with respect to the film thickness is very small in comparison to much larger changes in reflectivity, as well as in FWHM, we again simplify the comparison between the two sets of data by plotting them in a manner already used for single metallic films in figure 3.5. These results are shown in figure 3.7. As observed in the case of single metallic film based sensors, a bimetallic sensor having a greater ratio of silver to gold produces sharper resonance curves. Such bimetallic structures

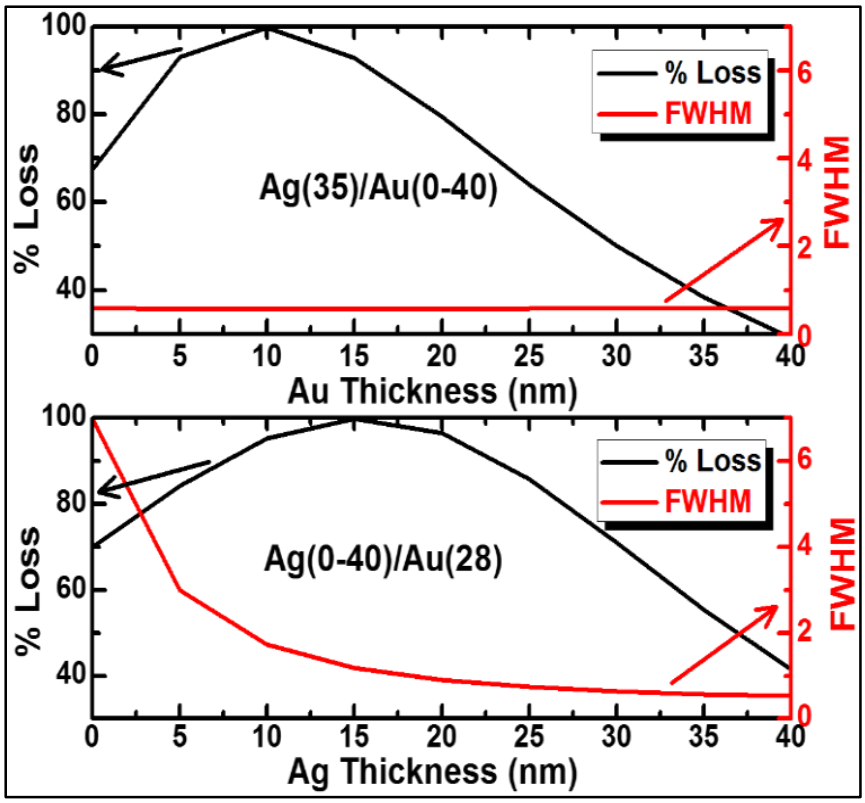

Figure 3.7. Loss in reflectance and FWHM as functions of metallic film thickness for bimetallic SPR sensors.

benefit from combined advantages of both silver and gold layers. Even-though the SPR characteristics of these bimetallic structures are convincing enough for their candidacy for sensing applications, their usage is limited due to the broad resonance curve produced by the structure and overall instability of the response caused by the reactions at the bimetallic interface. Optical properties (e. g., refractive index) of the interface in such structures are known to undergo significant aging, which could adversely affect sensor performance. We have monitored the SPR characteristics of such bimetallic sensors over extended periods of weeks to months in order to investigate possible aging effects on SPR curves. For the aging measurements, we fabricated a Quartz/35 nm Ag/28 nm Au structure and carried out optical measurements of the SPR curves over extended periods. Our preliminary results show that both the resonance angle (θ_{SPR}) and FWHM of the SPR curves increase with time; over a period of nine months, the resonance angle shifts to higher angle values and the curves become broader. The sensor seems to degrade due to aging effects. Upon completion of the analyses of these data, the results will be presented elsewhere. In the meantime, our assertion is supported by Chen et. al., who have experimentally shown that the growth of the silver oxide layer at the gold/silver interface is responsible for aging effect on the performance degradation of such bimetallic structures [38].

3.2.3 Simulation results for a waveguide-coupled $Ag/Si_3N_4/Au$ structure

The present work is motivated by widespread interest in improving the sensitivity and resolution of SPR sensors and in particular by a desire to explore multilayer structure parameters through which the evanescent field penetration depth can be increased [2, 5].

The usefulness of a dielectric between metal coatings was recognized almost twenty five years ago. Following proposals, by Sarid [39] and later by Kou and Tamir [40], Matsubara et. al. [41] studied the use of a dielectric inserted in between metal coatings over high-index prism. The main finding of this work was that the use of an intermediate dielectric in the sensor architecture improves sensor resolution. In spite of significant activity, the quest continues to further improve SPR sensors for various applications. It is towards this end that we have undertaken computational and experimental investigations of multilayer waveguide-coupled sensors.

The instability of a bimetallic sensor structure due to aging effects at the interface of the two metals, can be easily overcome by inclusion of a slab of dielectric material in between the two metals. We've chosen silicon nitride thin film for this purpose since it offers several exceptional properties; i. e., optical transparency from ultraviolet to infrared (250-900 nm), relatively large refractive index n = 1.91 @ λ = 632.8 nm, thermal stability, hardness, chemical inertness and good insulating properties. Widespread use of the Si_3N_4 dielectric in very large scale integration (VLSI) electronic fabrication and processing industry further justifies its use.

The transfer matrix method was again employed to simulate the reflectance as a function of incident angle for the Ag/Si_3N_4/Au multilayered structure. The thickness ratio of silver to gold was fixed at 35/28 nm, as optimized from the case of bimetallic sensor structure, whereas the dielectric slab Si_3N_4 thickness was varied from 0 to 200 nm in steps of 10 nm. Here the dielectric slab not only prevents the interaction of silver with gold but also acts as a waveguide media supporting the propagation of waveguide modes within,

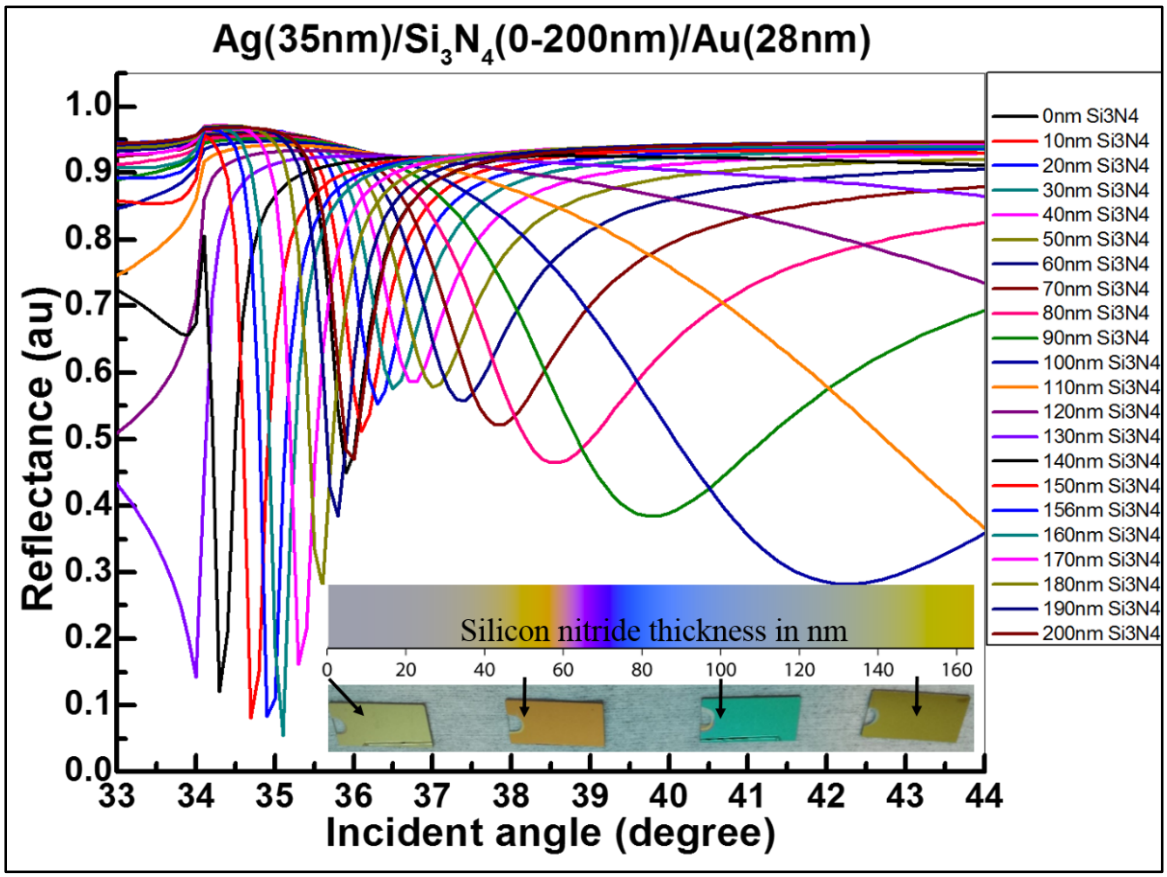

Figure 3.8. Reflectance vs incident angle for multilayered Ag/Si_3N_4/Au structures simulated by using MATLAB.

which shall be discussed later on. As sown in figure 3.8, the SPR curve shows dramatic changes as the Si_3N_4 waveguide thickness varies from 0 to 200 nm (only selective data have been shown here for visual convenience). The inset within figure 3.8 shows optical micrographs of four of our samples, which were used for optical measurements. For these samples, the waveguide thicknesses varies from 0 to 150 nm in steps of 50 nm. The graded color index reflects the influence of the silicon nitride film thickness on overall reflectance from the sample. Unlike the case of a single metal and bimetallic sensor structures, SPR angle (θ_{SPR}) changes drastically from $\theta_{SPR} \approx 34^o$ to 42^o at the prism base, with the change

in waveguide thickness. Therefore we consider both, a shift in SPR angle and loss in reflectivity to be important indicators of the quality of the sensor.

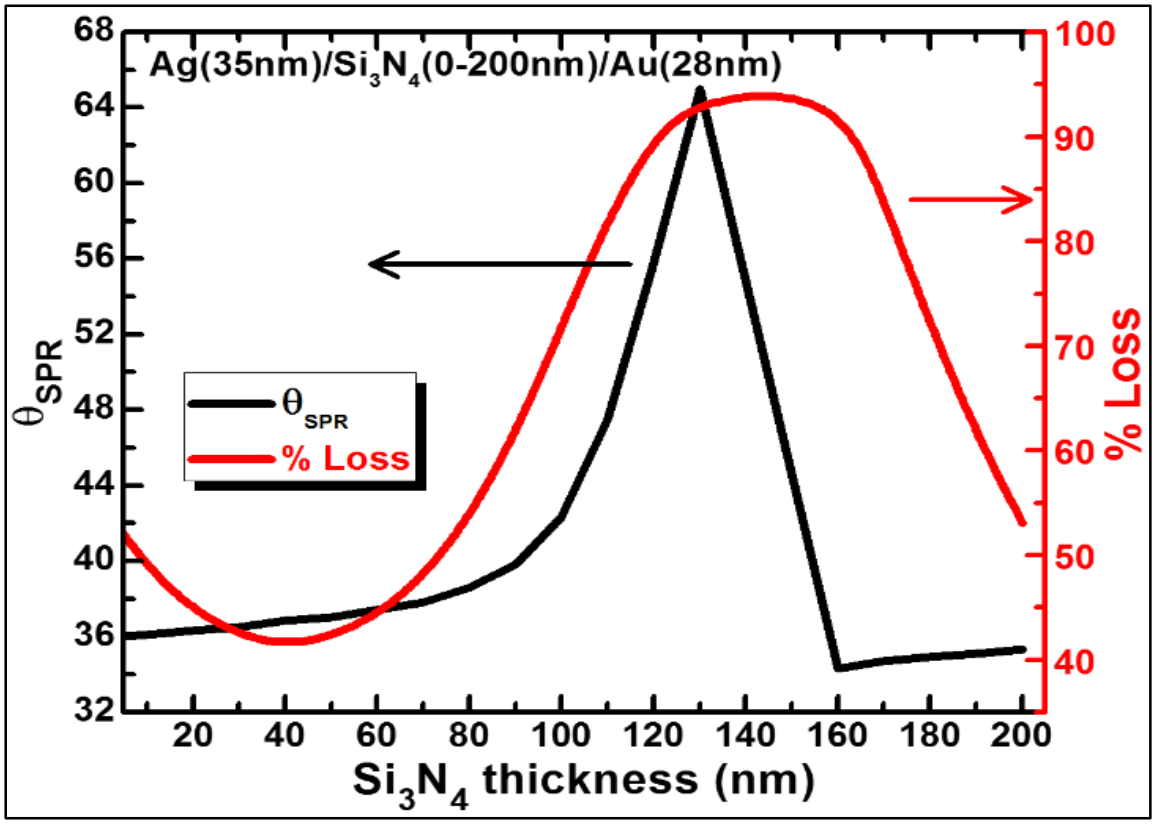

Figure 3.9. Resonance angle and loss in reflectance as a function of waveguide thickness for multilayered structure.

The overall dependence of the sensor performance on dielectric thickness is summarized in figure 3.9; the SPR angle (θ_{SPR}) increases gradually with increase in the waveguide thickness up till 130 nm, thereafter it sharply falls to the lowest possible angle and then staying almost constant. Whereas, the loss in reflectivity very much observes the same nature as θ_{SPR} but stays almost constant within the range of 115-160 nm of waveguide thickness, for which the loss in reflectivity is maximum (~90-95%). For a high performance sensor, it is not only important to demonstrate maximum losses in reflection corresponding to excitation of plasmons, but also to show that the loss in reflection occurs at the smallest

possible incident angle so that a relatively wider range of angles will be available for SPR measurements. Taking this into account, it is evitable from figure 3.9 that multilayered structures having a fixed ratio of Ag to Au (35/28 nm) but Si_3N_4 waveguide thickness in a range of 140 to 170 nm will make a far better SPR sensor compared to that relying upon a single metal or a bimetallic structure.

Figure 3.10 shows the graph for sensor characteristics of multilayered waveguide coupled sensors, having a fixed thickness ratio of silver to gold (i.e. Ag/Au) but varying thicknesses of waveguide media from 0 to 1000 nm. It is pretty evident from the overall

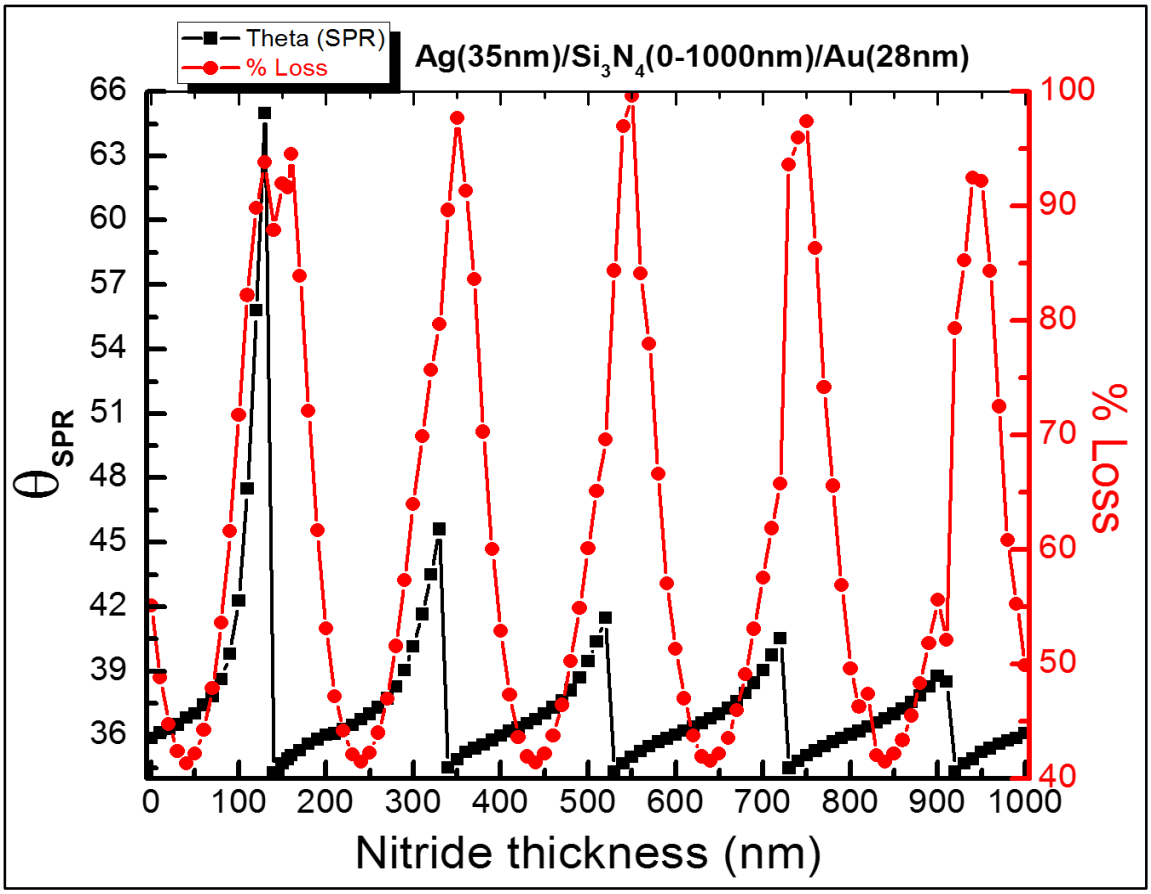

Figure 3.10. Resonance angle and loss in reflectance as a function of waveguide thickness for multilayered structure having a fixed ratio of Ag/Au and Si_3N_4 thickness varying from 0 to 1000nm.

nature of the graph that there could be many other combination of optimized thicknesses of waveguide media sandwiched between a fixed thickness ratio of silver to gold film, in order to achieve a desired surface plasmon resonance characteristics. The nature of the electric fields on the sensor surface and their penetration into the surrounding media cannot be estimated using this chart. The waveguide coupled bimetallic sensor fabricated using this chart, needs to be evaluated for the electric field penetration depths, in order for them to exhibit an overall strong SPR characteristics, as discussed in the next section (3.3).

3.3 Electric field simulations

The sensing ability of an SPR sensor is based on the perturbation of the evanescent fields arising from the sensor surface and propagating into the surrounding medium. Apart from the resonance curve characteristics, loss in reflectivity at resonance angle, FWHM, θ_{SPR} and stability, the other prominent feature of the sensor is the magnitude of the evanescent fields at surface and its penetration depth into a medium under investigation. It should be noticed that the values of the electric fields at the sensor surface have been normalized to unity.

3.3.1 Evanescent fields for single-metal sensors

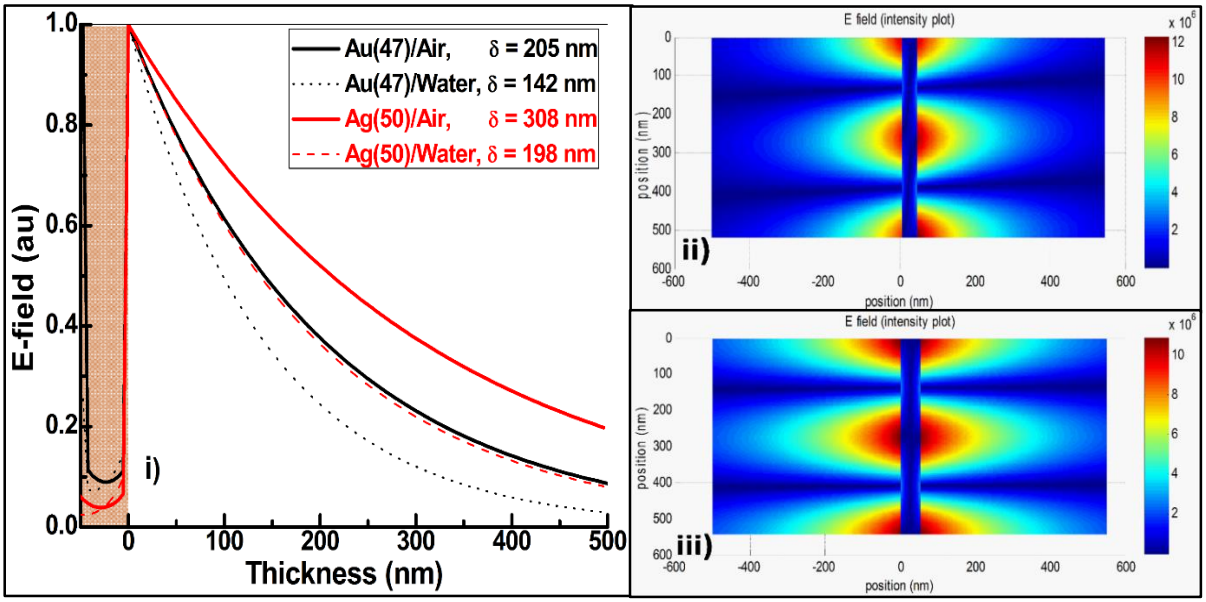

Figure 3.11. i) Electric field penetration curves for gold (47 nm) and silver (50 nm) film sensors, simulated for air and water as analytes. The color contour map of electric field distributions, as it propagates away from the metal film surface into air, are shown in figure ii) and iii) respectively.

Figure 3.11 (i) shows simulations for the electric fields excited at the surface of a gold and a silver thin film SPR sensor. The solid (peach colored) layer drawn for thickness

≤ 0 nm represents metal thin film. The metal (Ag = 50 nm or Au = 47 nm) is identified in the figure inset. These simulated results show how the electric field excited at the surface of single metal based SPR sensor propagates into two different media (air or water) in contact with the sensor surface. As is well known, the evanescent fields decay exponentially into the medium. The skin or penetration depth of the fields is defined as the depth at which the intensity of the electric field falls to $(1/e)^{th}$ of its original value at the surface. As seen in the figure 3.10, the penetration depths in air and water for Au sensor are 205 nm and 142 nm, respectively. In the case of the Ag sensor, the penetration depths are 308 nm for air and 198 nm for water. Figure 3.11(ii) and 3.11(iii) show a colored contour map of the electric field distributions on the surface of Au and Ag sensors. The color bar represents the field strength which is the highest at the metal surface and decays exponentially as the fields propagate away from the metal surface.

3.3.2 Simulations of fields for bimetallic sensor

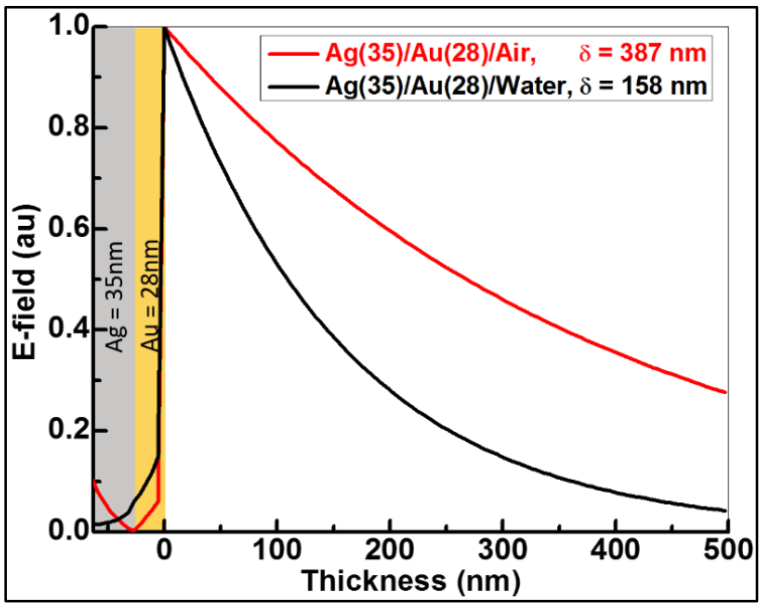

Figure 3.11. Electric field penetration into air and water.

In the case of a bimetallic (Ag/Au) sensor, simulated fields are shown in figure 3.11. Here the penetration depth of the electric field is longer than penetration depth for the single metal Ag or Au based sensor. But as discussed earlier, the bimetal sensor suffers significant aging effects at the interface of the two metallic films leading to a highly unstable sensor; we have observed significant degradation in sensor performance over periods, from days to nine months and it limits the usefulness of this sensor. For example, over a period of a month, the FWHM of the SPR curve of the bimetallic sensor increases from 0.59^0 to 0.65^0 and the loss in reflectivity decreases from about 56% to 53%. The FWHM and loss in reflectivity of the same sensor, when measured nine months later, were found to be 0.86^0 and 50%, thus confirming significant degradation in its performance characteristics.

3.3.3 Simulations of evanescent fields for waveguide coupled sensor

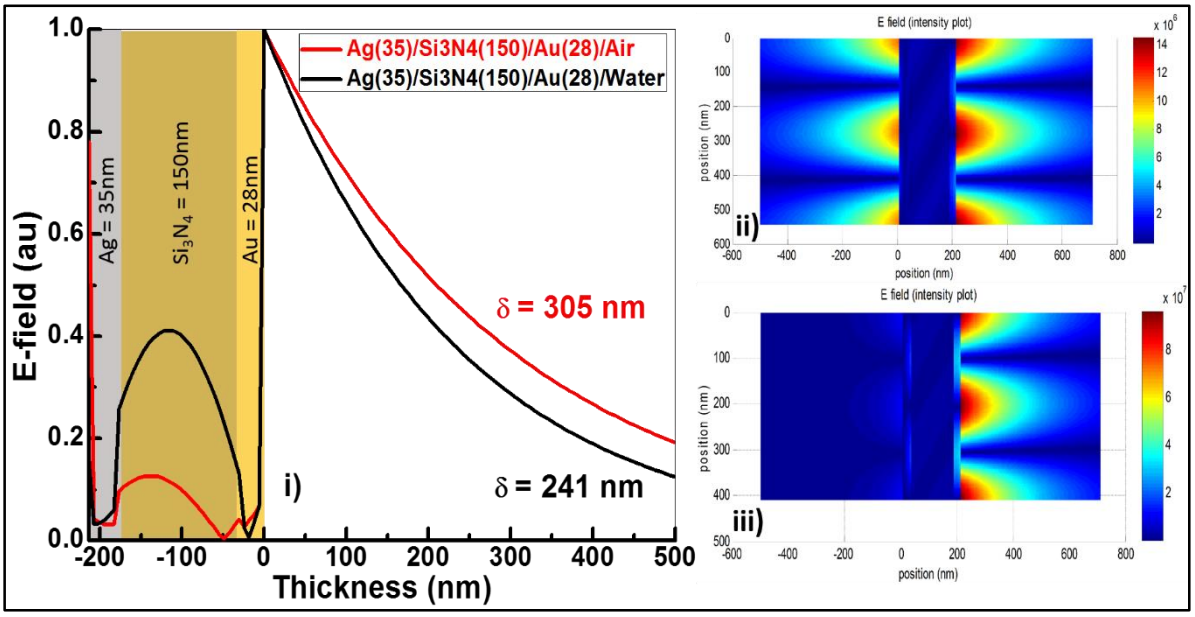

Figure 3.12. Electric field penetration into air and water from the bimetallic waveguide coupled ($Ag/Si_3N_4/Au$) SPR sensor.

Figure 3.12 shows simulations of the evanescent electric fields for a waveguide-coupled Ag/Si_3N_4/Au sensor having air or water in contact with the sensor surface. It is remarkable that the evanescent field extend for approximately 305 nm in air and 241 nm in water in contact with the sensor surface. Given such long penetration depths, it becomes possible to design experiments to study the influence of evanescent fields on materials' properties in the immediate vicinity of the surface and at depths within which the evanescent fields are strong enough to significantly modify the material. An example of such experiments will be the one in which the evanescent fields can be used to modify the surface anchoring of liquid crystalline materials and study their orientational order. The colored contour map in figure 3.12(ii) and (iii) shows the nature of the electric fields for the same waveguide coupled structure as these fields propagate into air or water. Thus the structure with 150-nm thick Si_3N_4 waveguide dielectric exhibits the best sensor characteristics; narrowest resonance curve (highest resolution) and extended range of evanescent fields into the material at the interface, ranging from about 241 nm for water to about 305 nm for air.

3.3.4 Relative strength and penetration depth of evanescent electric fields

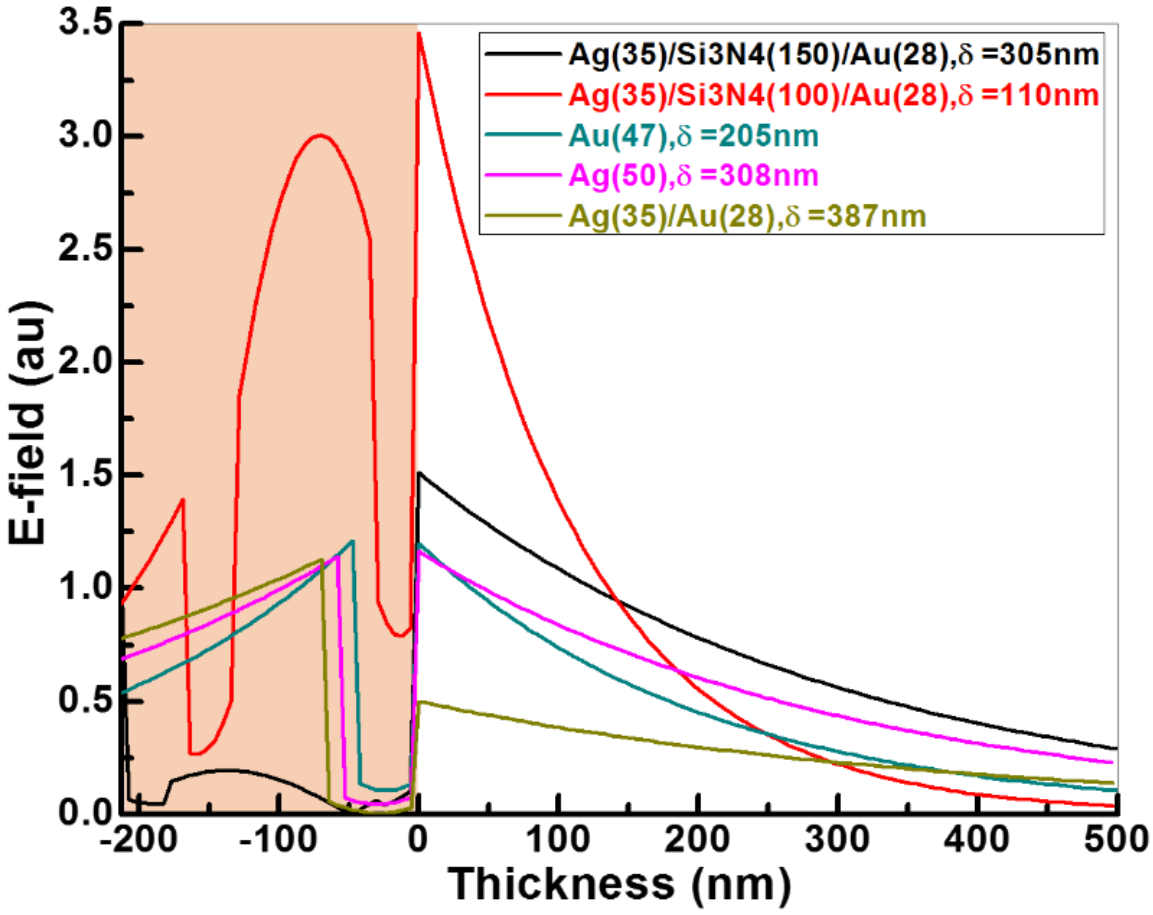

Figure 3.13. Schematic of electric fields from different sensor structures propagating into vacuum/air.

Figure 3.13 compares simulated electric field strengths and field penetration depths into air/vacuum for simple metal, bimetallic and waveguide coupled sensors. In the case of a single metal Au or Ag sensor, the field strengths at the surface of the sensor are almost the same in magnitude but they decay differently into the medium. The penetration depth in air for the Au sensor is 205 nm and for the Ag sensor it is 308 nm. In the case of a bimetallic sensor having metal film thicknesses of 35 nm Ag and 28 nm Au, the field at the surface

of the sensor is weaker (half the magnitude) compared to the field at the surface of the single metal sensor, but with longer penetration depth, δ_{SP} = 387 nm. For a 100 nm thick Si_3N_4, the field at the surface of the sensor is three times larger in magnitude than the field at the surface of the Ag sensor, but the field penetration depth is shorter. The electric field for the 150 nm thick Si_3N_4 sensor decays into the medium in a manner that is almost the same as that with the 50 nm thick Ag sensor. As evidenced by this comparison, in the case of the waveguide-coupled sensor, there is a trade-off between the surface field strength and penetration depth into the sensing medium. It is interesting that a desired combination of surface field strength and penetration depth can be obtained by adjusting the dielectric thickness. As seen in the solid (peach colored) slab for the region below 0 nm thickness in figure 3.13, an optimum thickness of Si_3N_4 waveguide layer supports excitation of strong waveguide modes, whereas the surface plasmon modes are excited at the outermost layer of the sensor surface (after 0 nm). The stronger waveguide modes are responsible for the surface field enhancement and sensitivity, but the strong plasmon modes are responsible for increased penetration depth into analytes. Different thickness of waveguide layer can be optimized per requirement of sensor applications i.e., higher surface sensitivity or greater penetration depth. For example, the liquid crystal assisted tunable plasmonic device reported by our group in a recent publication could sense electric field induced changes in liquid-crystal dielectrics placed at sensor surface with almost 28 times higher sensitivity than the sensitivity of previously reported similar sensors [5]. The shift in the SPR angle ($\Delta\theta_{SPR} = 1.4^o$) was limited due to a strong surface anchoring forces of the liquid crystal molecules on the sensor (gold) surface. With a 150 nm-Si_3N_4 waveguide coupled bimetallic

sensor employed for similar measurements, the deeper penetration of the electric fields (δ_{SP} = 305 nm) into the bulk of the liquid crystal cell could sense stronger electric field mediated changes in the LC dielectric resulting into a greater shift in the SPR angle (θ_{SPR}).

3.3.5 Table of summary for sensor simulations

Table 3.1 shows a detailed comparison between a single metal sensor using gold (Au) or silver (Ag) thin film, silver/gold (Ag/Au) based bimetallic sensor, and bimetallic-waveguide coupled (Ag/ Si_3N_4/Au) sensors, for their significant SPR characteristics. The sensor characteristics established over here for an optimized sensor architecture are useful for designing and fabrication of SPR sensors of high sensitivity, resolution, stability, and long decay length of plasmon related electric fields. Only those sensor structures that were fabricated for experimental measurements have been listed for comparison over here.

Table 3.1 Comparison of single metal, bimetal and waveguide coupled bimetallic sensor, for their SPR characteristics [6]

Sensor structure (thicknesses in nm)	**Sensor type**	**Angle at which SPR occurs θ_{SPR} (degree)**	**% Loss in reflectivity due to SPR**	**FWHM of the SPR curve (degree)**	**Penetration depth into air (nm)**	**Electric field strength at sensor surface (au)**
Au (47)	Single metal	36.2°	100%	1.5°	205	1.2
Ag (50)	Single metal	35.28°	100%	0.22°	308	1.16
Ag (35)/ Au (10)	Bimetallic	35.67°	100%	0.56	446	0.87
Ag (35)/ Au (28)	Bimetallic	35.6°	56%	0.59°	387	0.53
Ag (35)/ Si_3N_4 (150)/ Au (28)	Bimetallic waveguide-coupled	34.7°	93%	0.28°	305	1.52
Ag (35)/ Si_3N_4 (100)/ Au (28)	Bimetallic waveguide-coupled	42.23°	72%	10.45°	110	3.48

Chapter 4

EXPERIMENTS

4.1 Experimental setup for surface plasmon resonance (SPR) measurements

4.1.1 Rotating detector Kretschman configuration optical system for SPR measurements

The schematic of our Kretschmann configuration optical system, which was used for some of the surface plasmon resonance measurements employing various sensor structures under investigation in this work is shown in figure 4.1 As discussed in our earlier publications [2, 5], it uses a high-index prism (Edmund Optics, N-SF11, refractive index = 1.7847 @ 632 nm), *s*- or *p*-polarized 632 nm He-Ne laser beam, three silicon photo-detectors and JY Horiba Triax-550 spectrometer. We present a brief description of our (θ, 2θ) goniometer based Kretschmann configuration system over here. The circularly polarized laser is first passed through an optical density filter to reduce the intensity and then through a polarizer to obtain an *s*- or *p*- polarized incident beam. As it is customary, (a) the electric field of the s-polarized incident laser points perpendicular to the plane of incidence, whereas (b) the electric field of the p-polarized incident laser points parallel to the plane of the incidence. Once the beam is polarized, it passes through a beam splitter, one of which is used as a reference beam and its intensity is monitored by the silicon detector-1. The second beam from the beam-splitter is used for carrying out ATR measurements. One of the faces of the prism, which forms the base for the total internal reflection of the incident polarized laser beam, is sputtered coated with a known thickness ($\leq$ 50 nm) of noble metallic thin film, which can carry surface plasmon excitations at its

surface. The prism and the silicon detectors are mounted on the (θ, 2θ) goniometer, which facilitates measurements of the relative intensity of the reflected beam as a function of the incident angle at the base of the prism. At incident angles $\leq \theta_c$, the incident laser is transmitted through the back of the prism and is detected by silicon detector-3. For $\theta \geq \theta_c$, the incident beam undergoes total internal reflection and its intensity is then measured by detector-2. The output from each silicon detector is connected to an amplifier. The amplified signals are routed to a data acquisition and analysis Labview software. The reflected beam is also routed to JY-Horiba Triax-550 spectrometer for spectral analysis. Following total internal reflection, the surface plasmon polaritons (SPPs) are detected through the observation of an almost 100% loss in the reflected intensity at some angle $\theta_{SPR} > \theta_c$, where θ_c is the critical angle for which the angle of refraction is 90^o. The fraction of the incident light missing from the totally reflected beam is viewed as converted into surface plasmon excitations propagating along the interface. By varying the angle of incidence of totally reflected light inside and at the base of the prism, the resonance condition for exciting SPPs can be satisfied. The measured resonance data are analyzed by using Fresnel's equations and they provide quantitative results for the optical properties of the materials at the interface.

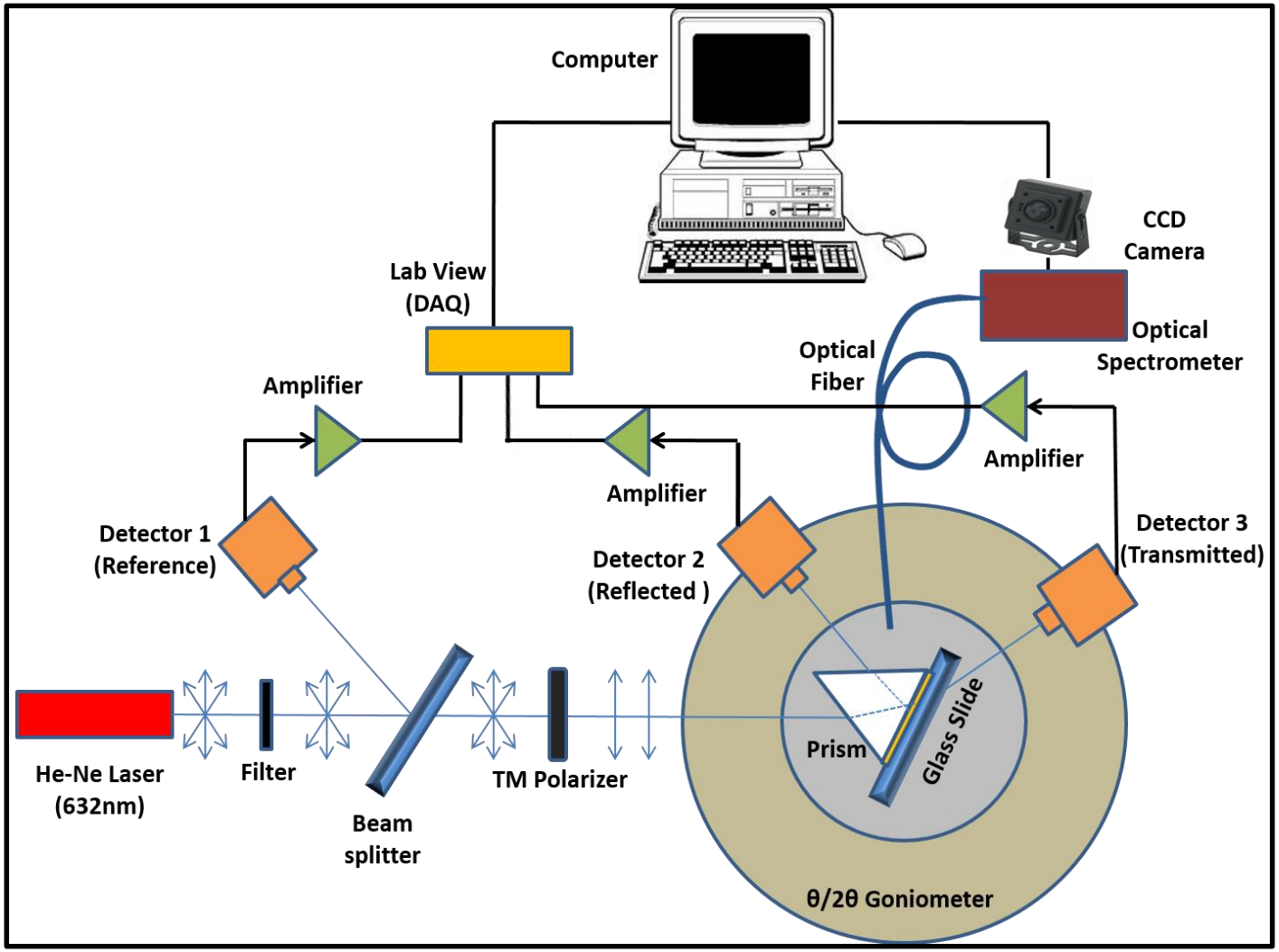

Figure 4.1 Experimental setup using hybrid Kretschmann/Otto configuration optical system and a spectrometer for SPR measurements [2]

4.1.2 Hybrid Kretschmann-Otto configuration for investigation of SPs in liquid crystal containing gold nanoparticles

It has been shown recently that the incorporation of relatively small concentrations of gold nanoparticles (Au-NPs) in a polymer-dispersed liquid crystal (PDLC) lowers the operating threshold voltage (by almost 50%) [1], increases the optical transmission and improves the frequency response of the device. External perturbations, which affect the alignment of the LC molecules in a PDLC, can significantly change the dielectric properties of the LC, which in turn can influence SPs excited in noble metal NPs embedded in the PDLC. Thus an obvious connection between the noble metal NPs and electro-optical properties of PDLCc is throgh SP-induced electric fields in the material.

In order to investigate how effectively SPs can be excited in a composite of the nematic phase of LC (E44) and dispersions of Au-NPs (10^{-10} mol/liter in water), we have carried out ATR measurements on the same composite. Four different samples were prepared by spin coating on glass slides mixtures of LC and dispersions of Au-NPs; sample-1 contained only the LC, sample-2 contained a mixture of the LC and 35 wt.% dispersions of the Au NPs, sample-3 contained the LC and 50 wt.% dispersion of Au NPs, and sample-4 contained only dispersion of Au NPs. The same rotating detector Kretschmann configuration system described in section 4.1.1 was employed for the surface plasmon resonance measurements in all these samples. The geometrical arrangement in these measurements to couple the incident p-polarized beam to SPs, resembles a hybrid Otto configuration (as discussed earlier in section 2.1.4) consisting of a high-index prism, LC as the dielectric medium, and noble metal NPs, as shown in the figure below.

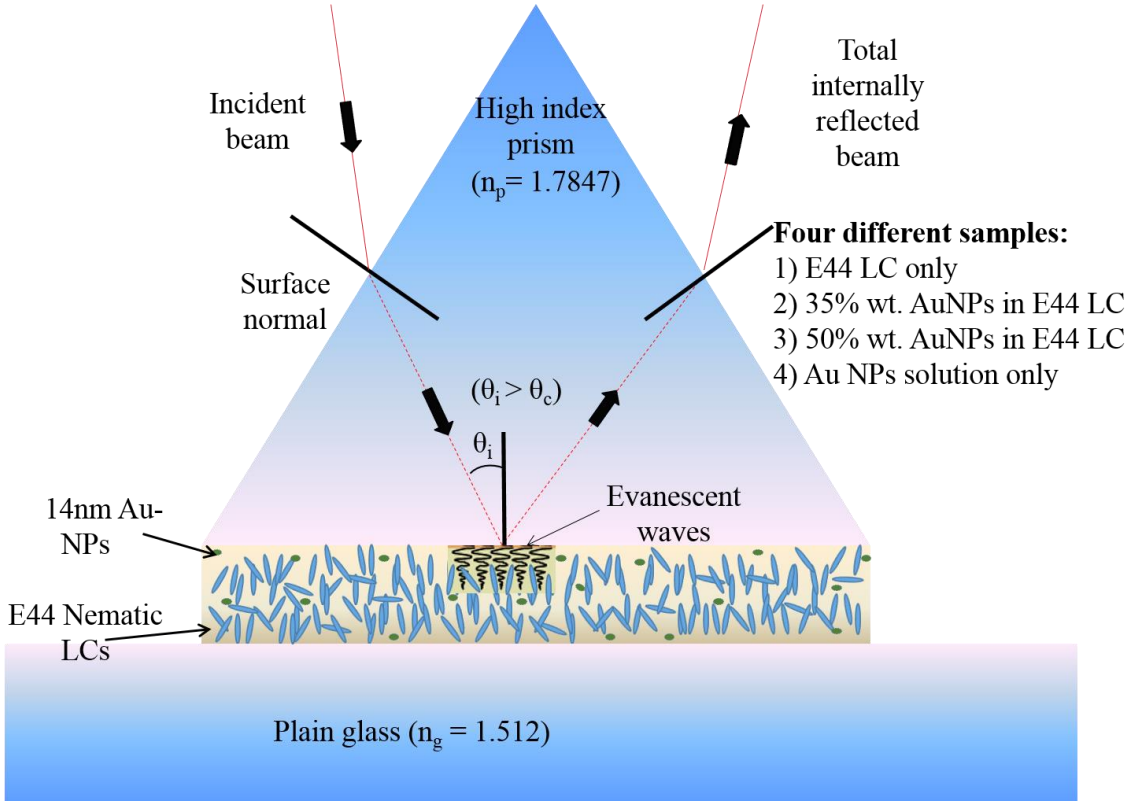

Figure 4.2 Hybrid Kretschmann-Otto configuration for surface plasmon measurements in composite samples of LCs and different concentrations of Au-NP dispersions

Inspite of an apparent immiscibility of the Au NPs dispersion medium and the LC, at least some, if not most of the NPs must come in contact with LC molecules to produce the observed loss in totally-reflected intensity at certain angles. There are sufficient evidence to believe that the resonant coupling conditions are met between the momentum of incident photon along the prism/sample interface and the local plasmons excited around Au-NPs and LC interface, which shall be discussed in detail in the results and discussion.

4.1.3 Arrangement for investigation of electric field induced changes in dielectric environment at metal/nematic liquid crystal interface

As sketched in figure 4.3, a device was fabricated by sandwiching ≈ 40 μm thick film of liquid crystal (E44) between 30 nm thick gold coating over the base of a high-index prism (Edmund Optics, N-SF11, refractive index = 1.7847 @ 632 nm) and an Indium-Tin-Oxide (ITO) coated glass slide. This particular liquid crystal exhibits nematic phase over a wide temperature range, from -10^{o} C to100^{o} C with refractive indices of n_o = 1.52395 for ordinary waves and n_e = 1.77526 for extraordinary waves at a wavelength of λ = 632.8 nm. The gold coating and ITO were insulated from each other by using SiO_2 beads of diameter ≈ 40 μm and they were used as electrodes to apply (1 kHz) electric fields across the device.

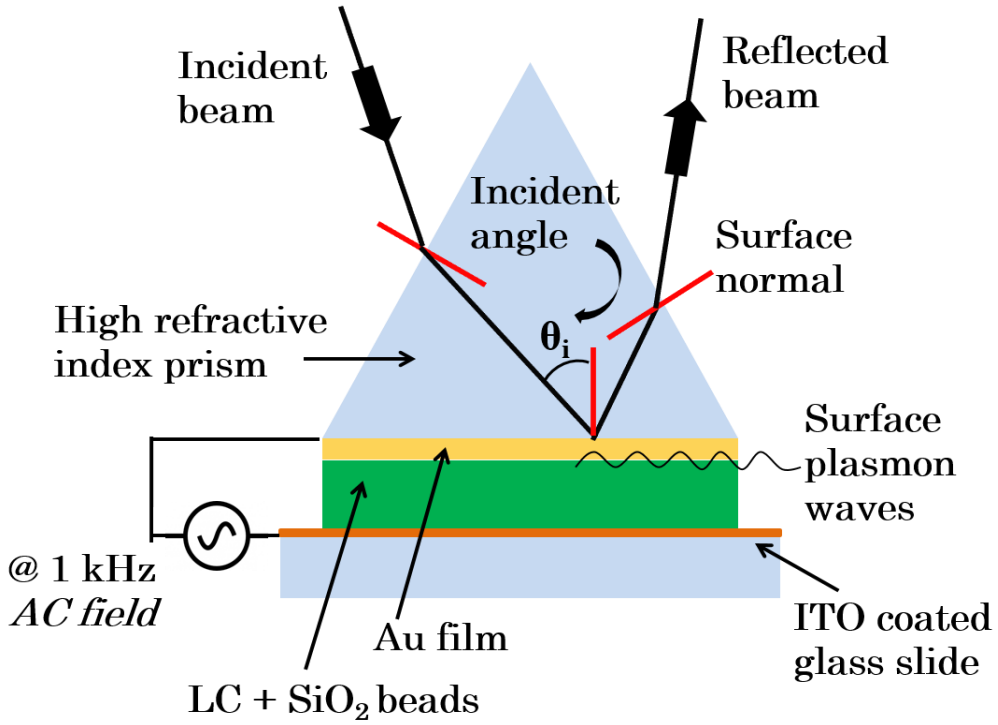

Figure 4.3 Schematic layout of the liquid crystal assisted tunable SPR device, employing a high index prism/Au-film/LC multi-layered structure [5]

This particular frequency is chosen based on our previous results, which have shown the optimum response of E44 to occur near 1 kHz [1]. Since the LC molecule alignment and thereby the electro-optical properties of the sensor are controlled by the nature of the surface (e.g., surface material, smoothness, impurities, and lattice defect), it is important to know the microstructure of the gold film.

The SPR curves were measured as a function of external 1 kHz electric fields, by using the Kretschmann configuration rotating detector system shown in figure 4.1. It is worth pointing out that ATR curves have been measured for one or two values of dc fields and these previous measurements have demonstrated the sensitivity of the technique to dc fields. The present work, however, provides the first set of detailed ATR measurements spanning a much wider range of ac fields that has yielded quantitative information on the sensitivity of the technique to changes in the dielectric environment at interfaces. The surface anchoring forces acting on LC molecules can limit the orientation of LC molecules, particularly adjacent to the electrodes in a device, and thereby influence device performance. The electric field dependencies of resonance angle and reflectivity at resonance are discussed in the results and discussion section.

4.1.4 Multilayer sensor structure/geometry and experimental setup

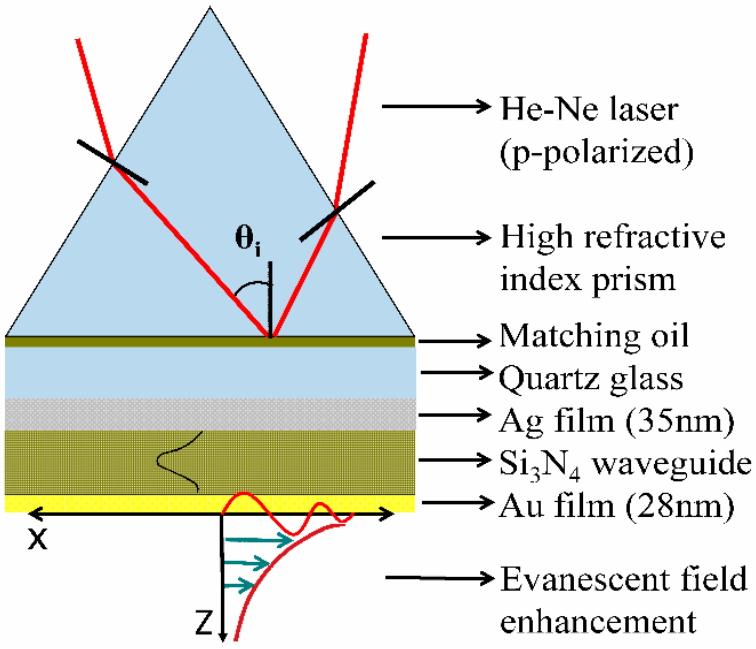

Figure 4.4 Schematic of quartz/Ag/Si_3N_4/Au multilayer structure coupled to high index prism [6]

The schematic of figure 4.4 shows the geometry of the multilayered sensor structure employed for experimental measurements. As mentioned earlier, the Si_3N_4 waveguide-coupled structure was deposited on quartz substrate. A waveguide-coupled SPR sensor is realized by optically coupling this multilayer structure to high-index prism, which is then used to carry out SPR measurements by using Kretschmann geometry discussed elsewhere.[2,5] We have investigated effects of two important parameters of thus fabricated sensors, i.e., materials selection (Ag *vs* Au) and thickness of the Ag, Au, and Si_3N_4 layers. In addition to relevant baseline data on two single metal sensors, we present SPR measurements on four additional samples: i) quartz/35-nm-Ag/28-nm-Au bimetallic structure (identified as sample-3), ii) quartz/35-nm-Ag/50-nm-Si_3N_4/28-nm-Au (sample-

4), iii) quartz/35-nm-Ag/100-nm-Si_3N_4/28-nm-Au (sample-5), and iv) quartz/35-nm-Ag/150-nm-Si_3N_4/28-nm-Au (sample-6).

4.1.5 Fixed detector Kretschmann configuration optical system for pump-probe spectroscopy (SPR and PL measurements)

Figure 4.5 shows a schematic of our fixed detector optical system employing the multilayered SPR structure coupled to a high index prism in a Kretschmann configuration. It is a modified version of the experimental setup reported earlier by our group for similar kind of pump-probe spectroscopy measurements [43]. It uses a 10-mW He-Ne laser (λ=632.8nm) as a pump beam to excite surface plasmons on the multilayered sensor surface, and a 2-W water cooled Spectra Physics Ar-ion laser (λ=514nm) as a probe beam , which can be used for example, to excite fluorescence of particles coated on the sensor surface. The detection system consists of a JY-Horiba's 1250M Spectrometer equipped with a liquid nitrogen cooled CCD camera. The angular interrogation (prism coupling) method of SPEs, which is the most accurate and widely used geometry for conventional sensors, requires the plasmon exciting beam to be scanned over large angles at the prism base coated with metal thin film. This demands for a sensor with a larger surface area, a good surface uniformity throughout the scan region, as well as a large amount of sample to be investigated in contact with the sensor surface. Also, with increasing incident angle, not only the shape/profile of the incident spot changes from a circular to an elliptical, but also it gets difficult to keep the plasmon excitation spot fixed for cases where the same vicinity be assessed for the influence of SPEs.

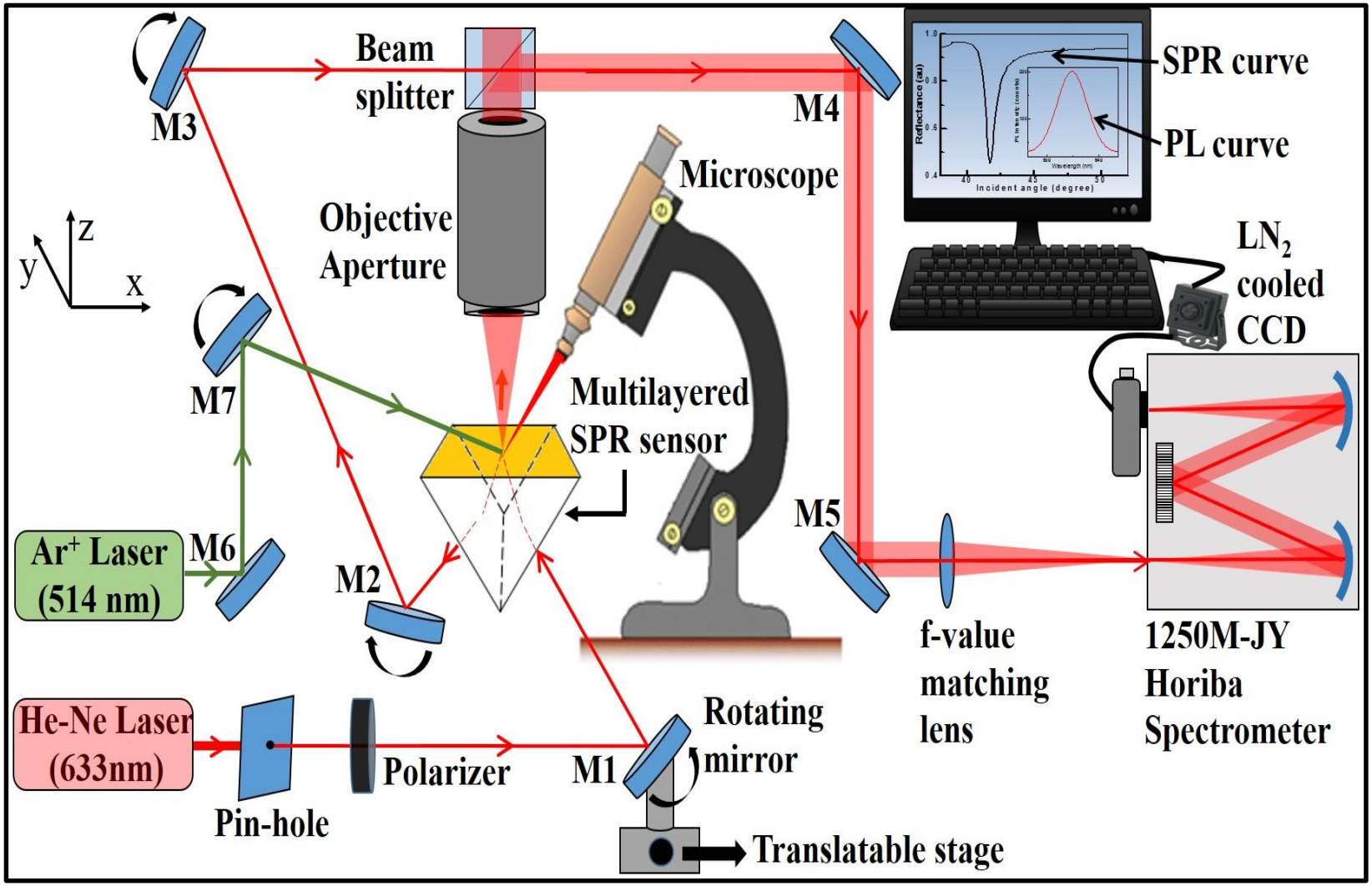

Figure 4.5. Experimental setup for fixed detector Kretschmann configuration optical system, which allows measurement of photoluminescence in presence of surface plasmons

Our fixed detector Kretschmann configuration optical system allows us to eliminate all the difficulties mentioned above. In this system, neither the prism nor the detector is rotated and the incident angles are scanned simply by steering the incident beam using a translatable stage. Only in special cases, when it is desired to examine a surface larger than the beam diameter, the surface can be scanned by prism translation along two orthogonal directions in the x-y plane. Moreover, this also eliminates the inconsistency of the detection efficiency of the detector when measured at different points along the radius of the detector. Thus it allows us to assess the influence of strong surface plasmon related fields excited at the sensor surface on different optical properties of the sample, e.g., photoluminescence, scattering, surface enhanced RAMAN effect, etc.

This optical system can be divided into three sub-systems. The first sub-system consists of a 10-mW He-Ne laser (λ=632.8nm) which generates SPPs and enables ATR measurements in the Kretschmann or Otto geometry without the need for a (θ, 2θ) goniometer. The second sub-system uses a water-cooled Spectra Physics Ar-ion laser with its main emission line occurring at λ = 514 nm. The laser also produces relatively weak lines centered at $\lambda \leq 488$ nm, which were removed by using band pass filter. As shown in the schematic (figure 4.5), the use of λ = 514 nm is not required, but is chosen in order to take advantage of the absorption near 514 nm by CdSe/ZnS quantum dots, which were being investigated during the development of this optical system. And the third sub-system consists of the final detection system which is common for the measurement of both, the pump and the probe signals. The detection system uses JY-Horiba's 1.25 m, f/11

monochromator, 2400-g/mm ion-etched blazed holographic grating, liquid-nitrogen-cooled CCD camera, and a Synergy data collection and analysis software.

The incoming circularly polarized 632 nm He-Ne laser beam propagate horizontally along the x-axis. This beam passes through a 500 μm pin hole, gets collimated and then passes through a polarizer, which ultimately determines the polarization of the final beam, which is incident upon the prism base. A collimated p- or s- polarized beam, after reflection from the mirror M1, is incident upon an inverted high index prism in a geometry shown in the schematic (figure 4.5). After reflection off the base of the prism, the beam impinges upon mirror M2 and is then reflected towards mirror M3. The SPR sensor structure under employment is either coated at the base of the prism or on a high quality quartz slide which can thereafter be coupled to the prism base with the help of a refractive index matching oil. In case of the later, the surface plasmons are excited at the interface of quartz slide and dielectric material under investigation. The prism is mounted such that the base of the prism is parallel to the horizontal x-y plane. The mount for the mirror M1 facilitates two types of motion; its rotation about the y-axis and linear translation along the x-axis. The mirrors M2 and M3 can be rotated about the y-axis. The actual angle of incidence at the base of prism is controlled by the orientation of the mirror M1 and can be calculated by using the geometrical arrangement schematically depicted in figure 4.6 and a calibration procedure discussed later. The spot at which the incident beam strikes the prism base can be centered by translating the mirror M1 along the horizontal x-axis. A Leica-S6 microscope, which has an internally calibrated scale, is used to monitor the incident beam spot. A microscope objective, placed above the base of the prism and

focused at the beam spot, collects all the radiation it receives from the prism base (either PL @ 620nm or scattered beam @ 514 nm) and couples it to the beam splitter above it. From there, a part of the light collected from the topmost face of the beam splitter can be sent into a video camera for imaging the sample placed over the sensor surface, whereas the remaining of it goes into the spectrometer for further analysis, following the optics as shown in the figure. The beam, which comes out of the other face of the prism after reflection, hits the rotating mirror M2. This mirror M2 is rotated until the reflection from its surface again hits the center of mirror M3. Finally, mirror M3 is rotated to send the reflected signal to the beam splitter and ultimately into the spectrometer, after going through the optics which ensures a perfect match between the f-values of the external optics and the spectrometer.

This arrangement allow us to measure the spectral characteristics (relative intensity, wavelengths, etc.) of the reflected & scattered signals, as a function of the angle of incidence at the prism base for *s*- or *p*- polarized beam without making a use of conventional (θ, 2θ) goniometer. The first sub-system (consisting of He-Ne laser) enables the measurements of the surface plasmon related ATR data, whereas the second subsystem consisting of 2-W water cooled Ar-ion laser adds to the versatile nature of our optical system, allowing to carry out simultaneous measurements of the PL and/or scattering of light off the samples mounted on top of the prism base.

4.1.6 Geometrical arrangement for angle calculation at the prism base in fixed detector system

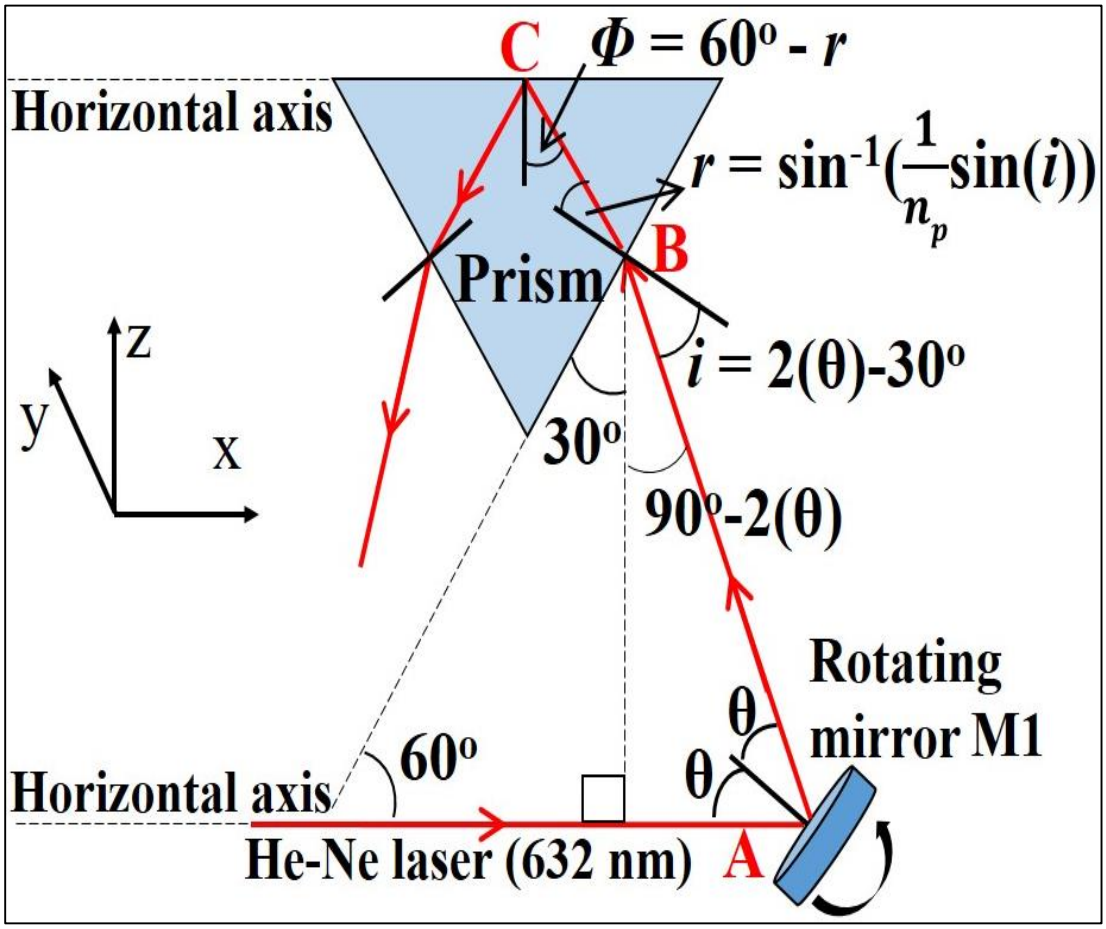

Figure 4.6 Geometrical arrangement for determining the incident angle at the prism base (inspired from [43])

The geometrical arrangement schematically depicted in figure 4.6 simplifies the calculation of angle of incidence at the base of the prism (Φ), which is controlled by the orientation of the rotating mirror M1. Immense care was taken while aligning the laser and the prism, and it was made sure that the laser beam incident at point A of the rotating mirror and the prism base remains parallel to the horizontal x-y plane of the optical setup. The

angle of incidence at the base of prism can be easily determined by using this calibration procedure for the arrangement of rotating mirror & prism in the above shown geometry.

The laser beam incident on M1 at point A, after reflection, enters into the high index prism at point B and hits the base of the prism at point C which is in plane with the horizontal axis. The angle of incidence at the prism base (Φ), measured with respect to the surface normal to the base, is responsible for exciting the surface plasmons at the interface of sensor structure and the analyte media, at angles greater than the total internal reflection. All the angles corresponding to the geometrical arrangement are labelled in the figure 4.6. The refractive index of the high index prism employed in our optical setup is $n_p = 1.7847$. The angle of the laser beam at prism base (Φ) has been determined by applying the Snell's law at the interface of prism and external media (air), and calculations for angles have been listed in table 4.1

Table 4.1 Determination of incident angle (Φ) of laser beam at the base of prism

θ	$r = \sin^{-1}\{\frac{1}{n_p}\sin(i)\}$	**Φ = (60-r) Angle @ prism base**	**θ**	$r = \sin^{-1}\{\frac{1}{n_p}\sin(i)\}$	**Φ = (60-r) Angle @ prism base**
43	27.68346	32.31654	37	22.90843	37.09157
42.5	27.32545	32.67455	36.5	22.46778	37.53222
42	26.95961	33.04039	36	22.02134	37.97866
41.5	26.58611	33.41389	35.5	21.56928	38.43072
41	26.20512	33.79488	35	21.11174	38.88826
40.5	25.81683	34.18317	34.5	20.6489	39.3511
40	25.4214	34.5786	34	20.18091	39.81909
39.5	25.019	34.981	33.5	19.70793	40.29207
39	24.6098	35.3902	33	19.23012	40.76988
38.5	24.19398	35.80602	32.5	18.74763	41.25237
38	23.7717	36.2283	32	18.26061	41.73939
37.5	23.34313	36.65687	31.5	17.76922	42.23078

4.1.7 Experimental setup for measuring electric field dependence of photoluminescence

Our fixed detector Kretschmann configuration optical system enables us to assess the influence of strong surface plasmon related fields (excited from the sensor surface) on the photo-luminescent properties of quantum particles coated on the sensor surface. The electric fields produced by surface plasmons excitations are believed to have an oscillating/alternating nature, as in the case of an externally applied *AC* electric field. Therefore, it is significant to understand how the nature of photoluminescence from these semiconducting core-shell quantum dots gets affected when placed directly under the influence of externally applied *AC* electric fields at a fixed (given) frequency. Figure 4.7 shows the schematic of the experimental arrangement used for carrying out photoluminescence measurements of the CdSe/ZnS quantum dots under the influence of externally applied *AC* electric fields.

The experimental setup makes use of the same 2-W water cooled Spectra Physics Ar-ion laser (λ=514nm) as a probe beam to excite the fluorescence of CdSe/ZnS quantum dot particles particles. The detection system consists of the JY-Horiba's 1250M Spectrometer equipped with a liquid nitrogen cooled CCD camera, the same used in our fixed detector Kretschmann configuration optical system. The quantum dot particles under investigation (i.e., CdSe/ZnS, more details discussed in section 2.3.1.1), are completely soluble in chloroform ($ChCl_3$) solution and for this reason a dispersion of these particles in chloroform can be considered as a uniform media for electric field measurements across them. A thin film of these quantum dot nanoparticles dispersed in chloroform was sandwiched between two ITO (Indium Tin Oxide) coated glass slides. This arrangement is

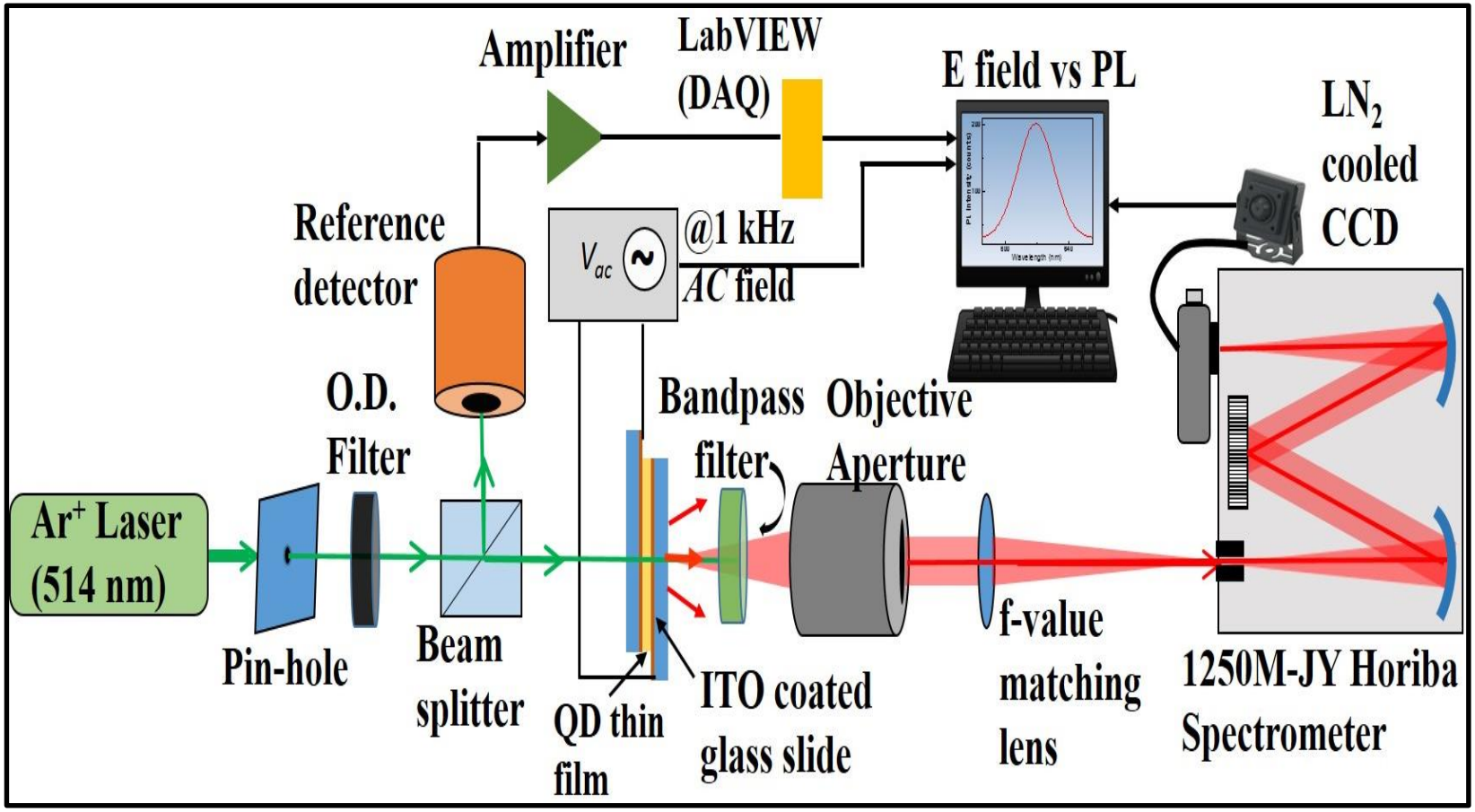

Figure 4.7 Experimental arrangement for measuring the effect of externally applied AC electric field on the photoluminescence from CdSe/ZnS quantum dots

similar to a parallel plate capacitor, wherein the separation between the two electrodes are determined by the spherical silica (SiO_2) beads of known diameter. These beads have been used in our previous measurements as well and are known to have no additional optical effects [5]. The silica beads of known diameter not only helps to keep the two electrodes from shorting, but also helps in determining the thickness of the quantum dot film under investigation. This information is ultimately used towards the determination of magnitude of electric field strength applied across the quantum dot thin film.

The Ar-ion laser is made to pass through a 500 μm pin hole to reduce the incident beam size which is then passed through an optical density filter in order to reduce the laser intensity. The reduced intensity beam propagates further and hits a 50/50 beam splitter which reflects half of the original incident laser into a reference detector, and transmits the original (remaining) half towards the quantum dot thin film sample. The reference detector is used to normalize the photoluminescence intensity data in order to keep an account of fluctuations in the incoming laser beam itself. The original narrow beam that transmits through the beam splitter hits the quantum dot thin film sample producing a large amount of scattering and transmission signal. The quantum dot particles directly irradiated by the incident laser spot absorbs the energy, pertaining to create electronic excitations within their structure (λ_{ab} = 514 nm). The photoluminescence signals thus excited (λ_{em} = 620 nm) are scattered in all the directions including straight-wards, as shown by the red colored arrows. A microscope objective, placed along the path of the incoming Ar ion laser (straight-wards) and focused at the beam spot hitting the thin film sample, collects a considerable amount of scattered radiations (either PL @ 620nm or scattered beam @ 514

nm) and collimates them towards an f-value matching lens, which ensures a perfect match between the f-values of the external optics and the spectrometer. A 514 nm band-pass filter is employed before the microscope objective so that the contributions from the original laser itself can be completely eliminated from the PL signals collected and thereby collimated to send into the spectrometer. The ITO coated glass slides holding the quantum dot thin film sample are connected to an *AC* power supply to measure the effects of varying externally applied electric fields on the photoluminescence emission of quantum dot particles.

4.2 Thin film deposition

The deposition of noble metallic thin films (Ag and Au) and dielectric waveguide layers (Si_3N_4 and HfO_2), employed in various sensor structures presented in this dissertation, were carried out in the *class-100* cleanroom nano-fabrication facility of the Schimadzu Institute Nanotechnology Research Center, UTA. Depending on whether the mode of deposition is physical or chemical, the thin film deposition techniques are mainly classified into the following two categories:

1) Chemical Vapor Deposition (CVD)
2) Physical Vapor Deposition (PVD)

Some other techniques include; Thermal oxidation, Spin coating and Platting, but they are restricted in applications due to the poor control of thickness and non-uniformity of the film deposited.

In case of CVD, a volatile fluid precursor produces a chemical change on the substrate surface leaving a chemically deposited coating. Since the fluid surrounds the solid object, deposition happens on every surface, with little regard to direction; thin films from chemical deposition techniques tend to be conformal, rather than directional. Whereas, PVD refers to a wide range of technologies where the atoms are directly transported from the source to the substrate through gas phase using mechanical, electromechanical or thermodynamic processes. Since particles tend to follow a straight path, films deposited by physical means are commonly directional, rather than conformal. Thin Film Evaporation (PVD) systems can offer the advantages of relatively high deposition rates, real time rate and thickness control, and (with suitable physical configuration) good evaporant stream directional control for processes such as Lift Off to achieve direct patterned coatings. Due to these reasons (and many others discussed later), even we have utilized PVD for the fabrication of single metal, bimetallic & multi-layered SPR sensors presented in this dissertation.

The PVD techniques are again sub-divided into three types depending upon the mechanics of evaporating target atoms, as mentioned below:

- Evaporation- Thermal evaporation, E-beam evaporation
- Sputtering- DC sputtering, DC Magnetron sputtering, and RF sputtering
- Reactive PVD

Out of these, the former two (evaporation & sputtering) are the most commonly used techniques for their high throughput industrial application.

In general, there are three steps in any PVD process: i) creation of an evaporant from the source material, ii) transport of the evaporant from the source to the substrate, and lastly, iii) condensation of the evaporant onto the substrate to form the thin film deposit. The process of evaporation involves significant amount of heat in the deposition chamber, wherein if oxygen were present, any reactive metal would form oxides. Also, collisions with gas molecules (if any) present along the path during the transport of evaporant from source to substrate would reduce the net deposition rate significantly, and would also prevent growth of dense films. For these reasons, the vapor deposition processes are best conducted under high vacuum conditions.

The general characteristics of thin film deposition which helps determining the appropriate technique are; Deposition rate, Film uniformity (across the substrate, and from run-to-run), Materials that can be deposited (metal, dielectric, polymer), Quality of film-Physical and Chemical properties (stress, adhesion, stoichiometry, film density, porosity, grain size and their orientation, breakdown voltage, impurity level), Deposition directionality (directional: good for lift-off, and non-directional: good for step coverage), and the most significant of all, Cost of ownership and operation.

All the sensor structures were fabricated/deposited over the high quality quartz glass substrates purchased from Ted Pella, Inc. Most of the silver and gold thin films used in this work were deposited using the high vacuum thermal evaporation technique, whereas the waveguide layers, silicon nitride and hafnium oxide, were deposited using the ultra-high vacuum assisted RF (radio frequency) sputtering system. The selection criteria of deposition technique used is more or less governed by the above listed characteristics.

Both, the deposition systems and their operating parameters during the sample fabrication are described in the following section.

4.2.1 Deposition of Ag and Au thin film using thermal evaporation system

The deposition of metallic thin films, Ag (silver) and Au (gold), employed as plasmonic elements in the SPR sensors presented in this work, were carried out using the AJA ATC Orion Series Thermal Evaporation system, as shown in figure 4.8. This system is designed to deliver maximum performance and quality for limited budgets. Similar such units are available in both, high vacuum and ultra-high vacuum versions, inheriting many design features and common parts from the highly evolved ATC and ATC ORION sputtering tools. This system can be outfitted with single or multi-pocket, linear and rotary e-beam sources, thermal evaporation sources, ion / plasma sources, Knudsen cells, low temperature evaporation cells for organic materials, Radak Sources, and magnetron sputter sources. In addition to these features, the system is available with load-locks, heated or cooled substrate holders, various pumping packages and automated control.

The deposition system is facilitated by three thermal evaporation sources, as shown in figure 4.9. Three different targets can be held in separate highly resistive molybdenum boats, as seen in the picture with an open lid of the deposition chamber. The deposition of evaporant atoms from the sources kept in each of these boats can be controlled by toggling

Figure 4.8. AJA ATC ORION Series thermal evaporation system facilitated by three separate thermal evaporation sources, at *Schimadzu Institute:* Nanotechnology Research Center (UTA).

the source shutter switches, namely 1 for silver, 2 for gold, and 3 for aluminum. The system also consists of two 900 W power supply with 2-way switchbox, and a quartz crystal thickness monitor for keeping a real time track of the deposited material. The substrate

holder can accommodate wafers/substrates as large as 6 inches in diameter, and observes radiant heating to 850 ^{o}C with a quartz halogen lamp for samples upto 4” and 300 ^{o}C for samples ranging in size from 4” to 6”. The substrate holder is also facilitated by a continuous motorized rotation controller (0-50 RPM) in order to retain the uniform distribution of evaporant atoms by rotating the substrate during the time of deposition.

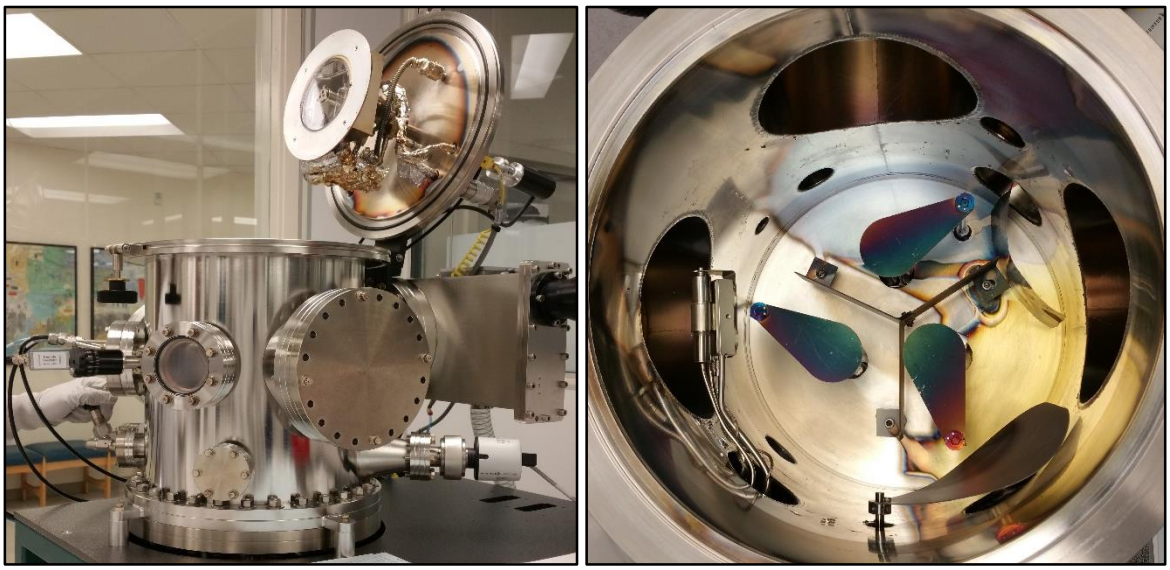

Figure 4.9. The ATC ORION series thermal evaporation system with open lid, showing the three sources facilitated with separate shutters to control the deposition.

We have deposited a series of sensor structures, viz., single metal, bimetallic, and waveguide-coupled bimetallic sensor on high quality quartz substrate. The deposition of silver and gold thin film employed in all of these sensor structures, was conducted using the above shown ATC ORION series thermal evaporation system. The base pressure of the chamber during deposition of silver and gold thin films was set between 4.5 to 5 x 10^{-6} Torr, and the deposition rate was maintained in the range of 0.4 to 0.6 Å/sec. The substrate rotation motor was kept ON and assured of rotating at a speed of 50 RPM during the

process of deposition. The deposition system was calibrated for obtaining correct thickness of films, by depositing several thin films and characterizing them on step IQ profilometer and ellipsometer, prior to the fabrication of actual sensor structures.

4.2.2 Deposition of silicon nitride (Si_3N_4) and hafnia (HfO_2) thin films using RF sputtering system

Unlike thermal evaporation, in which the target material to be deposited is heated to increase its equilibrium vapor pressure, in case of sputter deposition the target material is made to go into the vapor phase by the physical interaction of particles impacting the target. A wide variety of sputtering techniques, as mentioned earlier, are currently used for the purpose of depositing thin films for different applications. The deposition of dielectric thin films, silicon nitride (Si_3N_4) and hafnia (HfO_2), employed as waveguide media in the SPR sensors presented in this work, were carried out using the AJA ATC Orion 5 Series UHV (ultra-high vacuum) sputtering system, as shown in figure 4.10.

The ATC Orion 5 UHV system uses a technique called Magnetron sputtering which deals with two problematic issues simultaneously. Firstly, it overcomes the problem of slow deposition rate and secondly, it prevents the extensive bombardment of the substrate with electrons which creates overheating followed by the structural damage. The system uses magnets behind the cathode which helps trapping the free electrons in the magnetic field directly above the target surface. As a result, these electrons are now not free to bombard the substrate to the same extent as in the case of diode sputtering. At the same time the extensive, circuitous path carved by these same electrons when trapped in the

Figure 4.10. The AJA ATC 5 Orion UHV sputtering system for deposition of dielectric (non-conducting) thin films, at *Schimadzu Institute:* Nanotechnology Research Center (UTA).

magnetic field, enhances their probability of ionizing a neutral gas molecule by several orders of magnitude. This increase in available ions significantly increases the rate at which target material is eroded and subsequently deposited onto the substrate.

This system is capable of confocal sputtering facilitated by five 2" sputter guns. The substrate holder in this system can accommodate substrates upto the size of 4" in

diameter, and coupled to a continuous motorized rotation controller (0-50 RPM). The power supply for this system has a DC as well as an RF generator attached, enabling us to apply an RF bias across the substrate for pre-cleaning and during the deposition to avoid the charge accumulation at the corresponding electrodes. The system has a quartz crystal monitor for thickness monitoring of the deposited material, which helps setting a desired thickness on the monitor, after which the automated source shutter blocks the evaporant from further deposition. During the deposition of silicon nitride (Si_3N_4) thin films, the base pressure of the deposition chamber was set at 5×10^{-8} Torr, and a deposition rate of 0.16 Å/sec was achieved under the precursor Ar/N_2 gas flow at 35/4 SCCM. During the deposition process, the RF power supply of the system and the process pressure were maintained at 150 W and 4 mTorr, respectively.

4.3 Characterization

Characterization refers to the use of various external techniques to probe into the internal structure, morphology, topography and properties of materials. These techniques can help us determine the minutest possible detail of the specimen under investigation like elemental composition, crystal structure, molecular structure, etc,

Characterization of thin films

Since the surface plasmons are highly sensitive to the nature of the metal surface (e.g., surface material, smoothness, impurities, and lattice defects), it is significant to know the microstructures of the thin films involved in the sensor architecture. We have, therefore, examined crystalline structure, surface topography, and impurities in the film by using X-

ray diffraction (XRD), atomic force microscopy (AFM), and X-ray energy dispersive spectroscopy (X-EDS). The correct thickness of all the thin films used in this work were determined by the quartz crystal monitor equipped with each deposition system, which was again cross checked for its accuracy using the step IQ profilometer, in parallel. The refractive index of dielectric thin film (Si_3N_4, HfO_2), used as a waveguide layer, is significantly governed by the growth conditions. In order to confirm the refractive index consistency of the waveguide layers used, they were characterized on the spectroscopic ellipsometer for their refractive index.

4.3.1 X-ray diffraction (XRD) spectroscopy for crystal structure

XRD is the most effective diffraction methods for determining the crystal structure of materials. This technique can identify chemical compounds from their crystalline structure & not from their compositions of chemical elements. Different compounds that have the same composition can be identified using XRD. The XRD spectra as shown in this section were measured using the Bruker diffractometer. The operational parameters for XRD analysis of all the thin films used in this work are as mentioned below:

- X-Ray source, $CuK\alpha_1$ wavelength- $\lambda = 0.15406$ nm
- Scan range- 20-80 degrees (in most cases)
- Operating voltage- 40mV
- Operating current- 40mA
- Increment angle- 0.03
- Scan speed- 1scan/sec

a) XRD spectra of a 40 nm Au film on quartz substrate:

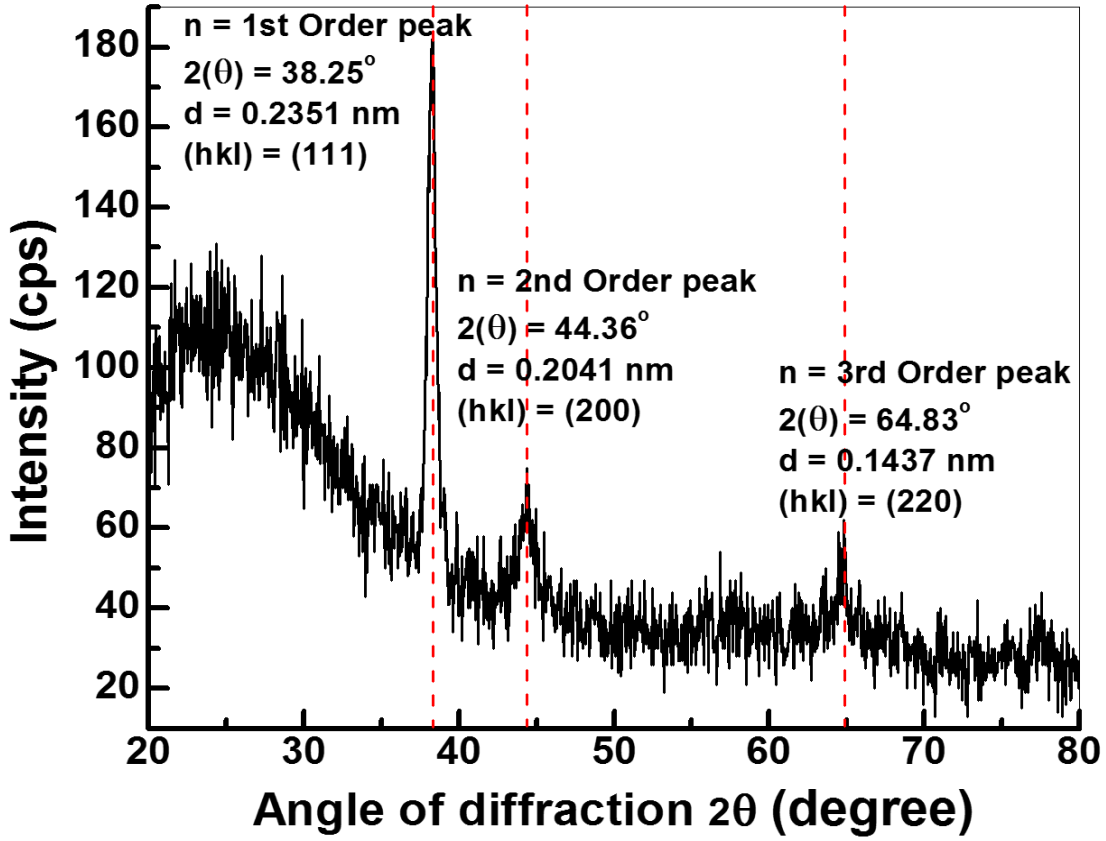

Figure 4.11. XRD spectral analysis of a 40 nm Au film employed for surface plasmon excitations

From Bragg's law, $n\lambda = 2d\sin\theta$ and for a CuKα_1 source, $\lambda = 0.15406$ nm.

Calculations for 1st Order:

Plugging n=1, d = 0.2351 nm & (hkl) = (111) into the equation for lattice constant

$$a = d\,(h^2+k^2+l^2)^{1/2} = 0.2351\,(1+1+1)^{½}$$

$$a = 0.4072 \text{ nm}$$

(Verified with published value for Au, a = 0.4072 nm [86] *)*

Thus, XRD confirms that the crystal structure of gold thin film used is FCC.

b) XRD spectra of a 35 nm Ag film on quartz substrate:

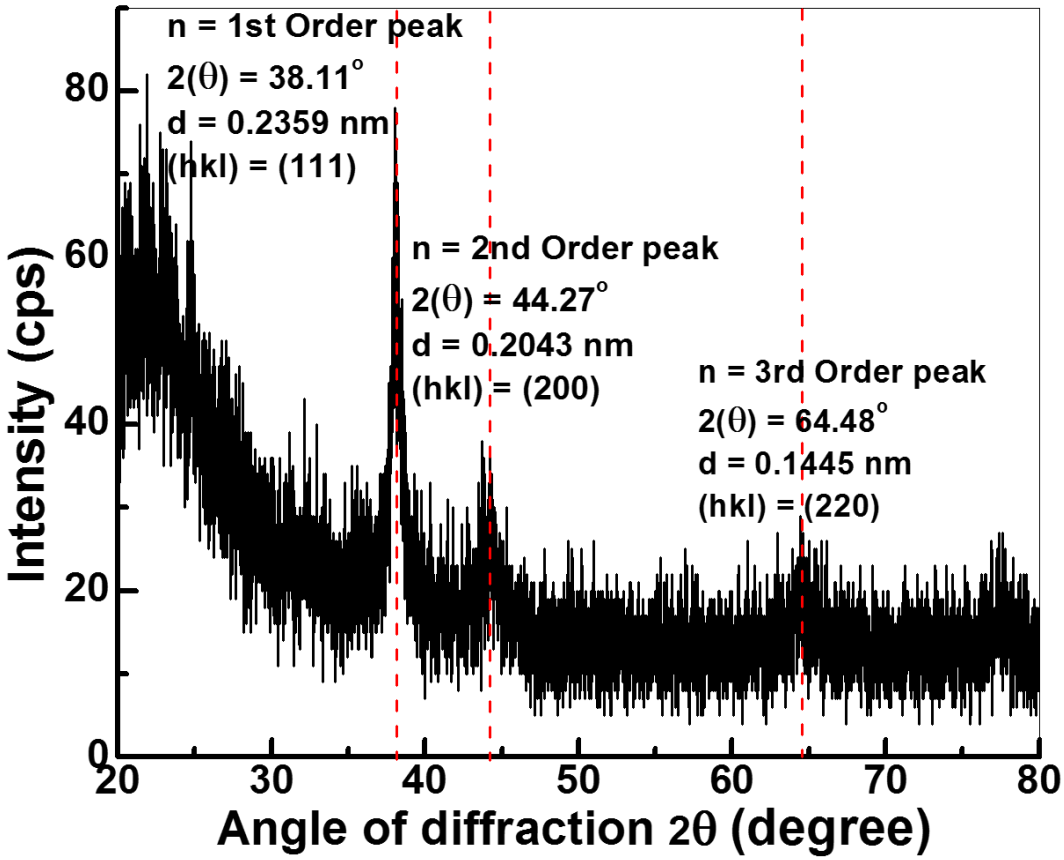

Figure 4.12. XRD spectral analysis of a 35 nm Ag film deposited on quartz substrate

From Bragg's law, $n\lambda = 2d\sin\theta$ and for a CuKα_1 source, $\lambda = 0.15406$ nm.

Calculations for 1st Order:

Plugging n=1, d = 0.2359 nm & (hkl) = (111) into the equation for lattice constant

$$a = d\,(h^2+k^2+l^2)^{1/2} = 0.2359\,(1+1+1)^{½}$$

$$a = 0.4086 \text{ nm}$$

(Verified with published value for Ag, a = 0.4086 nm [87] *)*

Thus, XRD confirms that the crystal structure of silver thin film used is FCC.

c) XRD spectra of a 400 nm Si_3N_4 film on a silicon substrate:

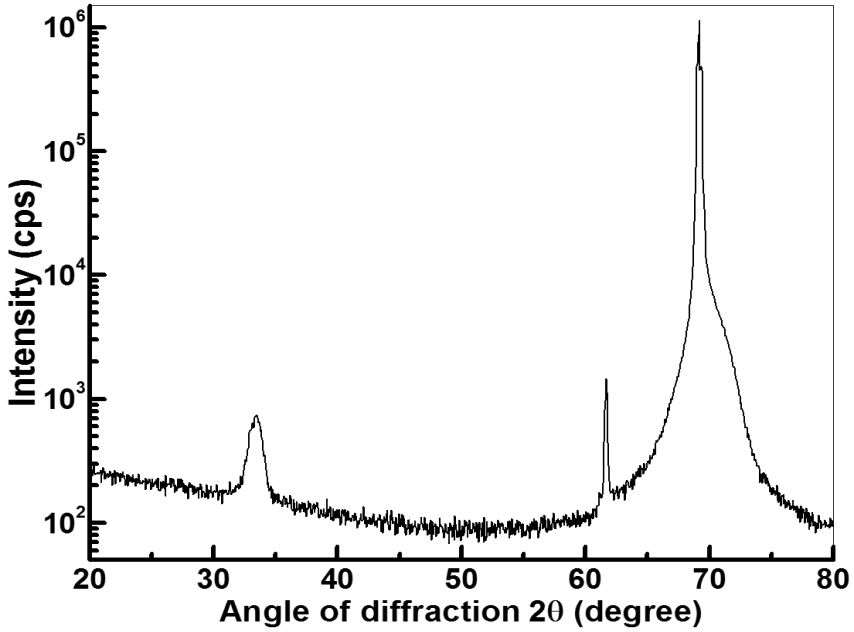

Figure 4.13 XRD spectrum of 400 nm Si_3N_4 thin film on a Silicon substrate

d) XRD spectra of a 500 nm HfO_2 film on a silicon substrate:

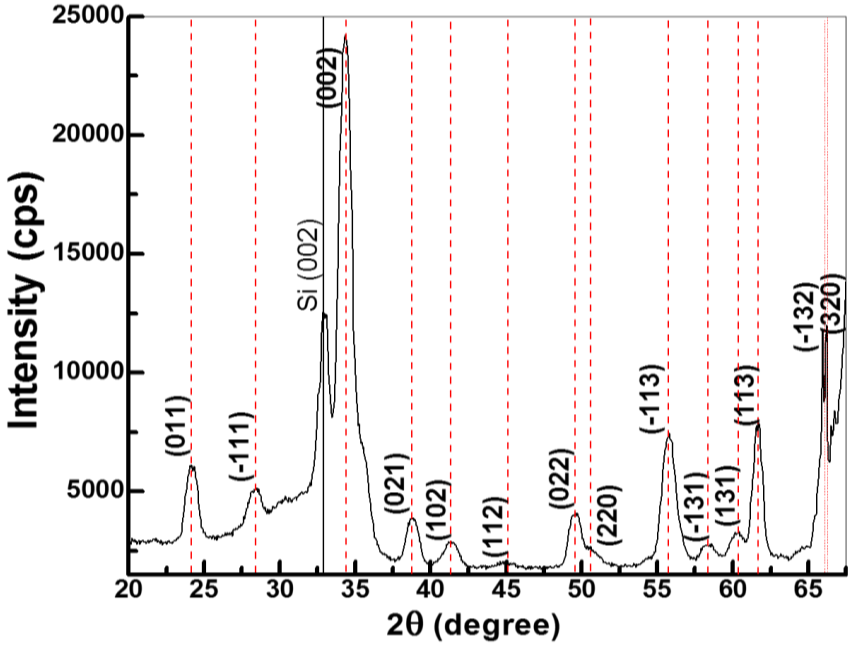

Figure 4.14 XRD spectra of a 500 nm HfO_2 film deposited on a silicon substrate

4.3.2. X-ray-Energy Dispersive Spectroscopy (X-EDS) for elemental composition

X-EDS is an analytical technique used for the elemental analysis or chemical characterization of a sample. It relies on an interaction of some source of X-ray excitation and a sample. Its characterization capabilities are due in large part to the fundamental principle that each element has a unique atomic structure allowing unique set of peaks on its X-ray emission spectrum. The number and energy of the X-rays emitted from a specimen can be measured by an energy-dispersive spectrometer. As the energies of the X-rays are characteristic of the difference in energy between the two shells and of the atomic structure of the emitting element, EDS allows the elemental composition of the specimen to be measured.

a) X-EDS scan of the Au thin film on quartz substrate

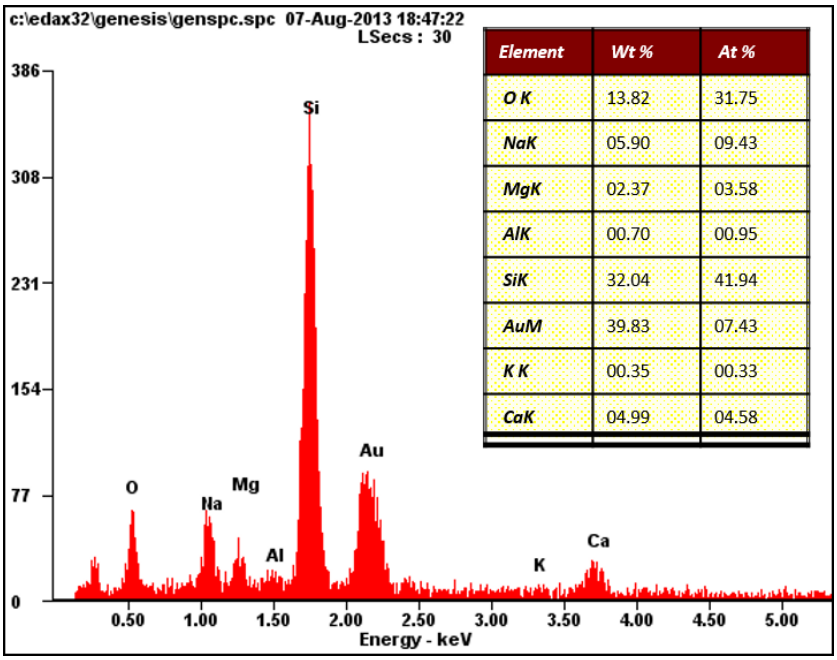

Element	Wt %	At %
O K	13.82	31.75
NaK	05.90	09.43
MgK	02.37	03.58
AlK	00.70	00.95
SiK	32.04	41.94
AuM	39.83	07.43
K K	00.35	00.33
CaK	04.99	04.58

Figure 4.15. EDS spectra of the 30 nm gold thin film at 15 kV accelerating voltage and the inset table shows elemental composition by wt.%

b) X-EDS scan of the Ag thin film on quartz substrate

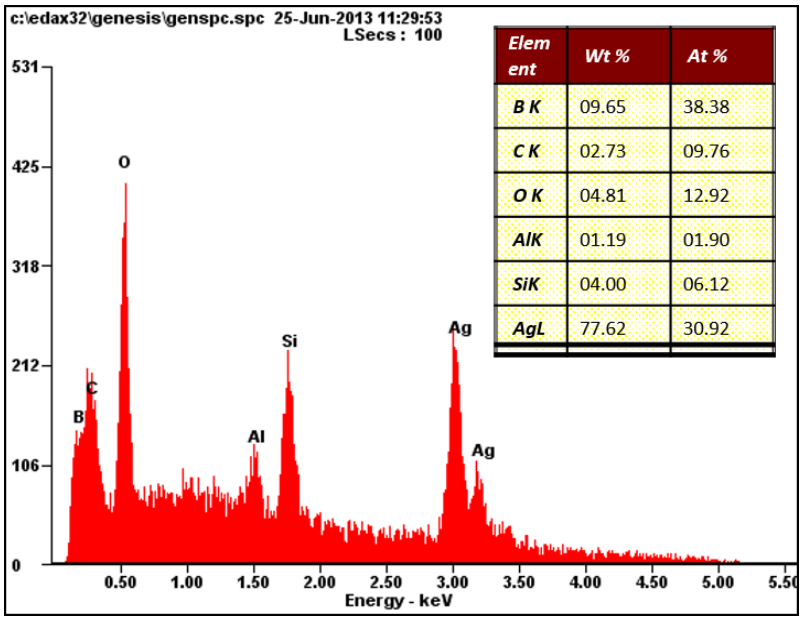

Figure 4.16. EDS spectra of the 35 nm silver thin film at 5 kV accelerating voltage and the inset table shows elemental composition by wt.%

c) X-EDS scan of Bi-WCSPR sensor, Ag(35)/Si_3N_4(100)/Au(28), on quartz substrate

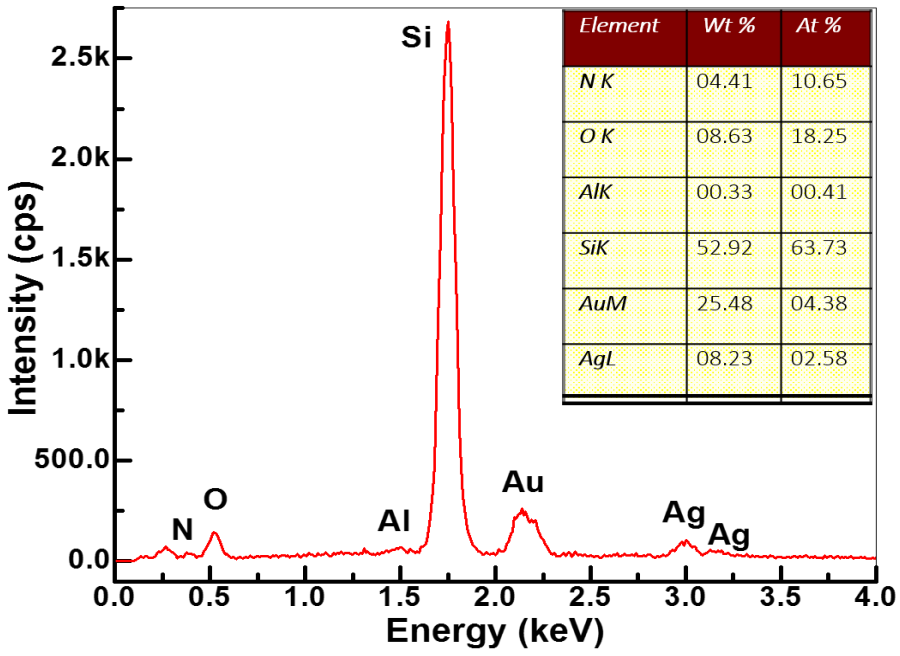

Figure 4.17 X-EDS spectrum of a Bi-WCSPR sensor- Ag(35)/Si_3N_4(100)/Au(28) at 5 kV accelerating voltage, and the inset table shows elemental composition by wt.%

d) X-EDS scan of Bi-WCSPR sensor Ag(35)/Si_3N_4(100)/Au(28), coated with a thin film of CdSe/ZnS QDs

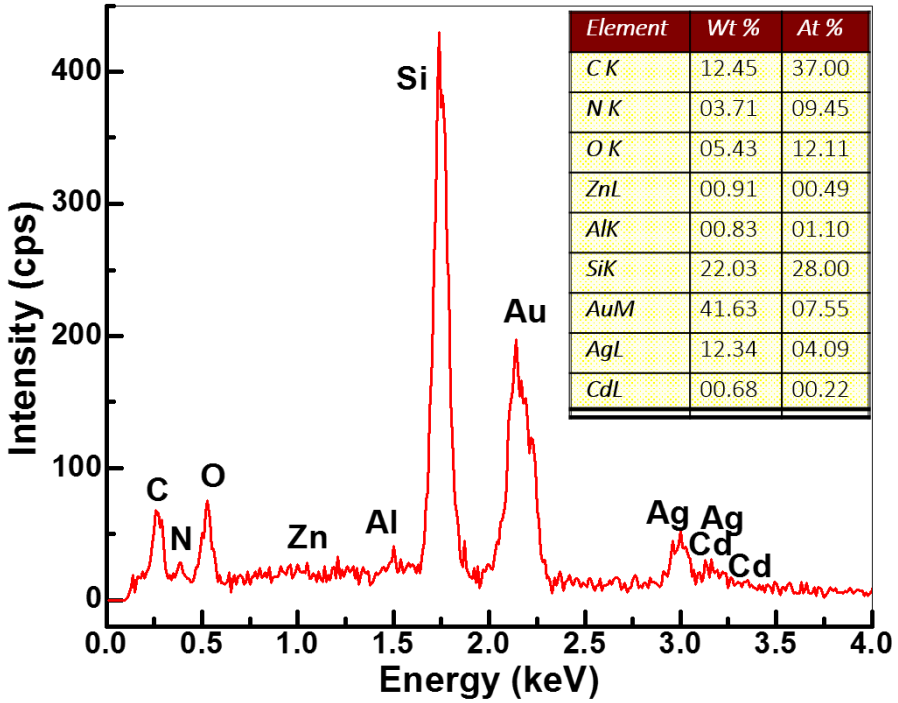

Figure 4.18 X-EDS spectrum of a Bi-WCSPR sensor- Ag(35)/Si_3N_4(100)/Au(28), coated with a thin film of CdSe/ZnS, measured at 5 kV accelerating voltage. The inset table shows elemental composition by wt.%

Conclusion for X-EDS measurements:

- The characteristic peaks of Ag & Au are present in corresponding thin films under examination, confirming its elemental composition.
- Si & O peaks are also visible in all the EDS spectra, which are known to be occurring from the quartz glass substrate (composed of silica SiO_2). This is due to the penetration of the high energy electron beams into the substrate of the specimen.
- The signals from the Si & O (coming from the substrate) is seen to be eliminated by reducing the accelerating voltage of the electron beam.

4.3.3. Atomic force microscopy (AFM) for surface morphology & thickness measurement

AFM is a kind of scanning probe microscope, which utilizes a solid & sharp probe tip to scan/examine the material. It examines surface features whose dimensions range from atomic spacing to a tenth of a millimeter. AFM uses near-field forces between atoms of the probe tip apex and the surface of the specimen to generate signals of surface topography. In case of optical and electron microscopy, the resolution is limited to the sub-wavelength scales due to the *far-field interactions* between light or electron waves and specimens. Whereas the near-field characteristic of atomic forces not only eliminates this resolution limit associated with diffraction of light or electron waves but also enable us to obtain a true image of surface atoms.

a) Surface topography of a 30 nm gold film using contact mode of AFM

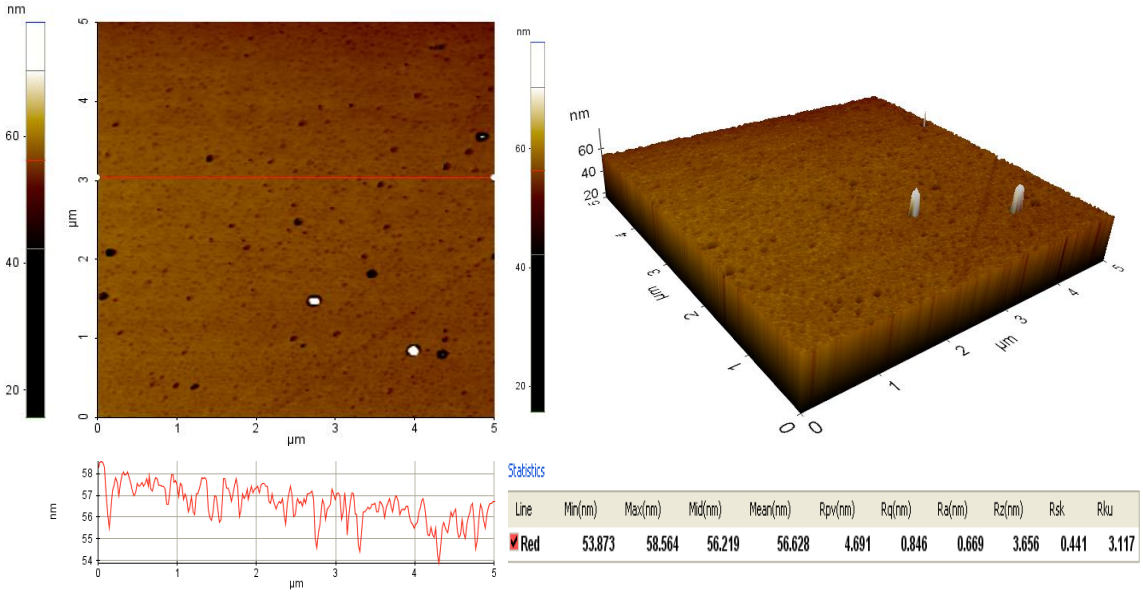

Figure 4.19 Surface topography of a (5x5) µm region of 30 nm Au film using AFM tip in a non-contact mode at a scanning rate of 0.5 Hertz

b) Surface topography of a 35 nm silver film using contact mode of AFM

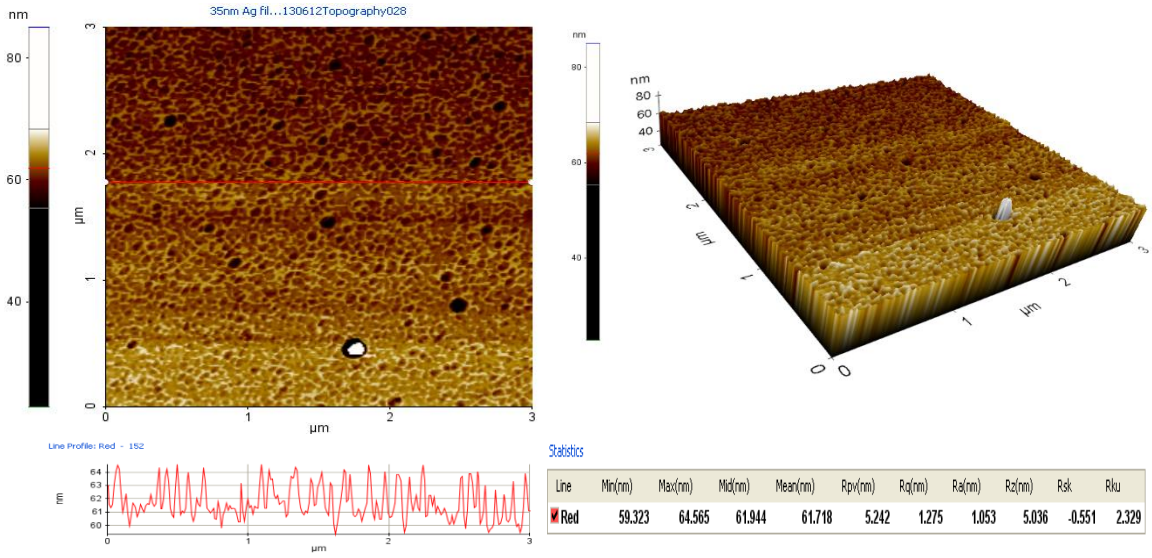

Figure 4.20 Surface topography of a (3x3) µm region of 35 nm Ag film using AFM tip in a non-contact mode at a scanning rate of 0.1 Hertz

A typical AFM scan of a gold and a silver thin film are shown in figure 4.19 and 4.20, respectively. The quartz crystal film thickness monitor and the step IQ profilometer confirms that the gold film is 30 nm thick and the silver film is 35 nm thick. The smoothness of the surface topography in both the cases are characterized by a root-mean-square deviation of about 4 to 5 nm. The line profile (red colored) across the (5 x 5) µm scan region of the 30 nm gold film clearly indicates that the overall surface roughness of the film is ~ 4nm, whereas the same in the case of (3 x 3) µm region of the 35 nm silver film indicates a surface roughness of ~ 5 nm. The thickness of a thin film can also be determined by scanning the AFM tip at the edge of the film in a non-contact mode, as shown in the next section.

c) Thickness measurement of a gold (Au) thin film by scanning the AFM tip in a non-contact mode across a step height/edge

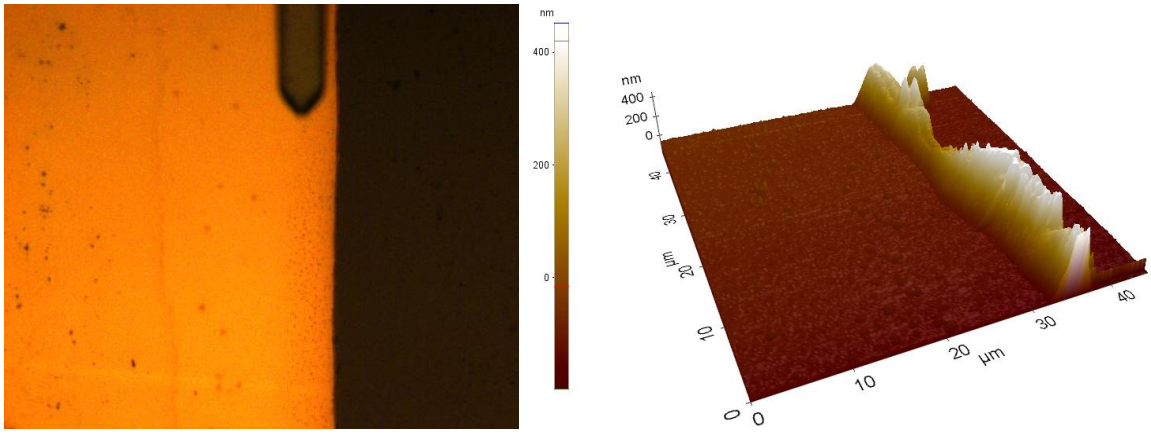

Figure 4.21 Image of the AFM tip at an edge of the gold film and the topography data for the same region

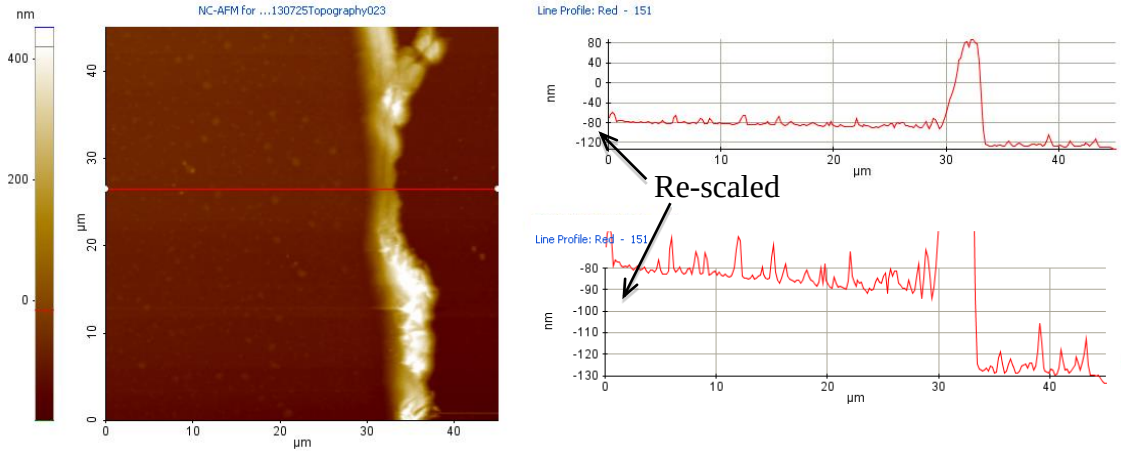

Figure 4.22 Line profile of the scanning probe across the step height indicates the thickness of the film to be around 40 nm.

It is pretty much evident from the line profile graphs in Figure 4.21 and 4.22 that the difference of the topographical average on the two sides of the step height gives the thickness of the gold film to be around 35-40 nm.

4.3.4. Spectroscopic ellipsometry

Ellipsometry is an optical technique for investigating the dielectric properties (complex refractive index or dielectric function) of thin films. It is very sensitive to the change in the optical response of incident radiation that interacts with the material being investigated. Typically, the measured signal is the change in polarization as the incident radiation interacts with the material structure of interest. Because the signal depends on the thickness as well as the materials properties, ellipsometry can be a universal tool for contact free determination of thickness and optical constants of films of all kinds.

a) Spectroscopic ellipsometry of Si_3N_4 thin film

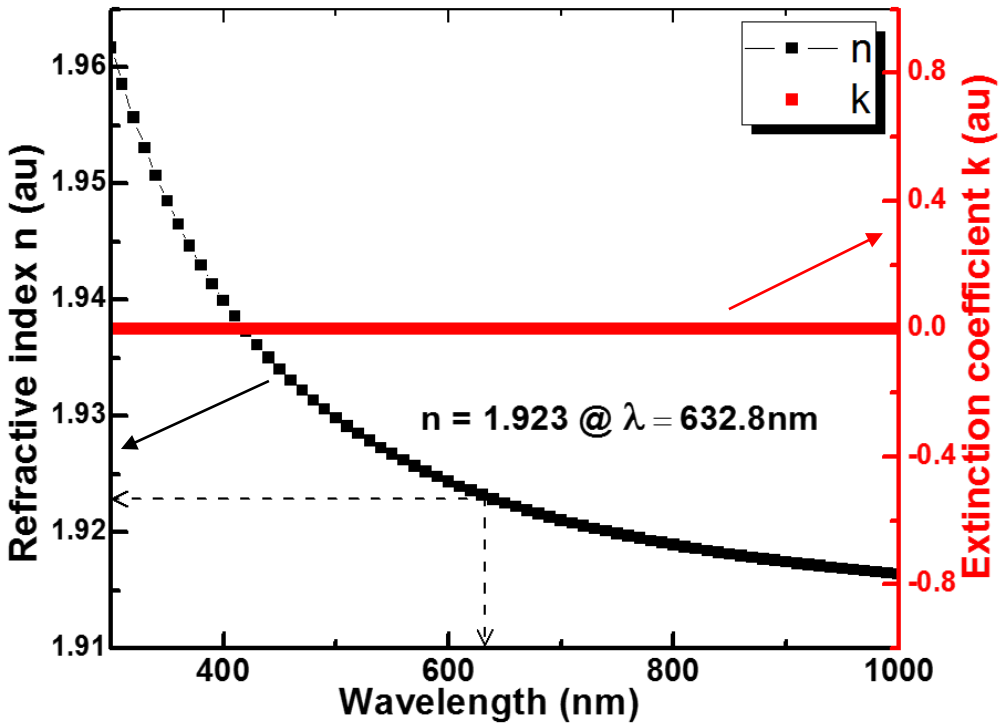

Figure 4.23 The image shows the refractive index and extinction coefficient values for Si_3N_4 thin film as a function of wavelength

b) Spectroscopic ellipsometry of HfO_2 thin film

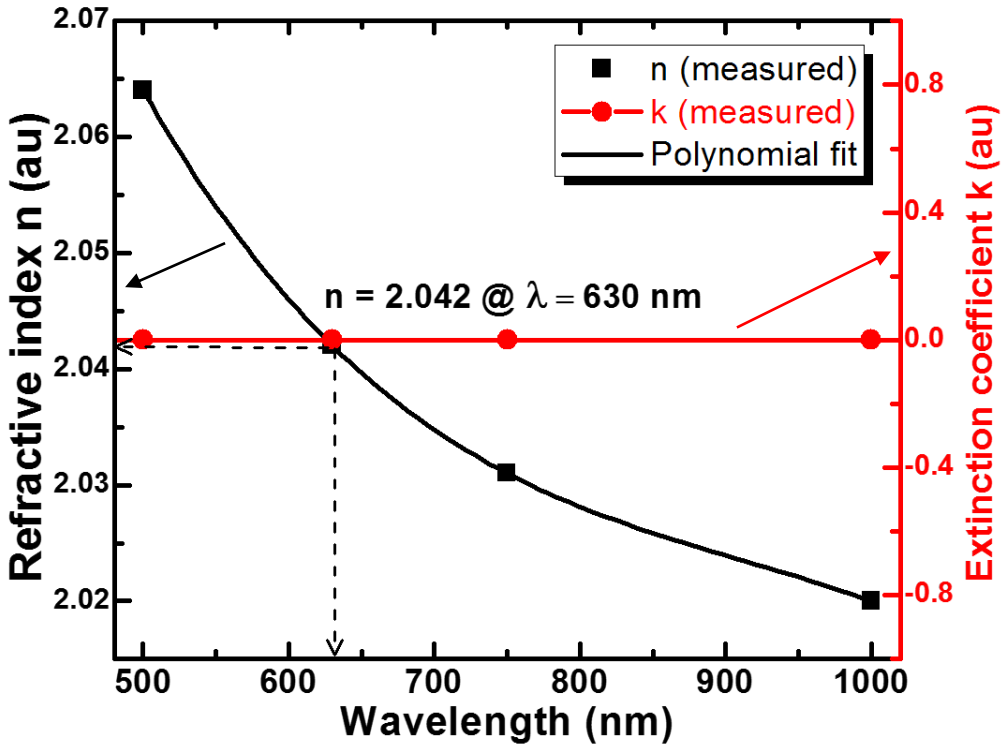

Figure 4.24 The image shows the refractive index and extinction coefficient values for Si_3N_4 thin film as a function of wavelength

As mentioned earlier, the refractive index of dielectric thin films (Si_3N_4, HfO_2), used as waveguide media in the multilayered sensors, is significantly governed by the growth conditions. In order to confirm the refractive index consistency of the waveguide layers used, they were characterized on the ellipsometer for their refractive indices (n) and extinction coefficients (k). The refractive index of Si_3N_4 and HfO_2 thin films, deposited and thus used in the multilayered sensors presented in this work, were found to be 1.923 and 2.042 at a wavelength of 632.8 nm (as shown in figure 7.23 and 7.24). Whereas, the extinction coefficient of these films were measured to be negligible (zero) for a wide range of wavelengths (300 to 1600 nm).

Characterization of gold nanoparticles (Au NPs)

4.3.5. UV-VISIBLE absorption and emission of Au-NPs

The gold nanoparticles, used in the investigation of evidence of surface plasmons in liquid crystal composites containing different concentrations of Au NP dispersions, were characterized for their UV-VIS absorption and emission spectroscopy. These Au NPs are highly soluble in distilled water and so were used in the water solvent for all the measurements pertaining to these NPs.

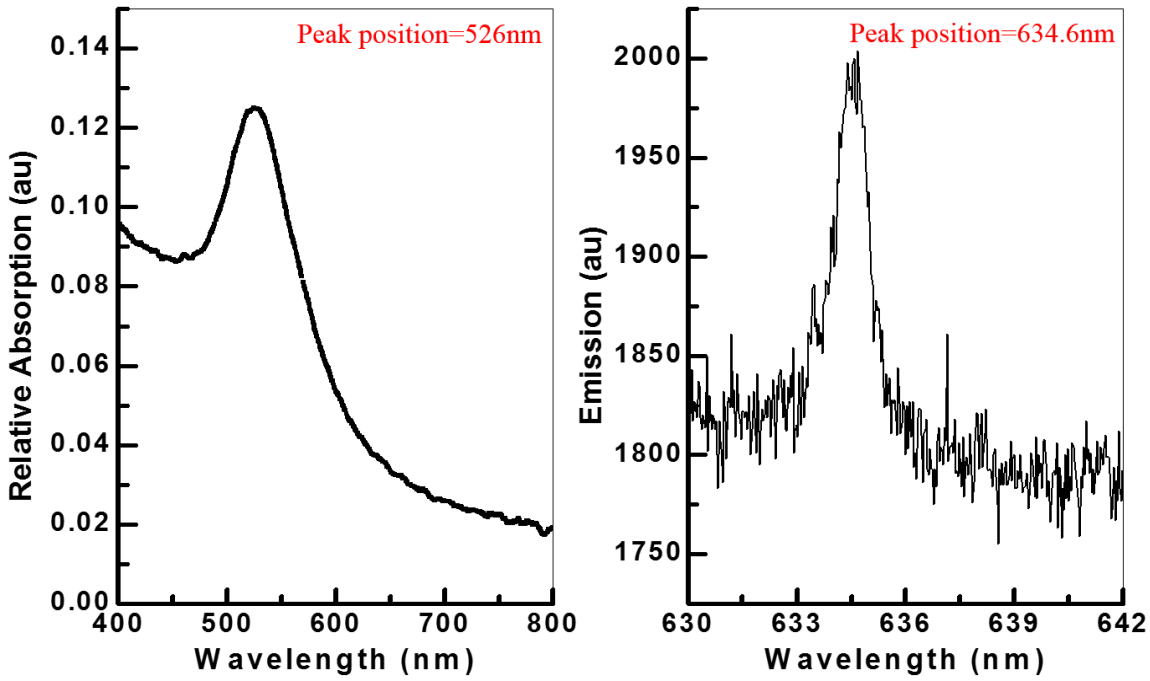

Figure 4.25 The characteristic absorption and emission spectra of 10^{-10} mol/l gold nanoparticle dispersions in water

The above two graphs (in figure 4.25) shows the absorption and emission spectra of these Au NPs having a concentration of 10^{-10} mol/l. The peak positions centered at 526 nm and 634 nm corresponding to absorption and luminescence by these NPs, respectively, are known to be characteristics of 14-nm diameter Au NPs.

4.3.6. HR-TEM images of the Au NPs

The HR-TEM model used, Hitachi H-9500, is an ultra-high resolution microscope with an accelerated voltage of 300 kV; a point-to-point resolution of 0.18 nm and a lattice resolution of 0.10 nm. A *SC-1000* Orius® *TEM CCD Camera* (4008 x 2672 pixels) is attached to the microscope, which allows quick and efficient searching of areas within the sample and viewing and recording high resolution images with ease. An *EDAX* EDS system is also attached to the H-9500 allowing chemical analysis at the nanoscale.

The figures 4.26 and 4.27 show (HR-TEM) images of the Au NPs used in this dissertation. As mentioned earlier, these Au NPs are highly soluble in distilled water and so did not require any sort of sample preparation process for imaging. A drop of solvent containing these NPs was placed on the sample holder (a wire mesh) and was allowed to sit until the water drop was evaporated.

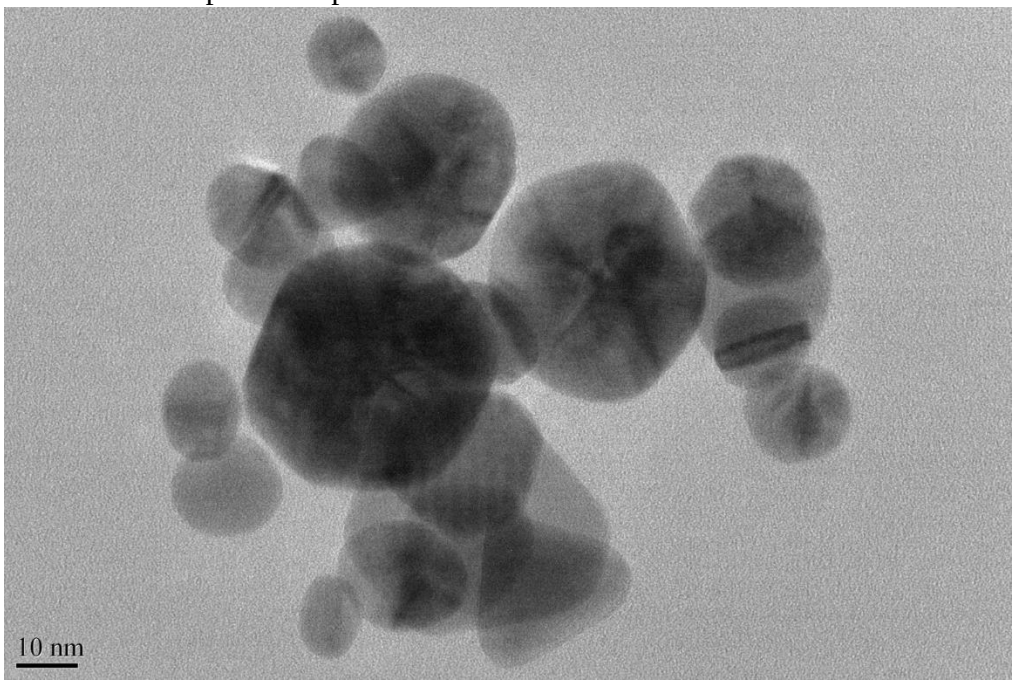

Figure 4.26 HR-TEM of Au NPs with an average diameter of 14 nm

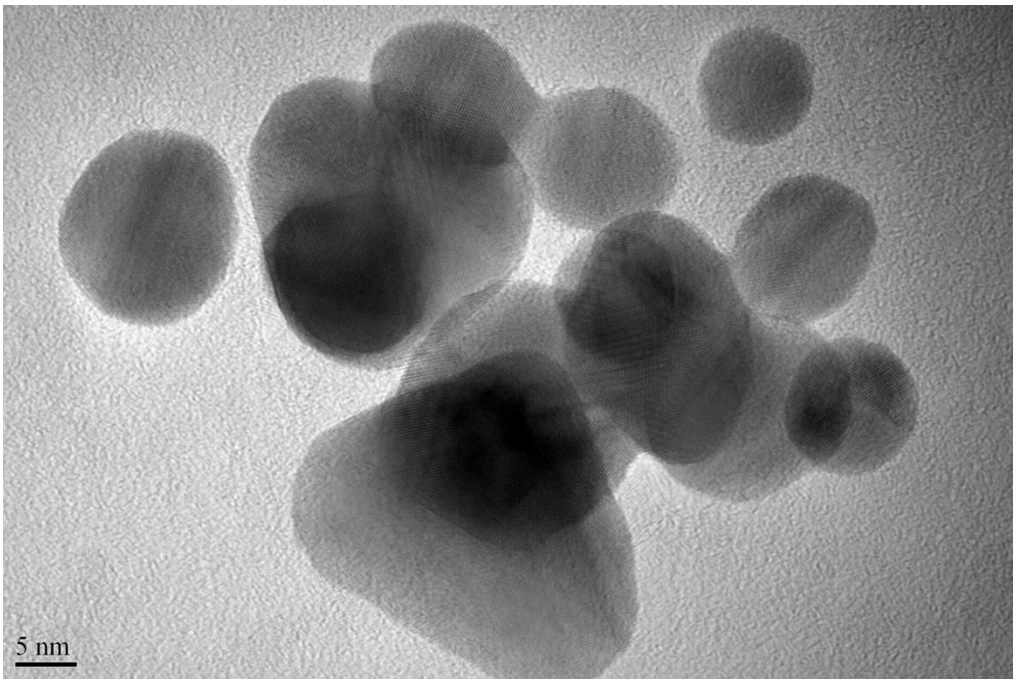

Figure 4.27 HR-TEM of Au NPs with an average diameter of 14 nm

The average size distribution of these Au NPs was measured to be around 15 nm which is in close agreement with the inferred size of the same particles (~14 nm), measured from the absorption and emission spectra. It is clearly evident from the images that some of the Au NPs are as big as ~35 nm and some are under 10 nm. But still, the overall optical response from a solution containing these NPs confirms the dominance of the smaller sized particles averaging around 14 to 15 nm.

4.3.7 Confocal microscopy images of liquid crystal and Au NPs composites

Once the liquid crystal composites with different concentrations of Au NPs were evaluated for their surface plasmon resonance (SPR) measurements, the glass slide holding/coupling the sample with the prism base was separated for its imaging. This glass

slide was examined by confocal microscopy using Zeiss LSM-510 Meta confocal microscopy system.

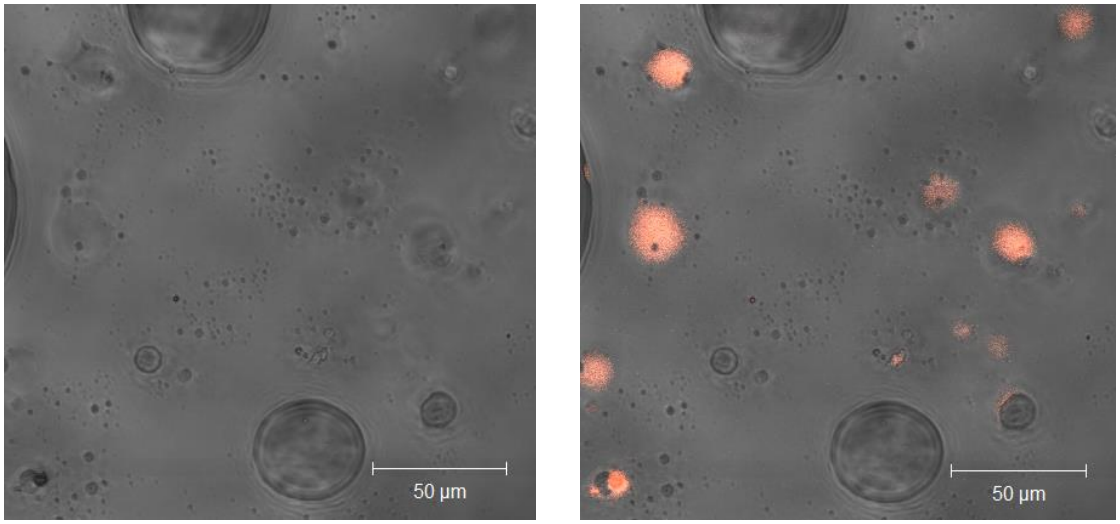

Figure 4.28 Confocal microscopy images of a composite sample, LC and 35 wt.% dispersion of Au NPs in water, under white source and 543/488 nm (25/25%) irradiation

Resulting confocal microscopy images of sample containing LC and 35 wt.% dispersion of Au NPs in water, are shown in figure 4.28. When illuminated with white light (left image), we observe several spherical structures without any luminescence from Au NPs. The spherical features range in size, from very small (<< µm) to as large as 20–40 µm. They appear to be water droplets formed in an immiscible mixture of LC and NPs dispersing medium (water). Prominent luminescence from Au NPs is visible only when the sample is illuminated with 543/488 nm (25/25%) radiation (right panel), confirming the presence of Au NPs dispersed in the liquid crystal media [2].

4.3.8 SEM and X-EDS images of Au-NPs dispersed in E44 liquid crystal

The Hitachi S-3000N variable pressure SEM was used for imaging the liquid crystal samples containing dispersions of Au-NPs. This SEM has 3.0 nm resolution at high vacuum and 4.0 nm resolution at low vacuum, controlled by the computer for ultimate ease of use. This SEM can examine insulating and biological samples at low vacuum without the need of coating a conductive layer on the sample surface. This SEM is attached with an X-EDS system allowing chemical composition analysis and elemental mapping.

As shown in figure 4.29 below, several composite samples of E44 liquid crystal in its nematic phase containing different wt.% dispersion of 10^{-10} mol/l Au NPs in water, were imaged using the SEM, in order to get more insight about the distribution of Au-NPs within the LC media. Despite of the capability of the instrument for imaging insulating materials, all our samples were sputtered coated with 4-5 nm thin film of silver, in order to get a better

Figure 4.29 Several composite samples of LC and dispersion of Au NPs loaded together on the sample stage for imaging in S-3000N SEM

quality images. The figure below shows the SEM image of one of the samples, LC + 35 wt.% dispersion of Au NPs. It is pretty evident from this image that the LC molecules within the sample, self assembles and forms big clusters/lumps having a spatial dimension of 30-50 μm, which could mediate/govern the arrangement of Au NPs dispersed into it.

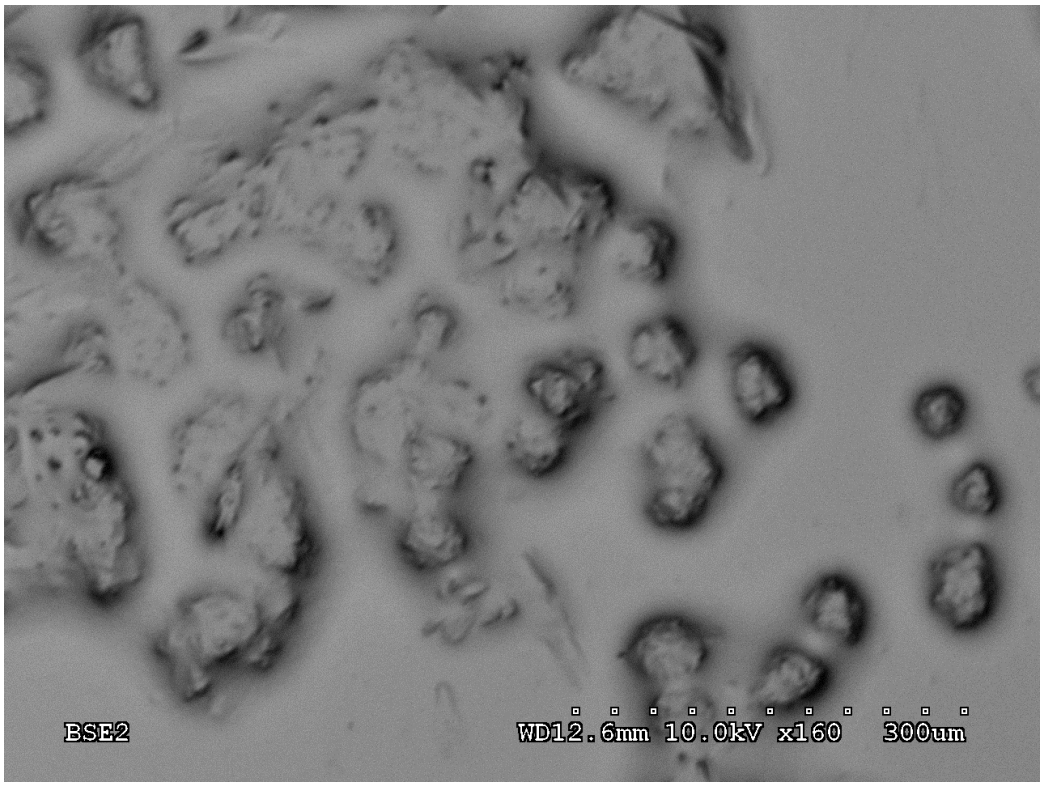

Figure 4.30 SEM-micrograph showing a composite sample of E44 LC molecules in its nematic phase, having a dispersion of Au NPs

In order to confirm the presence of Au NPs in the above image, we have carried out X-EDS measurement over the same region for the characterization of its elemental composition. As shown in the inset of figure 4.31, the EDS line scan was measured over the white colored line shown in the micrograph. The EDS spectrum collected over this line scan is shown plotted in the graph of figure 4.31. The sharp peaks observed in the graph for silver and carbon are not labelled by choice, since the sample itself was sputtered coated

with silver thin film, and the sputter chamber being used is also employed for coating carbon films. The presence of Au NPs, though in a very small concentration, are evident from the weak emission peaks corresponding to M shell de-excitation at around 2.120 keV.

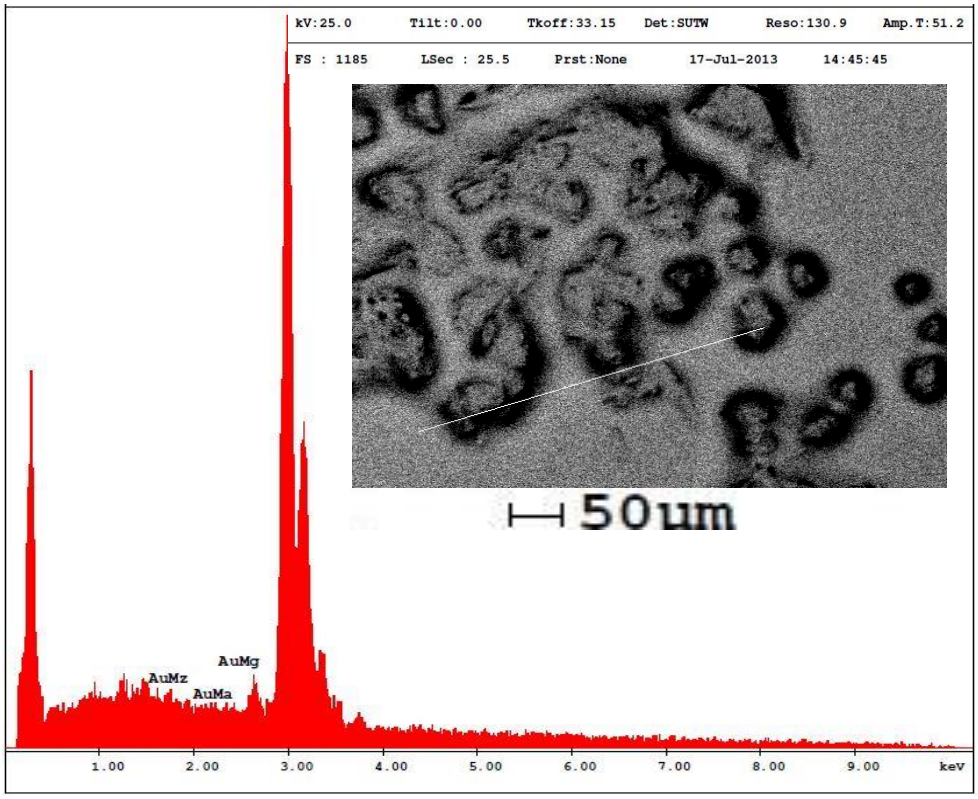

Figure 4.31 X-EDS spectra of the LC composite containing Au NPs dispersions, scanned along the white line indicated in the inset

4.3.9 Optical microscopy & polarized phase microscopy of LCs and defects in LCs

Since the liquid crystals molecules observe optical anisotropy, a good quality imaging of such (birefringent) specimen can be achieved through contrast enhancing technique like polarized light microscopy. The image contrast arises from the interaction of plane polarized light with the birefringent specimen to produce two orthogonally polarized wave components (ordinary & extra-ordinary). Since the velocities of these components are different and vary with the propagation direction, after exiting the specimen they can be recombined (by constructive & destructive interference) when they are passed through an analyzer on their pathway.

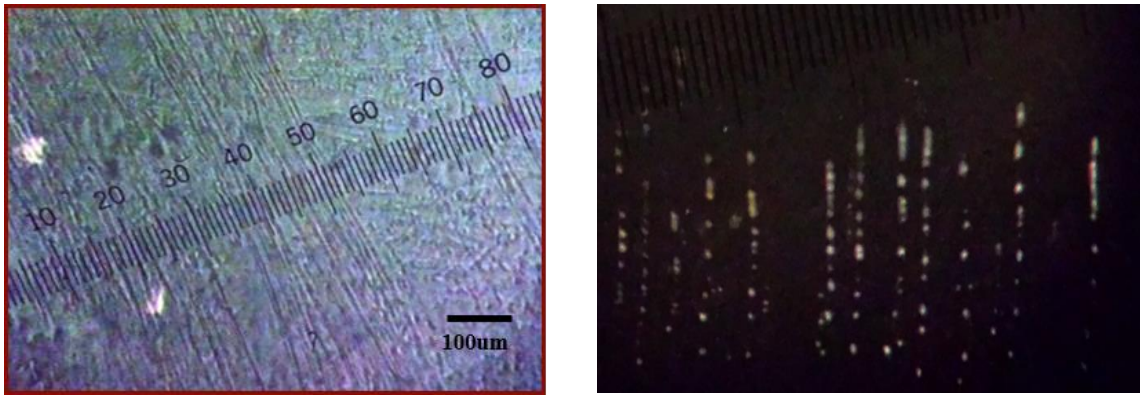

Figure 4. 32 The left panel shows preferential alignment of LC directors along the grooves of a patterned ITO glass slide. The right panel shows the same sample under cross polarizers.

An ITO-coated glass slide was patterned with periodic groove structure with intergroove separation of about 10μm. A 200X Nikon Optiphot microscope equipped with 100 line/mm ruled micro-scale was used to examine groove structures. The grooves were produced by using the standard practice of unidirectional rubbing of ITO surface by velvet, which produces more-or-less periodic groove structure and facilitates preferential alignment of LC directors within grooves, as shown in the left panel of figure 4.32. The

same glass slide, holding the patterned LCs, were later on imaged using a polarized light microscopy arrangement, as shown in the right panel.

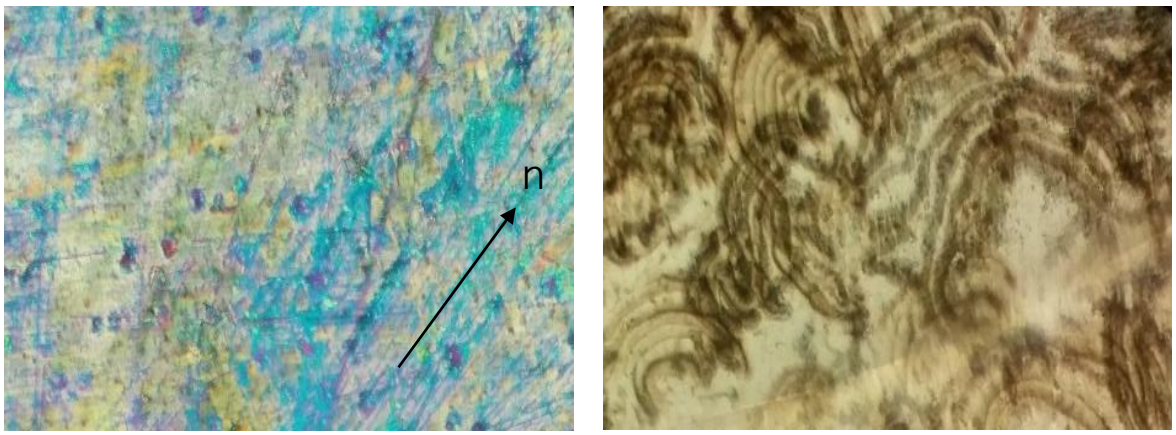

Figure 4.33 The left panel shows polarized optical photo-micrograph of E44 LC confined in a 40 μm thick cell, showing the preferential alignment of LC molecular director n. The right panel shows formation of defects in another LC cell embedded with silica (SiO_2) beads, across which external *AC* fields of the order 10^6 V/m @ 1kHz frequency were applied. These defects mimick a ribbon like structure due to the application of high *AC* fields

4.3.10 UV-VIS Absorption and Fluorescence spectroscopy of CdSe/ZnS quantum dots

The semiconductor quantum dots used in this dissertation were characterized for their UV-VIS absorption spectrum, fluorescence emission spectrum, high-resolution SEM imaging, and X-EDS analysis for its elemental composition (shown earlier).

CdSe/ZnS QDs used in this dissertation were dissolved in chloroform solution for their absorption and emission spectrum measurements. The absorbance spectrum of these QDs (as shown in figure 4.34), was measured using UV-3600, UV-VIS-NIR Spectrophotometer from Shimadzu. This equipment uses a tungsten lamp as radiation source and a PMT (photo-multiplier tube) detector in the visible region. Though the absorbance spectrum was measured from 200 nm to 800 nm, the above graph has been

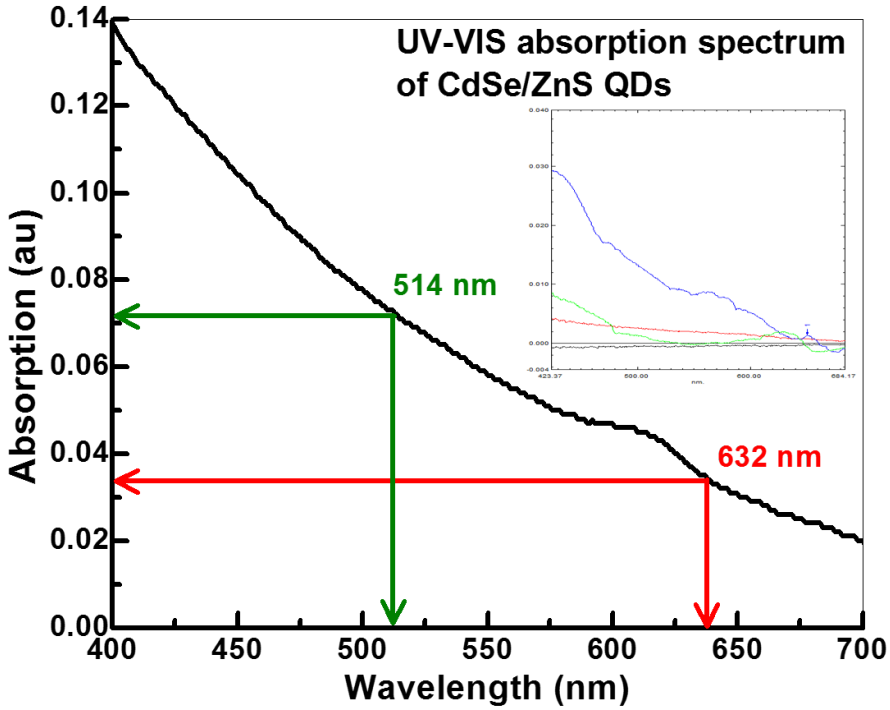

Figure 4.34 UV-VIS absorption spectrum of CdSe/ZnS quantum dots dispersed in chloroform solution. The inset shows the absorption spectra for several different concentrations.

rescaled to show only the visible wavelengths in the range 400 to 700 nm. The inset within figure# shows the absorption spectra measured for several different concentrations of these QDs dispersed in chloroform.

The emission spectrum for the same QDs dispersed in chloroform was measured with an RF-5301PC Spectrofluorometer from Shimadzu. This equipment uses a 150 W xenon lamp as the incident source of radiation, and a PMT detector for the analysis of emitted wavelengths in visible range. The emission spectrum of these QDs were also measured using the 2-W water cooled Spectra Physics Ar-ion laser (λ=514nm), as a part of our investigation, which shall be discussed in the results section. As shown in figure 4.35, the emission spectrum for these quantum dots shows a peak centered at 618.5 nm,

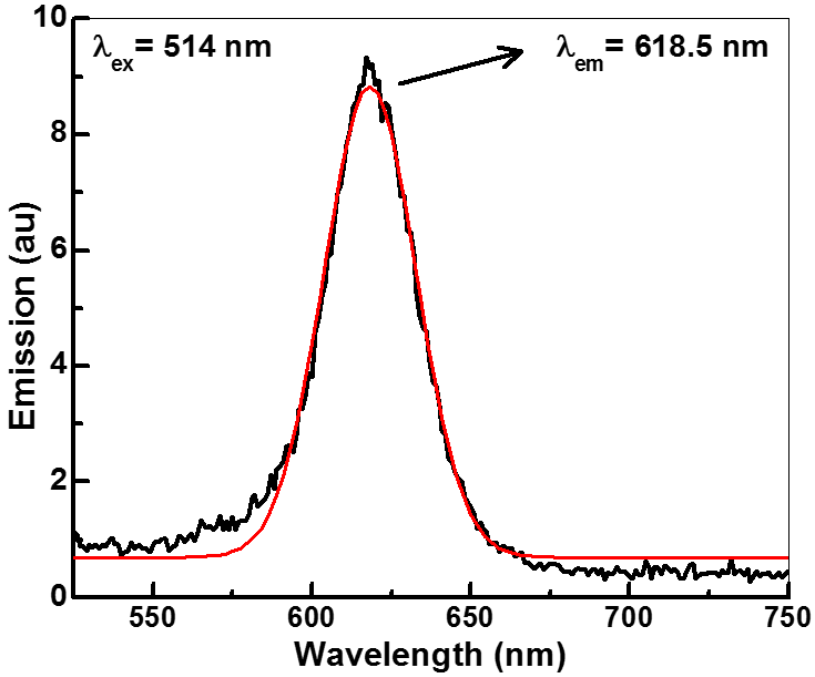

Figure 4.35 Emission spectrum of CdSe/ZnS QDs excited with 514 nm incident radiation

when excited with an incident wavelength of 514 nm. Whereas, the peak position for the emission spectrum of these QDs, when excited with 633 nm incident wavelength, shows a

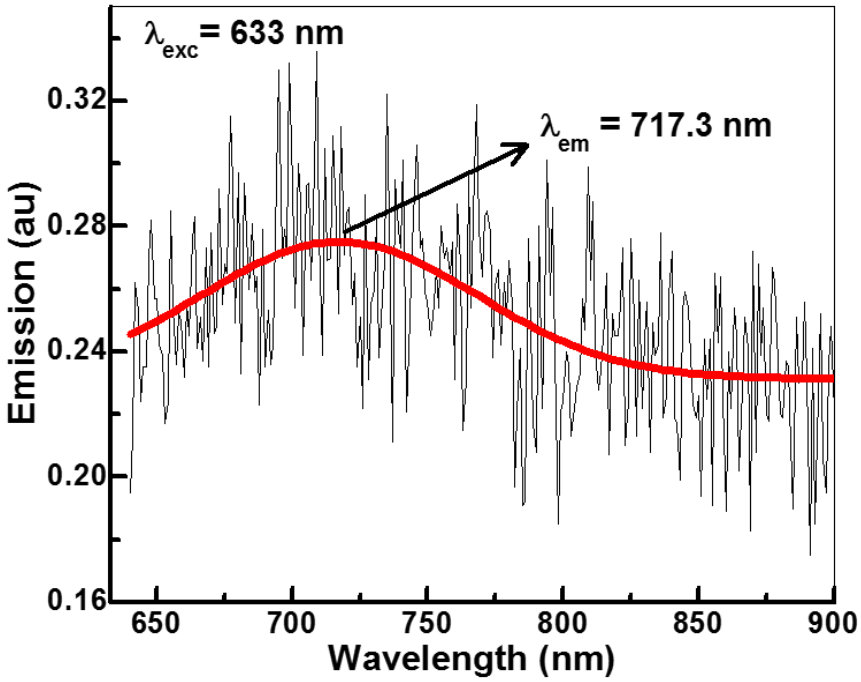

Figure 4.36. Emission spectrum for CdSe/ZnS QDs excited with 633 nm incident radiation

peak centered at 717.3 nm (shown in figure 4.36).

4.3.11 HR (High-resolution)-SEM and X-EDS of CdSe/ZnS QDs

The Hitachi S-4800 II Field Emission SEM was used to get the high resolution images of CdSe/ZnS quantum dots presented in this dissertation. This equipment is capable of ultra-low voltage imaging and handling large specimen upto 6" of a variety of sample types. This SEM has a resolution of 1.0 nm, a variable accelerating voltage of 0.5 to 30 kV, and is equipped with an X-EDS system for analysis of chemical composition of the specimen. A thin film of CdSe/ZnS quantum dots (which were originally dispersed in chloroform) coated on the surface of bimetallic-waveguide coupled SPR sensor (Ag{35}/Si_3N_4{100}/Au{28}), was imaged under the HR-SEM equipment, as shown in figure 4.37. The QDs dispersed in chloroform, once coated on the sensor surface, are agglomerated into big clusters due to the quick evaporation of chloroform solution after being exposed to the environment. Most of these clusters have an average diameter in the

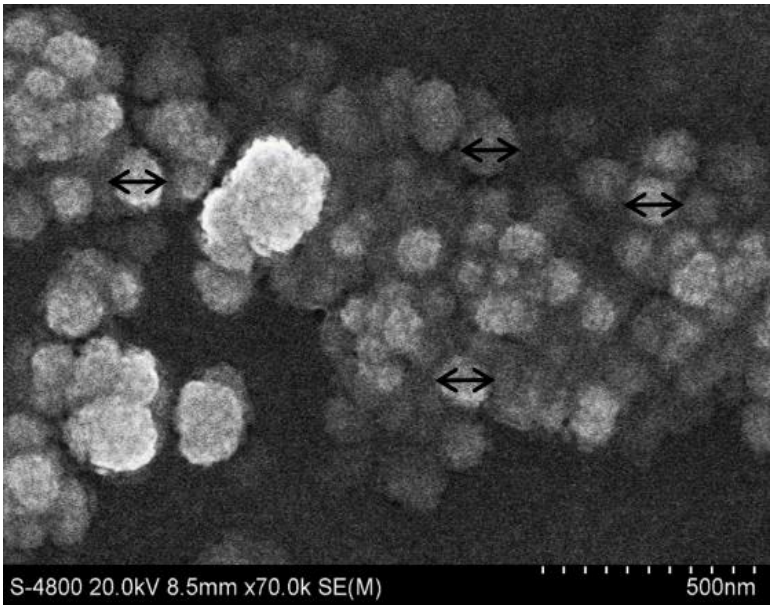

Figure 4.37 HR-SEM image of the CdSe/ZnS QDs coated on the sensor surface

range of 100 to 125 nm, except few which may be as big as 225 nm in diameter. But the overall PL emission from this QD thin film sample coated on the sensor surface (as shown in figure 5.21), retains almost the same PL emission wavelength observed in case of as received QDs from the manufacturers (figure 4.35).

This sample was investigated for its photo-luminescent properties under the influence of surface plasmon related fields excited at the sensor surface. The X-EDS analysis of this thin film sample was carried out and is as shown in figure 4.38. It is evitable from these results that the thin film of CdSe/ZnS QDs under investigation of its SPR induced PL characteristics, are in contact with the sensor surface. The X-EDS spectrum shows characteristic peak from each of the composite thin film of the multilayer SPR sensor (Ag, Si_3N_4, Au), as well as some of the composite elements of the QD thin film (Cd, Zn) coated over the sensor surface.

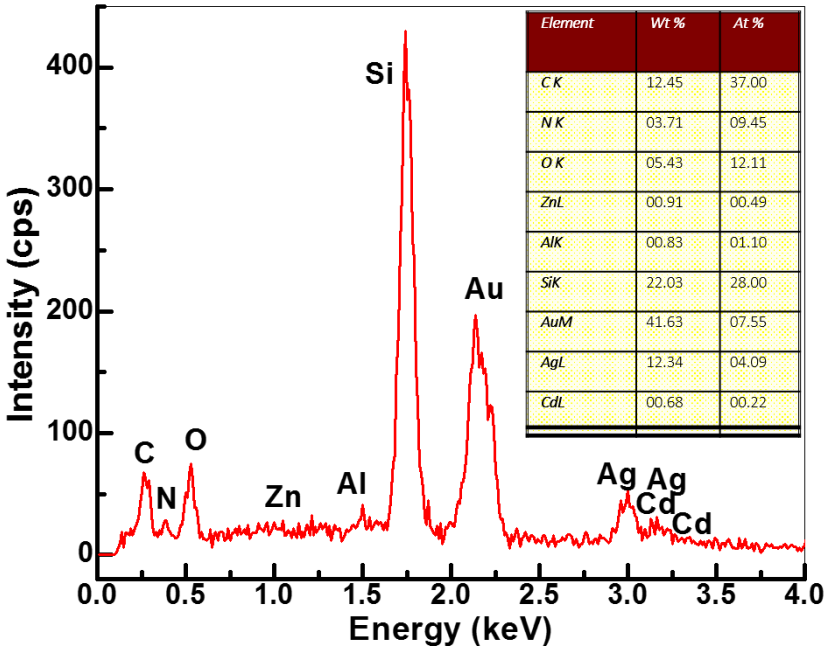

Figure 4.38 X-EDS spectrum of the QD thin film coated on the multilayered sensor surface

Chapter 5

RESULTS AND DISCUSSIONS

5.1 Surface plasmons in liquid crystals containing gold nanoparticles

We present evidence for surface plasmons (SPs) in a nematic liquid crystal (LC) containing dispersion of gold nanoparticles (Au NPs). The evidence originates from observations of attenuated total reflection (ATR) of p-polarized laser incident upon a high-index prism/LC-Au NPs/glass structure. SPs are generated through evanescent waves interacting with Au NPs embedded in the LC and NPs' dispersing medium.

5.1.1 Effects of Au NPs on electro-optical properties of a polymer dispersed liquid crystal

It is known that certain properties of liquid-crystal (LC) and polymer-dispersed liquid crystal (PDLC) materials can be changed very significantly by incorporating small concentrations of metal nanoparticles (NPs). Noteworthy are examples, in which the inclusion of metal NPs makes it more cost-effective to operate PDLC-based devices [1, 44-50]. PDLCs are composite materials consisting of submicron-size droplets of LC embedded within a polymer matrix. In the absence of external fields, the LC molecules are oriented randomly, the scattering of light dominates, and so the PDLC appears opaque. Application of sufficiently strong electric fields aligns LC molecules and transmission through the PDLC increases, often-approaching 100% at high fields. Displays, light shutters, and smart windows are among devices that make use of PDLC technology [51-53]. The motivation behind the proposed investigation came from the evidence of relatively large changes in the electro-optical properties of polymer dispersed liquid crystal (PDLC)

reported earlier by our group, shown in figure 5.1 [1]. In this, it was shown that the incorporation of small concentrations of metal NPs into PDLC structure can influence local electric fields, which in turn can bring about changes in the overall electro-optic response of the PDLC. For example, addition of only about 0.01 g of 10^{-10} mol/l dispersion of 14-nm diameter Au NPs to PDLC structure results in lower threshold voltage (by ~50%), increased optical transmission, and improved frequency response (shown in fig.1). As far as the physical mechanism(s) behind the observed changes in the electro optical properties of these materials is concerned, the local electric fields associated with surface plasmons (SPs) at Au-NPs/LC interface have been suggested [2].

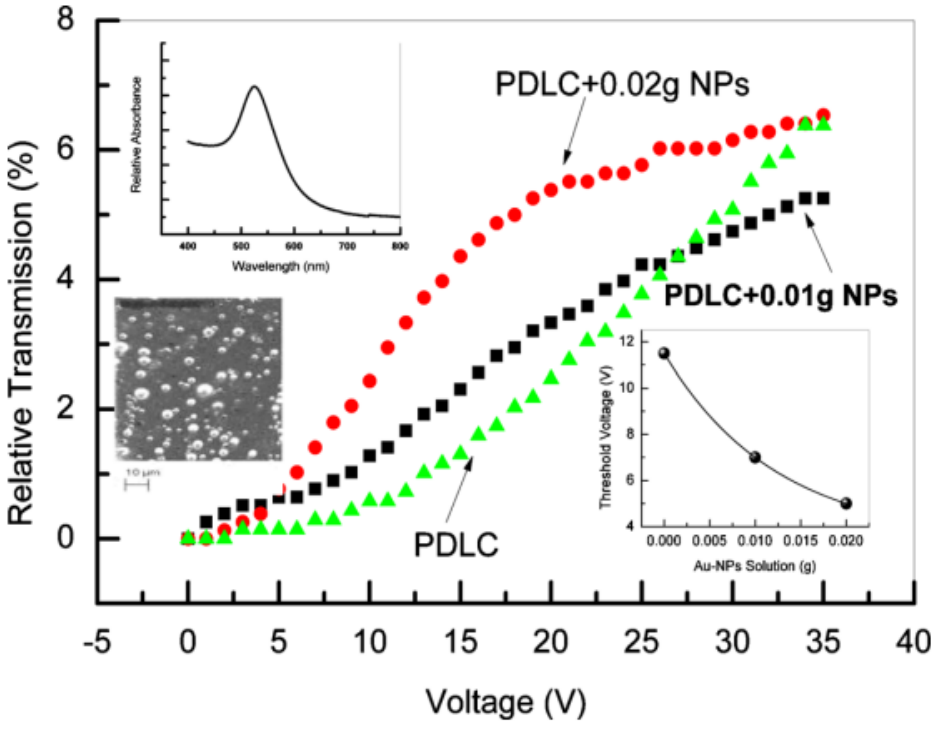

Figure 5.1. (i) Absorption spectrum of 10^{-10} mol/l Au NPs in water, (ii) SEM image of LC droplets, (iii) RT vs applied electric field (@ 1kHz), and (iv) threshold voltage vs relative concentration of Au NPs in PDLC [1].

Several other recent investigations have observed similar results [44,45,48]. For example, Ha et al. have also observed lower threshold voltage and faster response times in nematic LC doped with about 100 nm diameter Ti NPs. Similarly, Inam et al. and Pandey et al. have independently observed that relatively small concentrations of Au NPs (0.1 to 1 wt. %) decrease threshold voltage to switch an LC device from dark to bright, increase nematic to isotropic transition temperature, and modify device's frequency response. Additionally, several earlier investigations have observed similar results in that the addition of small concentrations of NPs to LCs can have rather large influence on LC properties.[50, 54-57]

5.1.2. Investigation of surface plasmons in a LC containing Au NPs

An obvious connection between the noble metal NPs and electro-optical properties of PDLCs is through the surface plasmon-induced electric fields in the material. In the present work, we provide direct evidence for SPs in LC samples containing small concentrations of Au NPs. As discussed in theory section, depending upon whether the noble metal in contact with LC is in the form of a thin film (Kretschmann or Otto geometries) or isolated NPs, two types of excitations are of interest: (1) the surface plasmon polaritons (SPPs), which are travelling electromagnetic waves along a metal/dielectric interface and (2) localized surface plasmons (LSPs), which are confined to NPs.

Having observed significant changes in the electro-optical properties of PDLCs doped with Au NPs, we had suggested that the physical mechanism behind these results involved surface plasmon excitations at metal (Au)/dielectric (LC) interfaces [1]. In order

to investigate how effectively SPs can be excited in nematic LC (E44) doped with 14 nm diameter Au NPs, we have carried out ATR measurements on the same material. Six different samples were prepared on glass slides containing mixtures of LC and dispersions of Au NPs (10^{-10} mol/l dispersion of NPs in water). Two sets of measurements were made: in the first set of measurements, the high-index prism had no gold coating on its base and in the second set of measurements, the base of the high-index prism was coated with 40 nm Au thin film. The first set of measurements utilized four samples: sample-1 contained only the LC next to the prism base, sample-2 contained a mixture of LC and 35 wt. % dispersion of Au NPs, sample-3 contained LC and 50 wt. % dispersion of Au NPs, and sample-4 contained only the dispersion of the Au NPs. We used two samples for the second set of measurements: sample-5 containing the prism/40 nm Au/air and sample-6 had only LC (similar to sample-1, but in sample-6 the LC was in contact with 40 nm thin Au film on the base of the prism). Our optical spectroscopy system is shown schematically in figure 4.1.

For reflectivity measurements, each one of the samples described above was placed under the high-index prism and mounted on (θ, 2θ) goniometer. As stated above, in the first set of measurements, the high-index prism had no gold coating on its base. Here, the idea was to simulate conditions, which might have existed in the case of our previous experiments on PDLCs containing Au NPs in which case no well-defined Au film/LC interfaces were created. In the second set of measurements, one of the faces of the high-index prism (base) was coated with 40 nm Au thin film, which creates well-defined Au/LC interfaces in the adjoining LC sample. For both sets of measurements, the reflectivity for

the s- and p-polarized incident 632-nm laser was measured as functions of incident angle using silicon detectors and LABVIEW software. Resulting confocal microscopy images of selective sample (sample-2) are shown in chapter 4.

The reflectivity data for both s- and p-polarized incident laser beams, obtained in the first set of measurements, are shown in Figure 5.2. For both polarizations, the reflectivity rises with increasing angle and reaches a plateau at the critical angle for total reflection (θ_c). Through the use of the Snell's law, the θ_c values observed in the cases of the LC and Au NPs dispersion provide dielectric constants of 2.32 for the nematic phase of the LC and 1.81 for the Au NPs dispersion. Thus, obtained values of the dielectric

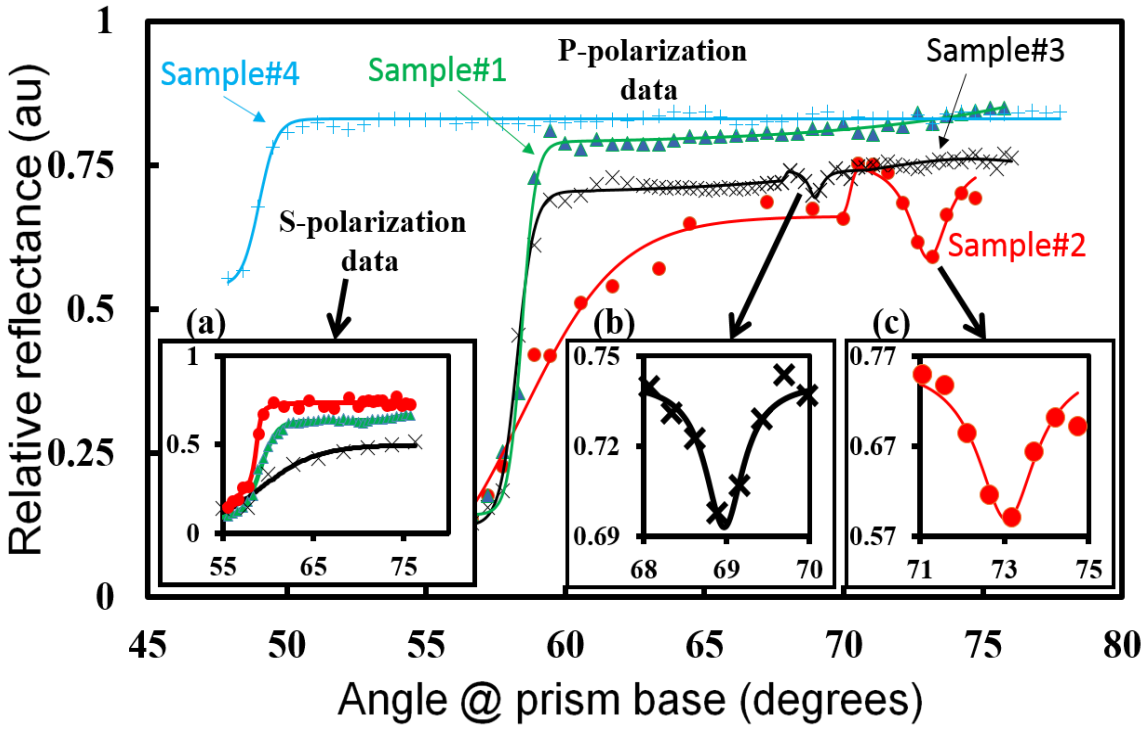

Figure 5.2 Relative reflectance vs incidence angle for sample-1-4, for p-polarized incident laser beam. Inset (a) shows data for s-polarized beam, (b) and (c) shows ATR in sample-3 and sample 2 on magnified scales. The solid curves are drawn to aid the eyes [2].

constants of the nematic phase of the LC (E44) and water are in excellent agreement with the known values of 2.309 [58] for LC and 1.78 for water near optical frequencies [59].

For an s-polarized incident beam (inset-a in Figure 5.2), the reflected intensity approaches a plateau and shows no evidence for ATR for LC, as well as for the other two samples, which contain Au NPs. This is what is expected from the view point of the wave vector matching condition for SPPs. The situation is, however, different when p-polarized laser is incident on samples containing Au NPs (sample-2 and sample-3). In these latter samples, we observe loss in reflected intensity at θ_{ATR} ($\theta > \theta_c$). The reflected intensity shows a characteristic upward shoulder at ~70.5^o (sample-2) and ~68^o (sample-3) followed by loss in reflected intensity of ~23% at θ_{ATR} = 73.6^o in sample-2 and ~7% at θ_{ATR} = 69^o in sample-3.

We have simulated the reflectivity vs angle data using the well-known Fresnel equations for model systems consisting of high-index prism/40-nm-Au film/sample, where the sample is LC + 35 wt. % Au NPs dispersion in one case, and LC + 50 wt.% Au NPs dispersions in the second case. The simulations are carried out in MATLAB environment by using the transfer matrix method (TMM) for multilayered thin film system, as described in our recent publication [6]. As shown in figure 5.3, our measured values of θ_{ATR} for samples containing 35 wt. % and 50 wt. % Au NPs dispersions are in agreement with the results of these simulations, when dielectric constants of the sample media in contact with the prism surface are considered as 2.3 and 2.2. The angle of reflectivity minima (θ_{ATR}) of the simulated curves for both the samples (35 wt.% and 50 wt.% Au-NPs dispersion) perfectly coincides with the observed experimental values of the same sample shown in

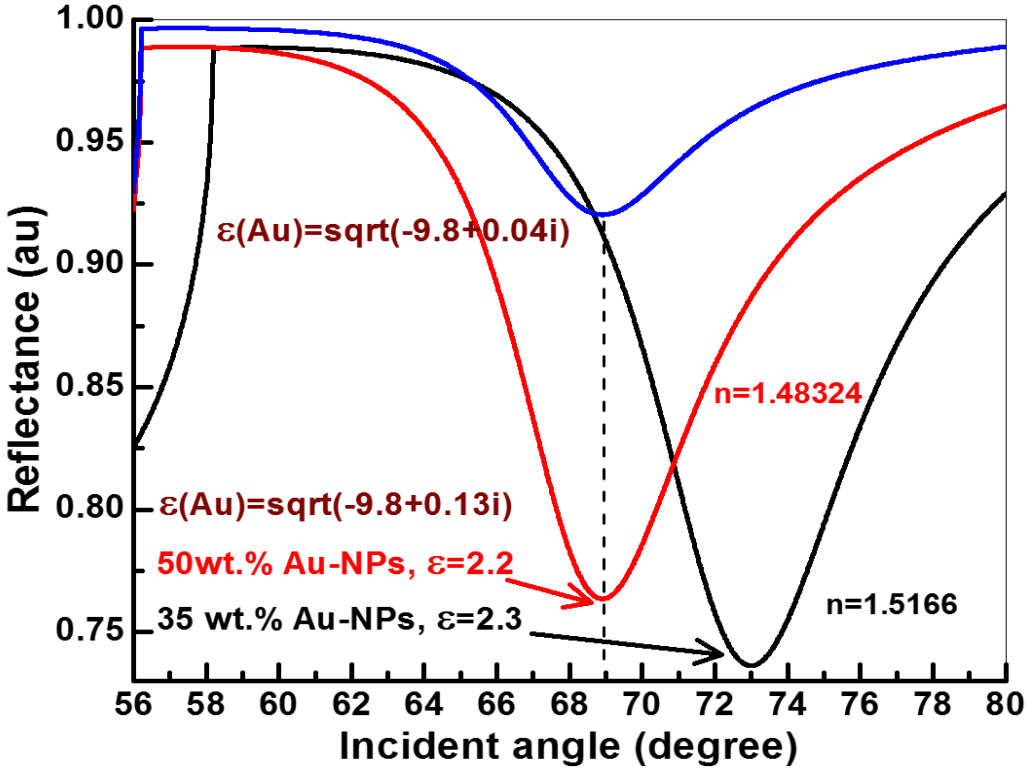

Figure 5.3 MATLAB simulations for high index prism/40-nm Au film/LC+AuNPs dispersion samples. The dielectric constant of two different samples used are; ε = 2.3 for 35 wt.% Au-NPs dispersion, and ε = 2.2 for 50 wt.% Au-NPs dispersion.

figure 5.2, if the 40nm thick Au film coated on the prism base have a dielectric constant, ε_{Au} = -9.8 + *i*0.13. In order for the simulations of sample-3 (LC+50 wt.% Au-NPs dispersion) to observe an identical magnitude of % loss in reflectivity as in our experimental case, the dielectric constant of Au film used in simulation needs to be modified to ε_{Au} = -9.8 + i0.04.

Thus, figure 5.2 shows that (i) no ATR occurs when s-polarized beam is used, (ii) ATR occurs at certain angle (θ_{ATR}) when p-polarized beam is used, and (iii) θ_{ATR} values change with the dielectric constant of the sample. This set of results supports SPPs in

sample-2 and sample-3, even though the prism had not been coated with a thin Au film. Supporting arguments, taken from other published works, are discussed later.

In order to better understand the observed loss in totally reflected intensity in sample-2 and sample-3, we have carried out additional experiments using Kretschmann geometry for which one of the faces of the prism was coated with 40 nm Au film. Once again, reflectivity measurements were carried out for both s- and p-polarized 632 nm incident laser on two samples: sample-5 (prism/40-nm Au/air) and sample-6 (LC only). The resulting data are shown in Figure 5.4.

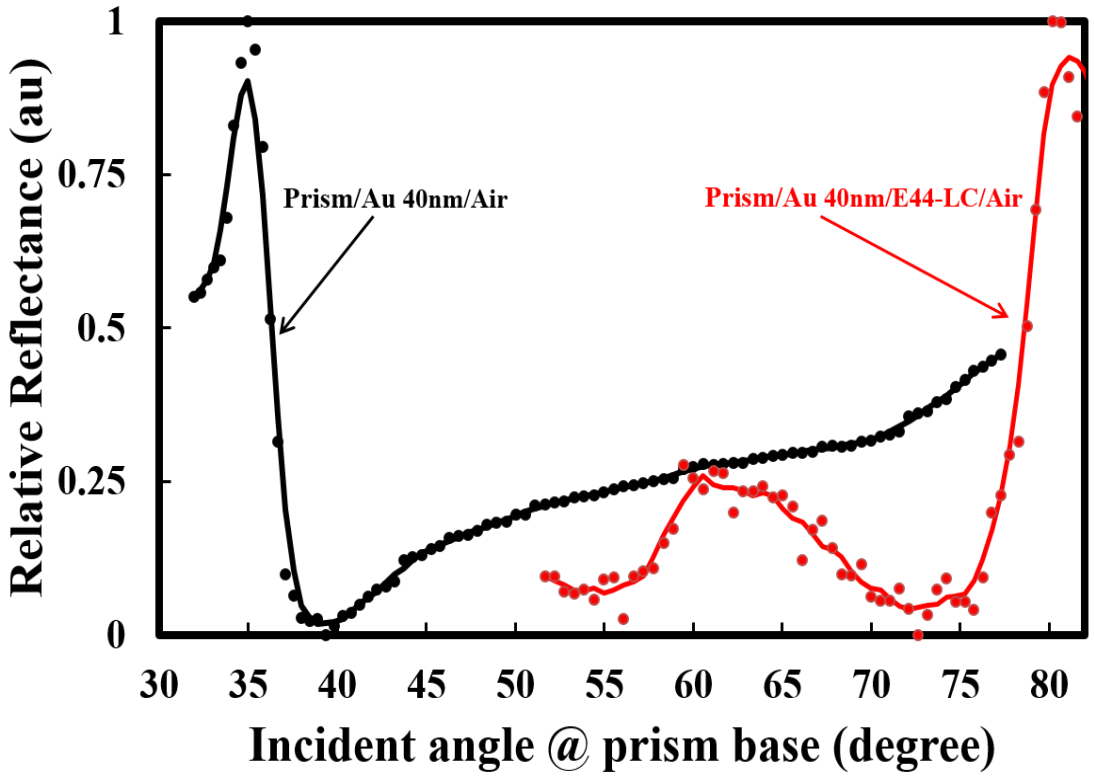

Figure 5.4 Reletive reflectance vs incident angle for sample-5 (prism/40-nm Au/air), sample-6 (LC only). The solid curves are drawn to aid the eyes.

First of all in the case of the prism/40 nm Au/air (sample-5), the reflectivity data for the p-polarized laser show total internal reflection at $\theta_c = 35^o$ followed by dramatic loss

in reflected intensity at $\theta_{ATR} \sim 39^o$. These features are in agreement with simulations made using $\varepsilon_{prism} = 3.1852$, $\varepsilon_{Au} = -9.8 + i0.73$, and 40nm thickness of the Au film coating on the prism. As it is well-known, the ATR at 39^o is a signature of the SPPs travelling along Au/air interface [11]. In the case of sample-6 (LC only), once again we observe total internal reflection at $\theta_c = 59^o$ followed by loss in total reflection at $\theta_{ATR} \sim 73^o$. The measured critical angle $\theta_c = 59^o$ is in excellent agreement with 58.6^o calculated using 3.1852 and 2.3224 for the dielectric constants of the prism and LC, respectively. Remarkably, identical θ_{ATR} values are observed for sample-2 (LC + 35 wt. % NPs dispersion shown in Figure 5.2, for which the prism had not been coated with thin Au film) and sample-6 (shown in Figure 5.4, for which the prism had been coated with 40nm thin Au film). Since the ATR in sample-6 (having well-defined Au/LC interface) unambiguously identifies SPPs along the Au/LC interface, the loss of reflectivity observed at the same angle in sample-2 suggests that SPPs are also excited along Au NPs/LC interfaces in sample-2.

5.1.3 Discussions

It is highly possible that Au NPs form LC-induced aligned structures within the decay length of the evanescent waves (≈50 nm) from the base of the prism. Sufficient evidence exists in support of such an alignment. For example, linear self-assembly of Au NPs within LC defect arrays has been demonstrated [59]. In this work, Au NPs, as small as 5 nm, are observed being trapped in smectic defects in liquid crystal 8CB (4-n-octyl-4'-cyanobiphenyl), where they align in straight parallel chains separated by 1.5 nm to μm. A second independent study on a colloidal dispersion of CdS quantum dots in nematic LC 4-

cyano-4'-pentylbiphenyl (5CB) has shown that the nematic phase of the LC imposes self-assembly of quantum dots to form one dimensional arrays [60]. In another study, 10^6-enhancement in the conductivity of a discotic LC (HAT6) doped with only 1wt. % Au NPs has been attributed to the formation of chains of gold NPs. In the light of these results, it appears very likely that NPs in sample-2 and sample-3 form LC-assisted aligned structures, which facilitate surface plasmon excitations along NPs-LC interfaces in the proximity of the prism base. How such aligned nanostructures change with the nature of the constituent materials (e.g., type of the LC and NPs), trapping of NPs in liquid crystal defects, as well as the influence of externally applied electric fields on the LC alignments, remain to be investigated.

5.2 Liquid crystal assisted tunable surface plasmon device

A highly sensitive surface plasmon based sensor is developed for monitoring changes in the dielectric environment at metal/dielectric interfaces. It consists of high-index prism/30–40 nm gold/nematic liquid crystal (E44)/indium-tin-oxide/glass structure, which enables measurements of surface plasmon resonance (SPR) curves by using the Kretschmann configuration. The baseline sensitivity of the device to changes in the refractive index is evaluated by using Au/air, Au/water, and Au/nematic liquid crystal (E44); the measured baseline sensitivity is in excellent agreement with theoretically predicted optimal sensitivity. The sensitivity of the device to electric field induced changes in the refractive index of the material at the interface, however, is 28-times higher than previously known value for a similar sensor. Effects related to the periodic alignment of

the liquid crystal on gold surface and surface plasmon mediated diffraction are investigated.

5.2.1 Sensitivity of the device to changes in dielectric environment at three interfaces

To begin with, we evaluate the sensitivity of the device to changes in the dielectric environment at interfaces of interest. Obviously, there are several different interfaces within the structures used in this work: (1) the gold/air interface in prism/Au-film/SiO2 structure (the amount of the insulating SiO_2 beads used is so small that the interface in this particular case is essentially defined by air), (2) the gold/water interface in prism/Au-film/Au-NPs-dispersion in H_2O structure and (3) the gold/LC interface in prism/Au-film/LC structure. We have carried out ATR measurements for all three structures and the results are shown in figure 5.5. Each one of these curves contains information on the occurrence of total internal reflection from an interface and loss in the intensity of the totally reflected light at some specific resonance angle due to the excitation of the surface plasmon polaritons. Incidentally, this occurs only in the case of p-polarized incident laser beam. We observe no loss in totally reflected intensity in the case of s-polarized incident beam [2,43]. The main features of these data can be described qualitatively by: (i) rise in reflectivity up to a certain angle (θ_c), at which total internal reflection occurs with θ_c = sin−1($n_{\text{material}}/n_{\text{prism}}$), (ii) maximum loss in reflectivity (ATR) at certain resonance angle (θ_{SPR}), which depends on the type of the material at the interface and (iii) the reflectivity recovers from the loss at angles higher than θ_{SPR}. Approximate values for the interface parameters can be obtained from the data of figure 5.8 without any elaborate analysis. For example, the values of the critical angles seen in these curves (θ_c = 35º, 50º, and 59º)

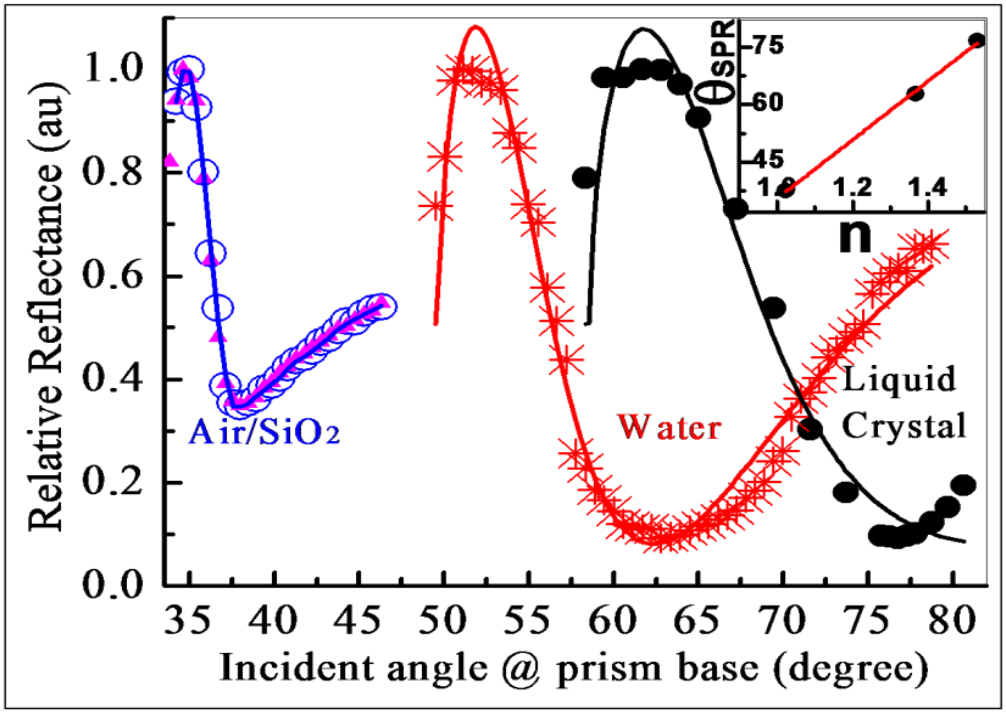

Figure 5.5 The reflectivity vs incident angle for a p-polarized 632 nm laser beam atthe base of the prism used in the Kretschmann configuration. Reflectivity data areshown for three interfaces: (i) prism/Au-film/SiO_2, (ii) prism/Au-film/water, and (iii) prism/Au-film/LC interfaces. The solid curves represent results of the nonlinear squares fit of Eqs. (1) and (2) discussed in the text. The inset shows linear dependence of the resonance angle θ_{SPR} vs. refractive index of the materials used.

provide values for the refractive index of the material at the inter-face by using $\theta_c = \sin^{-1}(n_{material}/n_{prism})$; n_{air} = 1.023, n_{water} = 1.367, and n_{E44} = 1.525. These values are in excellent agreement with known refractive indices of air, water, and nematic phase of the liquid crystal E44 [61]. The slight differences in the values of the refractive indices of air and water from the established respective values of the refractive indices of these two materials (1.0 and 1.33, respectively) are due to the facts that the ambient air was humid and the water solution used had 10^{-10} mol/l Au NPs in it. Additionally, the resonance curves provide resonance angles θ_{SPR} = 38°, 62.5° and 76° for the gold/air, gold/water and gold/LC interfaces, respectively. The overall performance of the sensor can be characterized by

several different parameters; (a) sensitivity $S = \delta\theta_{SPR}/\delta n$, which is a measure of the change observed in the value of the resonance angle θ_{SPR} when the refractive index of the medium changes by δn, (b) a figure-of-merit parameter FOM = S/FWHM, where FWHM is the full-width at half-maximum of the resonance curve, and (c) resolution, which scales with the figure-of-merit value, i.e., higher FOM corresponds to higher resolution. As seen in the inset in figure 5.5, the resonance angle θ_{SPR} changes almost linearly with refractive index of the medium with sensitivity $S = \delta\theta_{SPR}/\delta n$ = (77 ± 3) degrees RIU^{-1} (here RIU means "refractive index unit"). These performance parameters of the sensor may change depending upon the dielectric environment at the metal/dielectric interface, nature of the metal coating (e.g., Au vs Ag and thickness of the coating), and wavelength of the incident radiation. As stated above, in our experiments we used high-index prism of refractive index = 1.7847 @ 632 nm, 30 nm thick gold film and λ = 632.8 nm incident radiation. It is useful to compare the performance characteristics of our sensor with those of other com-parable sensors. In this context, Roh et al. have presented calculated optimal characteristics of Au, as well as Ag layer sensors [62]. For SF10 prism, 55 nm gold film, and λ = 633 nm, these authors report $S = 100^{o}$ RIU^{-1} and FOM = 20.8. The performance parameters of our Kretschmann configuration sensor, $S = 75^{o}$ RIU^{-1} and FOM = 35 are in excellent agreement with the optimal characteristics calculated for a similar sensor. In fact, because of significantly narrower resonance curve observed in our work, the resolution of our sensor is much higher than the value calculated by Roh et al. for a similar sensor [62]. Figure 5.5 also compares two resonance curves measured for zero and about 5×10^5 V/m applied across gold/air interface in Au/SiO_2 structure. Within the statistical uncertainties, these two

sets of data are essentially indistinguishable from one another. As expected, this observation confirms that application of about 5×10^5 V/m across the Au/SiO_2 interface does not produce any undesirable effects on the ATR curves. All of these are the base-line results and they will be helpful in understanding other sets of data presented below in this manuscript.

5.2.2 Simulations for the sensitivity of device

In order to obtain more accurate quantitative information on the interface parameters, we have analyzed the ATR curves of figure 5.5 by using the Fresnel equations in a nonlinear least-squares subroutine [63]. In this model, the reflectivity from a thin metal film can be expressed by,

$$R = \left| \left[\frac{\exp(-i2\phi_{21} - \exp(-i2\phi_{01})\exp(-2\alpha_1 d)}{1 + \exp(-i2(\phi_{21} + \phi_{01}))\exp(-2\alpha_1 d)} \right] \right|^2, \tag{5.1}$$

$$\text{where } \phi_{01} = \tan^{-1}\left(\frac{\varepsilon_0 \alpha_1}{\varepsilon_1 \kappa_0}\right), \quad \phi_{21} = \tan^{-1}\left(\frac{\varepsilon_2 \alpha_1}{\varepsilon_1 \kappa_2}\right), \quad \kappa_j = \sqrt{\left(k_0^{\,2}\varepsilon_j - \beta^2\right)},\ j = 0, 2,$$

$$\alpha_1 = \sqrt{\beta^2 - k_0^{\,2}\varepsilon_1}\ \&, \quad \beta = k_0\sqrt{\varepsilon_2}\sin(\theta) \tag{5.2}$$

In these equations, subscripts 0, 1, and 2 identify parameters characterizing LC, Au, and prism, respectively. The kjs are the wave vector components perpendicular to the interface in medium identified with j, α_1 is the attenuated coefficient of the field in the metal, β is the component of the incident wave vector parallel to the interface, and $\kappa_o = 2\pi/\lambda$ is the wave number corresponding to the wavelength of the laser λ in free space. The complex optical constant of the metal film $\varepsilon_{Au}(\omega)$ is represented by a complex and frequency dependent dielectric constant, $\varepsilon_{Au}(\omega) = \varepsilon_{real}(\omega) + i\varepsilon_{imag}(\omega)$. By using Eqs. (5.1) and (5.2), the analysis

of the data of figure 5.5 provides values for the dielectric constants of both materials at the interface (H_2O at one interface and E44 at the other interface) and film thickness. The solid curves in figure 5.5 correspond to ε_{Au} (λ = 630 nm) = (−7.8 ± 0.8) + i(1.25 ± 0.74), ε_{H2O} = 1.852 ± 0.005, ε_{LC} = 2.32 ± 0.02, and film thickness = 28.9 ± 1.0 nm. For the sake of comparisons: (1) the dielectric constant of gold @ λ = 630 nm has been observed to vary from −10.8 + i1.47 to −12.8 + i1.36, the dielectric constant of H_2O near optical frequencies is known to be approximately 1.78 [59], and the dielectric constant of the liquid-crystal is about 2.309 [58]. From the quartz crystal thickness monitor and AFM measurements, the thickness of the gold film was estimated to be in 30–40 nm range. Thus the least squares fits made to the data of figure 5.8 by using Eqs. (5.1) and (5.2) provide precise values for the dielectric constants and film thickness, which are in good agreement with other published results referenced above.

5.2.3 Sensitivity to electric field induced changes in the dielectric environment at interface

Following analyses of the above described baseline data and in order to further evaluate the sensitivity of our device, we have carried out ATR measurements as functions of 1 kHz electric fields. The resulting surface plasmon polariton resonance data are shown in figure 5.6. It is worth pointing out that ATR curves have been measured for one or two values of dc fields and these previous measurements have demonstrated the sensitivity of the technique to dc fields. The present work, however, provides the first set of detailed ATR measurements spanning a much wider range of ac fields that has yielded quantitative information on the sensitivity of the technique to changes in the dielectric environment at interfaces. Furthermore, the detailed data shown in figure 5.6 establish for the first time

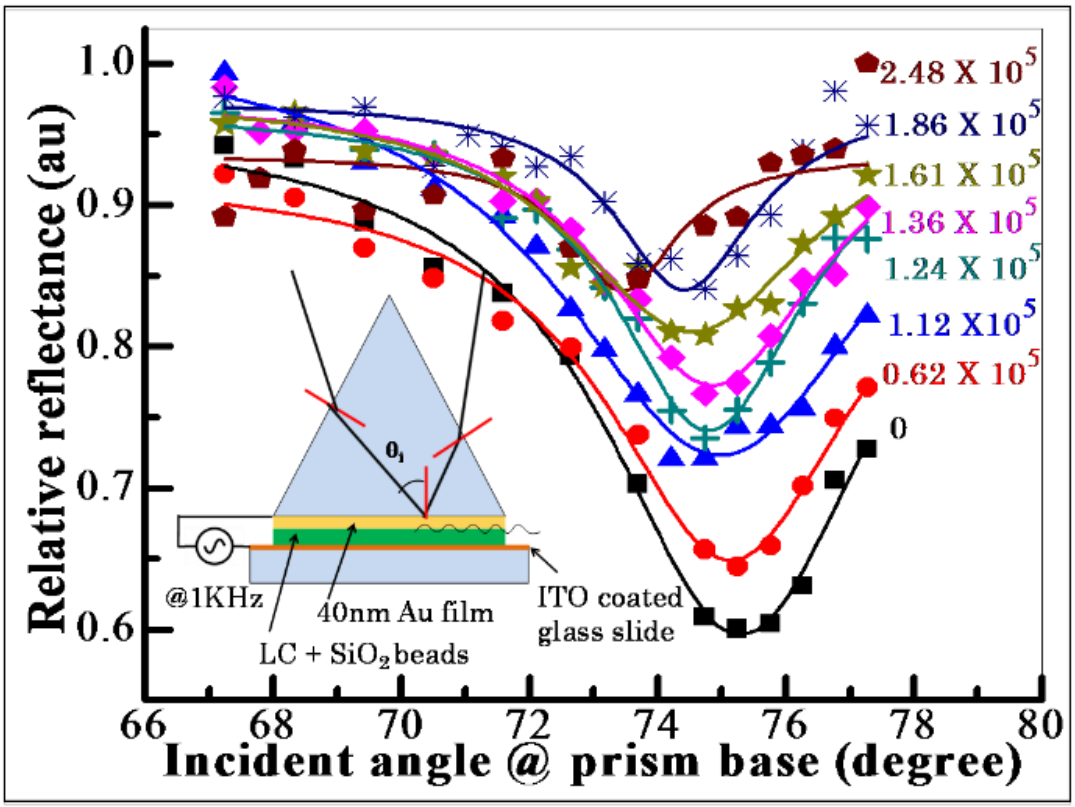

Figure 5.6. The reflectivity vs incident angle for a p-polarized 632 nm laser beam at several values of externally applied electric fields (1 kHz). The inset shows schematic layout of sensor structure and solid curves represent smooth fits to aid eyes.

how applied ac fields influence overall nature of the resonance (i.e., relative intensity, FWHM, any field dependent asymmetry in shape). The main features of the electric field dependent resonance data of figure 5.6 can be summarized as follows: (1) the reflectivity suffers dramatic loss at certain field dependent value of the surface plasmon polariton resonance angle (θ_{SPR}), (2) θ_{SPR} decreases with increasing electric field, (3) the magnitude of the loss in reflectivity decreases at higher fields, and (4) the resonance curves become narrower at higher fields. Once again, by fitting the data of figure 5.6 to Eqs. (5.1) and (5.2), we obtain: (1) $\varepsilon_{Au} = (-9.25 \pm 0.20) + i(1.75 \pm 0.01)$, which is in good agreement with published results for gold at $\lambda = 632$ nm [34,64] and (2) an average value of (39.5 ± 1.0)

nm for the thickness of the gold film, which too is in good agreement with 30–40 nm indicated by the quartz crystal oscillator used during sputter-coating of the film.

The electric field dependencies of the resonance angle and reflectivity at resonance are shown in figure 5.7. The magnitude of the loss in reflectivity changes from about 36% at zero field to about 10% at 2.5×10^5 V/m and θ_{SPR} shifts non-linearly from about 75.2° at zero fields to 73.8° at 2.5×10^5 V/m. It is remarkable that the sensitivity of our device, characterized by the electric field induced shift in the resonance angle ($\Delta\theta_{SPR}$ = 1.4°; $\Delta\theta_{SPR}/\Delta E = 5.6 \times 10^{-6}$ (degrees/(V/m))), is 28-times higher than the $\Delta\theta_{SPR}/\Delta E$ value published elsewhere for the only other known device [65]. Because of narrowing of the resonance curves at higher fields, the resolution of the device improves with increasing

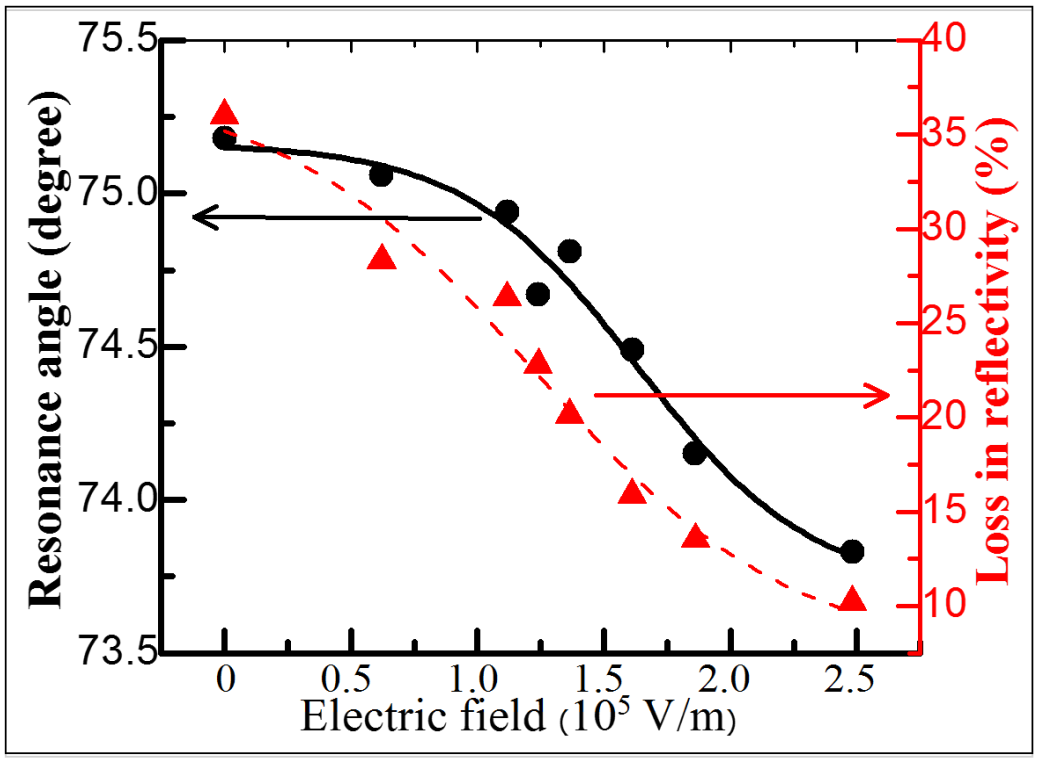

Figure 5.7. The resonance angle and loss in reflectivity vs electrical field data obtained from nonlinear least squares fits of eqs (2)-(3) to the data of Fig-5, which are discussed in the text. The solid curves represent smoothed fits to aid the eyes.

fields. Of course, the sensitivity is expected to depend on the chemical composition of the LC and the surface anchoring forces. It is well known that the surface anchoring forces acting on LC molecules can limit the orientation of the LC molecules, particularly adjacent to the electrodes in a device, and thereby influence device performance [65-68]. The extremely high sensitivity of our device may be useful in the design of certain types of surface plasmon polariton and LC based opto-electronic switches that respond to loss in reflectivity or change in the SPPs resonance angle.

5.2.4 Interpretation of the electric field induced changes in the refractive index

Figure 5.8 shows the electric field dependence of the LC refractive index n(E) obtained from nonlinear least squares fits of Eqs. (5.1) and (5.2) to the data of figure 5.7. The refractive index decreases from approximately 1.525 @ zero field to 1.485 @ 2.5×10^5 V/m. It is well known that the refractive index of an electro-optic medium can undergo significant changes under the influence of externally applied electric fields [69,70]. In the case of non-centro-symmetric materials (such as $LiNbO_3$, CdTe, and $NH_4H_2PO_4$), the electric field dependence is described by the Pockels effect, whereby $n(E) = n_0 - (1/2)\tau n_0^3 E$. Here n_0 is the refractive index at zero fields and τ is the Pockels coefficient with typical values ranging from 10^{-12} to 10^{-10} m/V. This effect has been observed in some photopolymers with smectic-C*-like order derived from low molecular weight ferroelectric liquid crystals [71]. These measurements have provided values on the order of 10^{-12} m/V for the Pockels coefficient. However, in centro-symmetric materials (such as liquids and glasses), the electric field dependence of the refractive index is nonlinear and described by the Kerr effect, according to which, $n(E) = n_0 - (1/2)\,\kappa n_0^3 E^2$, where κ is the

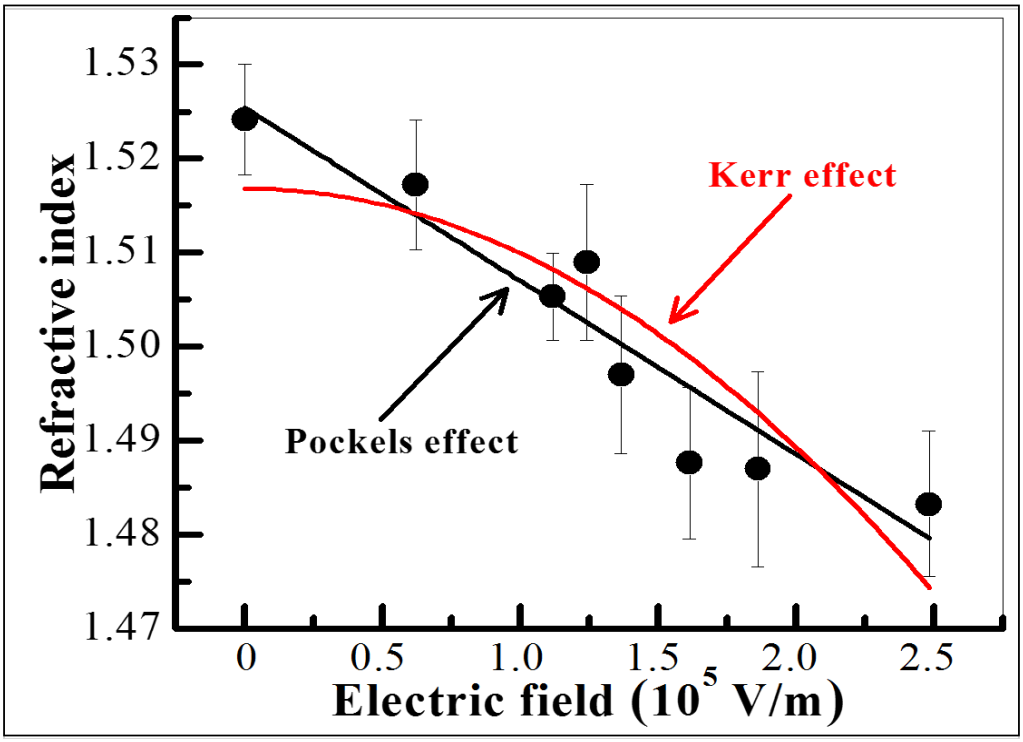

Figure 5.8 The refractive index vs applied electric field obtained from nonlinear least squares fits of eqs (2)-(3) to the data of Fig-5. The solid curves represent nonlinear least squares fits made by using linear (the Pockels effect) and quadratic (the Kerr effect) field dependencies discussed in the text.

Kerr coefficient with typical values ranging from 10^{-22} to 10^{-19} m^2/V^2 for liquids. The Kerr effect has been observed in polymer-stabilized isotropic liquid crystal (E31LV) and polymer-stabilized blue-phase liquid crystal (PS-BPLC) and values on the order of 10^{-16} m^2/V^2 have been reported for the Kerr coefficients in these materials [72,73]. Guided by these results, we have analyzed the electric field dependence of the refractive index by using linear, as well as quadratic field dependencies. The results of the nonlinear least squares fit are represented by $n(E) = (1.5254 \pm 0.0046) - (1.85 \pm 0.35) \times 10^{-7}E$ and $n(E) = (1.5168 \pm 0.0035) - (7.0 \pm 1.4) \times 10^{-13}E^2$, and they are included in figure 5.8. The refractive index of the liquid crystal (E44) for λ = 632 nm at zero field and room temperature is in excellent agreement with n_o = 1.5195 and 1.5245 published elsewhere [2,58]. The solid

curves in figure 5.11 correspond to the Pockels coefficient $\tau = 1.85 \times 10^{-7}$ m/V and Kerr coefficient $\kappa = 7 \times 10^{-13}$ m^2/V^2. These are unexpectedly large coefficients and they do not agree with the reported values of the Pockels and Kerr coefficients in related similar materials. As stated above, values on the order of 10^{-12} m/V and 10^{-16} m^2/V^2 have been reported for the Pockels and Kerr coefficients, respectively in polymer-stabilized isotropic liquid crystal (E31LV) and polymer-stabilized blue-phase liquid crystal (PS-BPLC) [71–73]. In order for our results for the Pockels and Kerr coefficients to fall within the ballpark limits of the published coefficients, the actual electric fields within the material would have to be much larger than externally applied electric fields; larger by factors of 10^5 and 60 to match with the published values of the Pockels and Kerr coefficients, respectively. Whereas a factor of 10^5 appears much too high, it is reasonable to suspect that the actual electric fields within the material in our experiments could be higher, by as much as a factor of about 60, than externally applied fields. The examples of the surface enhanced Raman scattering and self-similar systems containing silver nano-spheres provide ample evidence for the plasmon-induced enhancements in the local electric fields [74–77]. For example, whereas local electric field enhancements ≤ 30 are predicted for single Ag nano-sphere, enhancements as large as 103 may be realized by using clusters of Ag nano-spheres [75]. Based on the facts that in the centro-symmetric optical materials, electric field induced changes in the refractive index of the material are often explained by the Kerr effect, it appears plausible that the actual electric field "seen" by the LC sample in our experiments could be higher (by as much as a factor of 60) than applied fields and consequently the

electric field induced changes in the refractive index of the sample are consistent with the Kerr effect.

5.2.5 Stability of sensor

The stability (reproducibility) of the response of the sensor was checked several times during the course of the measurements spanning a period of several months. In one set of the experiments, the response of the sensor to three different interfaces without external electric fields, i.e., metal/air, metal/water, and metal/LC (E44), was examined weeks apart. Each time the fluid in contact with the metal surface was changed, the sensor surface was first cleaned with Acetone solution to avoid cross contamination of the fluids. These measurements reproduced resonance curves for each one of the fluids well within the statistical uncertainties of the measurements. In the second set of measurements, the stability of the sensor to provide accurate values of the refractive index of the fluid under externally applied electric fields was examined over a period of three months. The sensor retained its basic characteristics, which are that: (1) the reflectivity suffers dramatic loss at certain field dependent value of the surface plasmon polariton resonance angle, (2) the resonance angle decreases with increasing electric field, (3) the magnitude of the loss in reflectivity decreases at higher values of the field, and (4) the resonance curves become narrower at higher fields. Based on these observations, we conclude that the sensor is stable and reproduces the refractive index data satisfactorily.

5.2.6 Liquid crystal alignment on gold surface and SPP-assisted formation of diffraction grating

Interactions of liquid-crystalline molecules with metal surfaces are important from the viewpoint of basic surface science, as well as sensor technology to study processes occurring at metal/fluid interfaces. In order to better understand surface-mediated alignment of LC molecules at gold surface of ±5 nm root-mean-square smoothness, we have investigated whether the formation of periodic LC structures, aided by resonant excitation of surface plasmon polaritons at the metal/E44 interface, can be utilized as diffraction gratings. The method adopted for LC grating formulation in this work is extremely simple and different from the traditional methods used to form grating structures in, for example holographic polymer-dispersed liquid crystals (HPDLCs [66-68]). In the latter case, the fabrication of the grating involves precisely controlled protocol using several interrelated steps. For example, (i) a polymer like polyimide or polyvinyl alcohol (PVA) is spin coated and baked over ITO-coated glass substrate, (ii) the baked surface is rubbed uni-directionally with velvet to produce grooves, (iii) certain holographic polymer-dispersed liquid crystal (HPDLC) mixture, consisting of nematic LC, reactive mesogenic monomer and photo-initiator/co-initiators, is spin coated, and (iv) eventual set-up of periodic spatial variation in the refractive index within the material due to light-induced phase separation into polymer-rich and LC-rich channels. The LC droplets in the LC-rich regions are nematically ordered and as a result of the initial surface preparation most of the LC droplet directors are aligned along grooves on the surface. The final result is the holographic recording of a diffraction grating under illumination by coherent laser beams

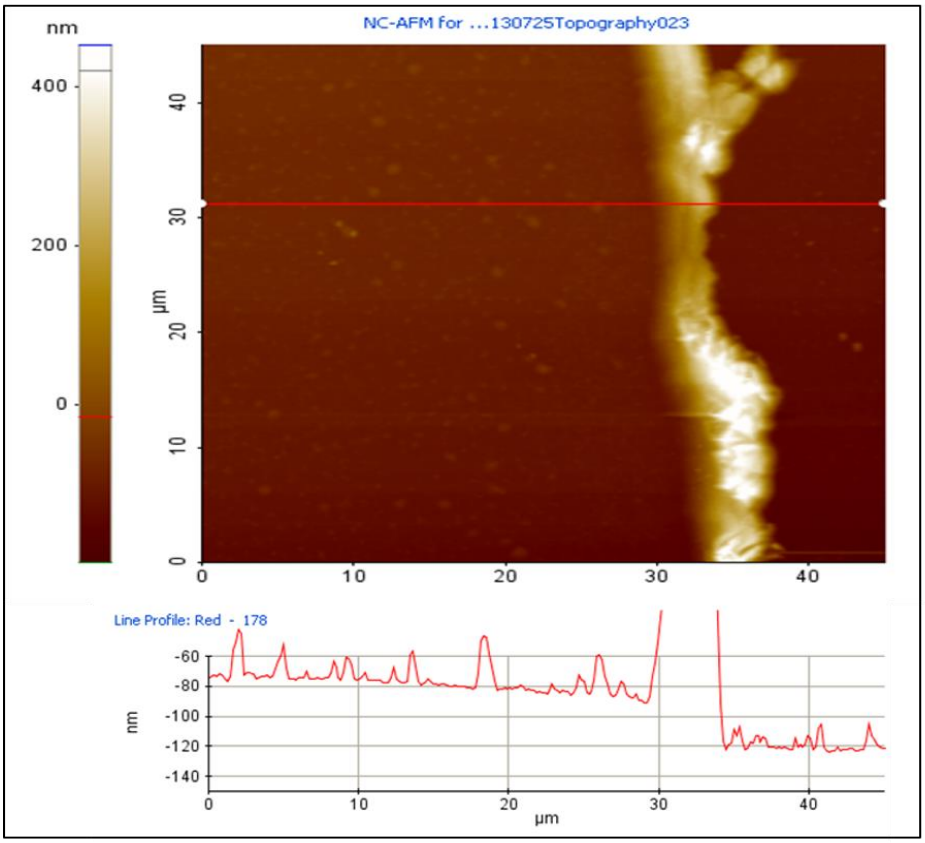

Figure 5.9 AFM scan showing surface topography of the gold film. AFM scan was made along the horizontal line shown. The big blog-looking feature is thickness step at which the gold film thickness changes from 30 nm to zero (substrate surface).

[66-68]. In contrast, and as evidenced by the AFM scans shown in figure 5.9, the surface topography of the gold film used in the present work already contains periodic array of grooves. The as-grown periodic array of micro-fluidic channels on gold surface facilitates preferential alignment of the LC within these channels. This greatly simplifies grating formation. Under this scheme, a three layer structure is formed (Au/LC/ITO), wherein the alignment of the LC directors in direct contact with the gold and ITO surfaces is controlled by the topography of each one of these surfaces due to relatively strong anchoring of the LC molecules with the underlying surface. The LC molecules, which are sufficiently far

from the gold and ITO surfaces and inside microfluidic grooves, are aligned preferentially along the axes of the grooves. This creates a well-aligned LC structure that we find to be very resilient to damage under normal operating conditions. Figure 5.10 shows typical structure with an average periodicity of approximately 100 μm; the dark regions are rich in nematic LC droplets and the bright regions are void spaces in between LC channels. We have examined the diffraction patterns formed by the grating structure by using s- and p-polarized 632 nm He–Ne laser beams in the Kretschmann configuration SPPs system. For incident angles $\theta \geq \theta_c$, the polarized laser beam undergoes total internal reflection at the gold/LC interface at the base of the high-index prism. In the high-index prism/30 nm gold/LC/ITO structure, the incident laser beam interacts with three different interfaces; prism/Au, Au/LC and LC/ITO interfaces. Since the thickness of Au film (30 nm) is an

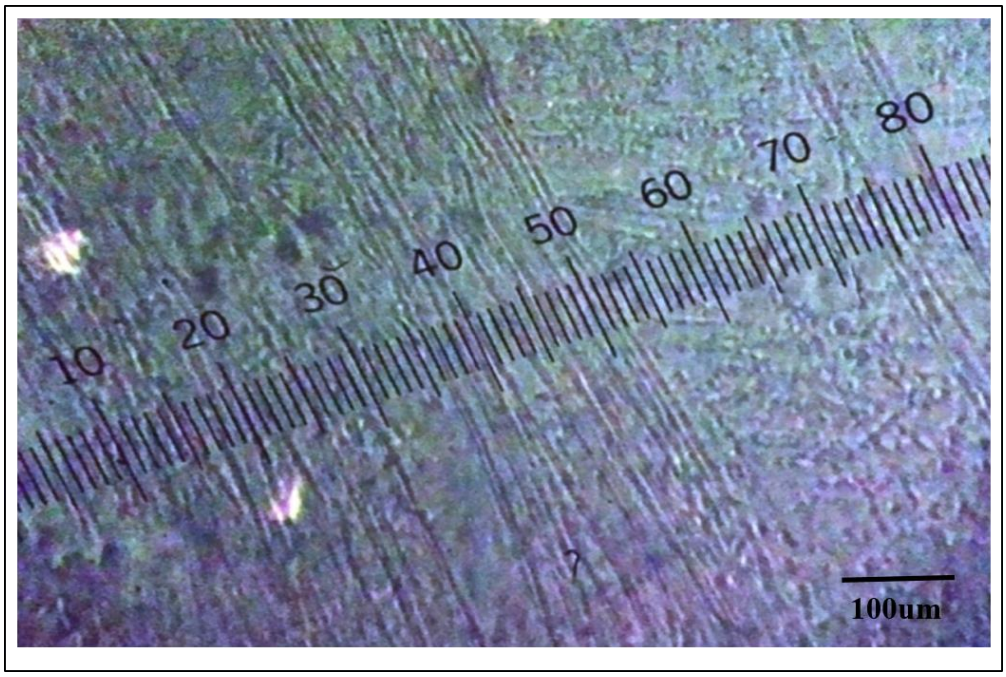

Figure 5.10 High resolution optical image of typical periodic structure of the gold surface with periodicity in the range 10 μm.

order of magnitude smaller than the wavelength of the incident laser (λ_{air} = 633 nm, λ_{prism} = 355 nm), and the refractive indices of the LC and ITO-coated glass are almost the same, the total internal reflection of the laser beam occurs only at the prism/gold interface. Therefore, any diffraction pattern will reflect the periodic LC alignment on the gold surface only. For angles $\theta < \theta_c$, the incident beam passes through the multilayer structure and its transmission is observed at the backside of the high-index prism/gold/LC/ITO-coated glass assembly. A representative diffraction patterns observed with only p-polarized incident beam (figure 5.11) shows the characteristic m = 0, 1, 2 interference spots. We have studied the diffraction patterns as functions of the polarization of the incident laser beam and observe that the diffraction occurs only for p-polarized laser for incident angles near the

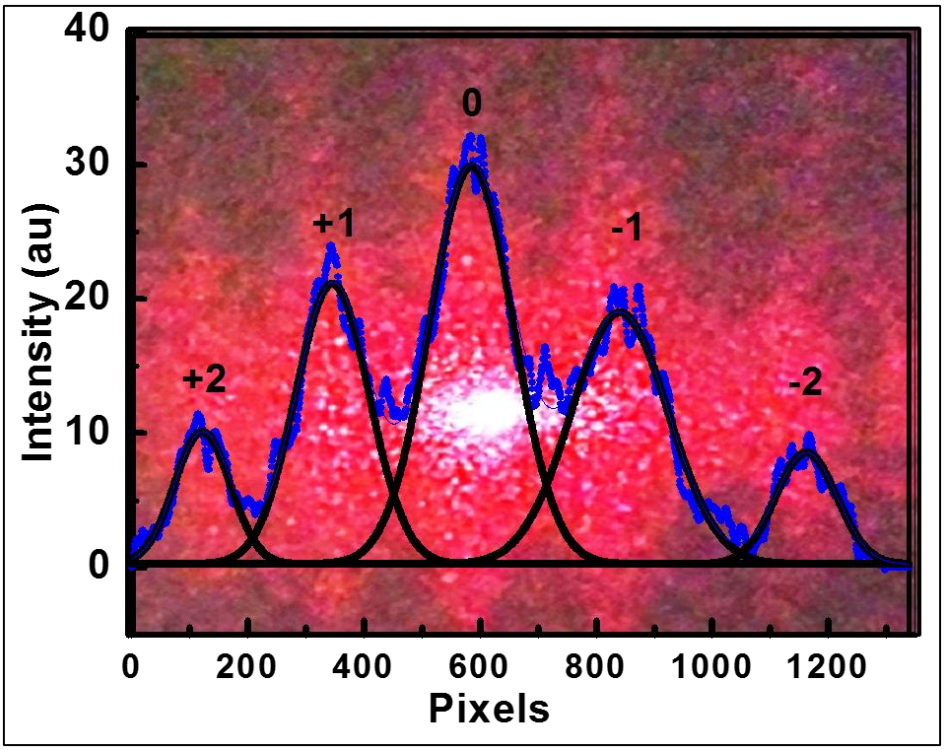

Figure 5.11 Diffraction image recorded at fixed angle in the Kretschmann configuration. The results obtained from the J-Image software analysis of the diffraction image are shown by the continuous curve, which clearly shows the relative intensity distributed among different orders (i.e., zeroth, 1st, and 2nd order peaks).

surface plasmon polariton resonance angle, i.e., for $\theta = \theta_{SPR}$. No diffraction pattern is observed when an s-polarized beam is used. The polarization dependence of the diffraction and its occurrence only at $\theta = \theta_{SPR}$ are extremely important results because they assure the role of the surface plasmon polaritons in diffraction; i.e., diffraction is SPPs mediated. The diffraction images collected at a fixed angle (= resonance angle θ_{SPR}) were captured and analyzed by using the National Institutes of Health Image-J software. This analysis provides results for the periodicity ($\Lambda = 5\mu m$) of the grating structure, which is in excellent agreement with an average value of 4μm obtained from the Fourier analysis of the surface topography AFM measurements. We have also observed that the diffraction pattern disappears when an ac field $\geq 2.5 \times 10^5$ V/m is applied across the device. Upon removal of this field, the diffraction pattern reappears in a reversible manner. These preliminary data clearly show that nematic LC molecules can be aligned in periodic structures by gold surface topography and the coupling between the surface plasmon polaritons excited at the gold/LC interface and totally reflected light can lead to diffraction effects. We are further investigating electric field dependence of the diffraction patterns and additional results will be presented elsewhere.

5.3 High performance surface plasmon sensors

Through computer simulations and surface plasmon resonance (SPR) measurements, we establish optimum parameters for the design and fabrication of SPR sensors of high sensitivity, resolution, stability, and long decay-length evanescent fields.

We present experimental SPR data in supplement of the simulations carried out for variety of sensors fabricated by using bimetal (Ag/Au) and multilayer waveguide-coupled Ag/Si_3N_4/Au structures. The simulations were carried out by using the transfer matrix method in MATLAB environment, as elaborated in section 3. Results are presented as functions of the thickness of the metal (Ag or Au) and the waveguide dielectric used in Ag/Si_3N_4/Au structures. Excellent agreement is observed between the simulations and experiments. For optimized thickness of the Si_3N_4 waveguide (150 nm), the sensor exhibits very high sensitivity to changes in the refractive index of analytes, $S_n \approx 52^0 / RIU$, extremely high resolution $\left(FWHM \leq 0.28^0\right)$, and long penetration depth of evanescent fields $\left(\delta \geq 305\,\text{nm}\right)$ [6].

5.3.1 Single metal (Au and Ag) sensors

Figure 5.12 shows experimental SPR data measured for single metal Au and Ag film sensors, *viz*., sample-1: Quartz/29 nm Au and sample-2: Quartz/40 nm Ag. The Kretschmann configuration optical system described in section 4.1 was used for the optical measurements. The thickness of each metal film deposited (Ag = 40 nm, Au = 29 nm) is almost the same as that used in the case of the bimetallic (Ag{35}/Au{28}), and bimetallic-waveguide coupled sensor (Ag{35 nm}/Si_3N_4{150 nm}/Au{28 nm}). The TMM simulations are represented by the continuous solid curves. The degree to which the TMM simulations and the experimental data agree in figure 5.12 is impressive, particularly in the case of the silver film sensor. In the case of the gold film sensor, however, the agreement between the simulations and the experimental data is not as good as it is in the case of the

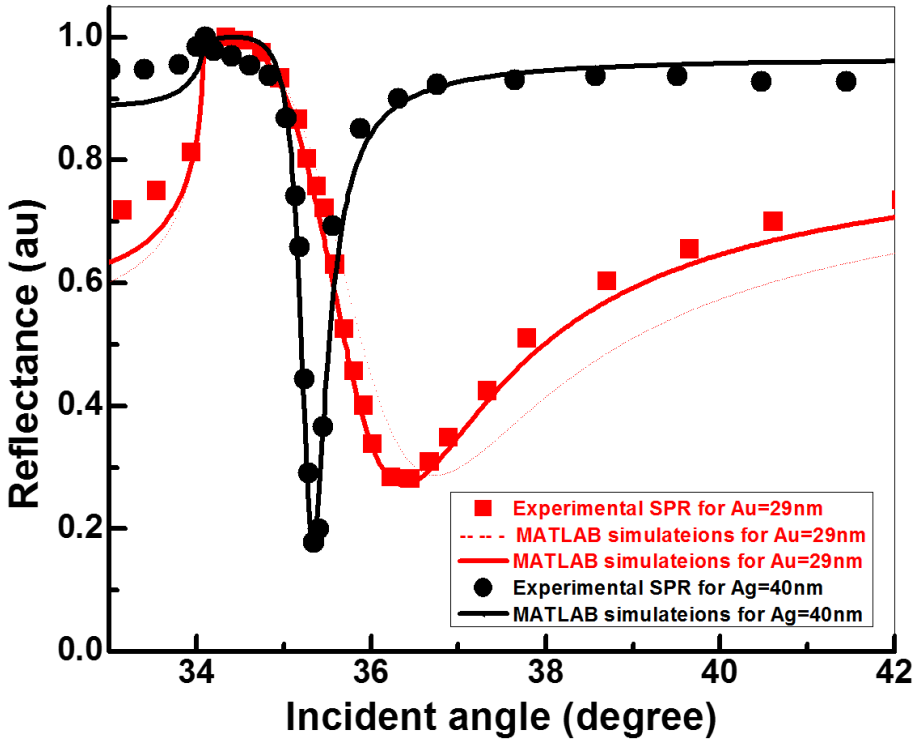

Figure 5.12. Experimental SPR data for sample-1: quartz/29 nm Au, and sample-2: quartz/40 nm Ag. The smooth curves through the data points show MATLAB simulations.

silver film sensor. If we change the complex dielectric constant of gold from (-10.8+i1.47) to (-12.2+i1.47), an equally good agreement between the simulation and the experimental data is obtained.

5.3.2 Bimetallic (Ag/Au) sensor

In order to enhance the sensitivity of SPR sensors using angular interrogation method (prism coupling), the best approach is to narrow down the line-width (FWHM) of reflectivity curve obtained so that a minimal shift in θ_{SPR} could be easily discerned & slope of a tangent to the resonance curve at the lower angle side of attenuation can be made steeper. From our long time interest in noble metallic thin film surfaces & their characterization for SPR sensors, we have been using gold (Au) and silver (Ag) thin films

ranging from 30 to 50nm. Silver is the best choice for use in plasmonic sensors owing to its optical properties, but is limited due to its poor thermal, chemical, mechanical stabilities, and inferior biocompatibility. On the other hand, optical properties of gold are worse than those of silver, but has an excellent environmental durability and biocompatibility. Therefore, a bimetallic (Ag/Au) SPR sensor approach combining both the characteristics has been proposed. An SPR optical biosensor, with a bimetallic silver–gold (Ag/Au) configuration integrates the better evanescent field enhancement of silver, the higher resolution in the reflectivity minimum of silver, and the high chemical resistance of gold.

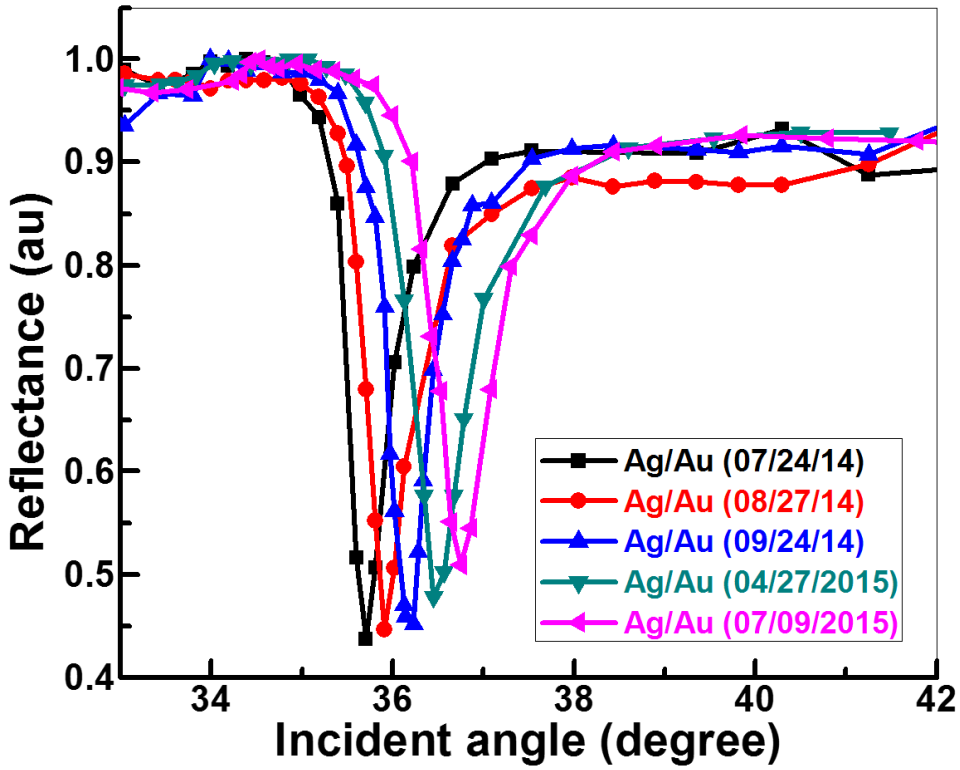

Figure 5. 13 SPR curves of a bimetallic Ag/Au sensor, monitored for its changes due to the aging effects at the bimetallic interface.

For the most efficient/tight coupling of SP modes with the incident photon component along the metal film interface, it is essential that the total thickness of the bi-

metallic film structure be confined within the window of 30nm to 70nm. Also, the effect of Ag to Au ratio is found to be incomparably superior in terms of evanescent field enhancements, than that observed for a simple Au/Ag approach. As the ratio of Ag layer increases, the resonance curve become sharper and the local field near the Au surface is more enhanced [78]. The sensitivity itself is low for a pure Ag film in comparison to a pure Au film based sensor, but it seems to have little influence on the sensing resolution because the narrowest curve width helps the small variation in thin analytes to be resolved. Since the benefit overwhelms the disadvantage, a higher ratio of Ag is likely to give better performance. However, the excessive increase in the ratio of the Ag layer reduces the role of Au as a protective layer, leading to alloying between the Au and Ag layers at the interface, which thereby reduces the stability of the sensor.

Such bimetallic structures benefit from combined advantages of both silver and gold layers. Even-though the SPR characteristics of these bimetallic structures are convincing enough for their candidacy in sensing applications, their usage is limited due to the broad resonance curve produced by the structure and overall instability of the response caused by the reactions at the bimetallic interface. Optical properties (e. g., refractive index) of the interface in such structures are known to undergo significant aging, which could adversely affect sensor performance. We have monitored the SPR characteristics of such bimetallic sensors over extended periods of weeks to months (almost a year) in order to investigate possible aging effects on SPR curves. For the aging measurements, we fabricated a Quartz/35 nm Ag/28 nm Au structure and carried out optical measurements of the SPR curves over extended periods (as shown in figure 5.13).

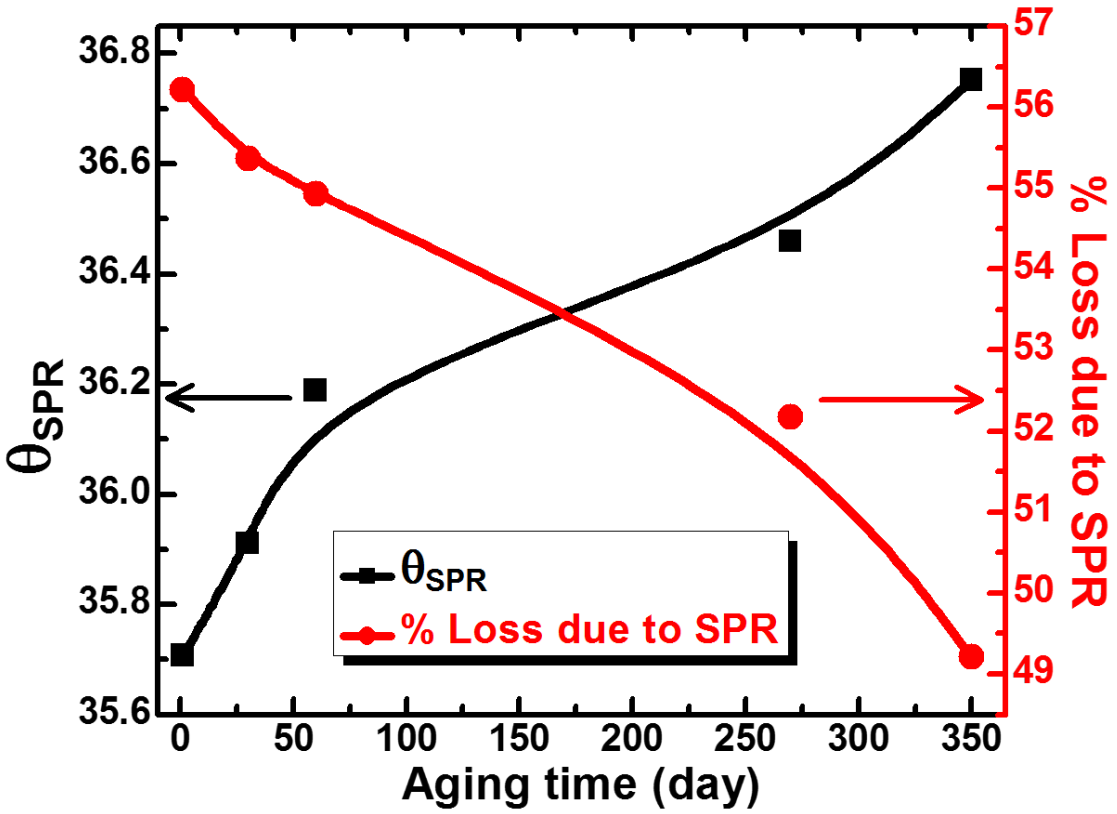

Figure 5.14 Effect of aging at the Ag/Au interface on the SPR sensor characteristics

Our preliminary results show that both the resonance angle (θ_{SPR}) and FWHM of the SPR curves increase with time; over a period of twelve months, the resonance angle shifts to higher angle values and the curves become broader. The sensor seems to degrade due to aging effects. The change in SPR angle and % loss in reflectivity due to the excitation of surface plasmons, both measured for ambient air, are plotted against the age of the bimetallic sensor after the date of deposition, as shown in figure 5.14. Upon completion of the analyses of these data, the results will be presented elsewhere. In the meantime, our assertion is supported by Chen et. al., who have experimentally shown that the growth of the silver oxide layer at the gold/silver interface is responsible for aging effect on the performance degradation of such bimetallic structures [38].

5.3.3 Waveguide material selection

The criterion for selecting Si_3N_4 thin film as a material for waveguide has been the vast interest in its applications in the microelectronics and optoelectronics industries. This particular dielectric possesses remarkable properties; for example, high thermal stability, extreme hardness, chemical inertness and good insulating properties, which make it highly desirable for oxidation masks, protection and passivation barrier layers, gate dielectric, etch-stop layer and inter-level insulator. Additionally, silicon nitride thin films are good optical materials since they are transparent from ultraviolet (250 nm) to infrared (900 nm), and exhibit relatively large refractive index, $n = 1.91$ @ $\lambda = 632.8$ nm. The *Nano-Fab* tools for its deposition and characterization are well established and readily available. Therefore silicon nitride films have been widely used in very large scale integration (VLSI) fabrication and processing.

We have investigated effects of two important parameters of thus fabricated sensors, i.e., materials selection (Ag *vs* Au) and thickness of the Ag, Au, and Si_3N_4 layers. In addition to relevant baseline data on two single metal sensors, we present SPR measurements on four additional samples: i) quartz/35-nm-Ag/28-nm-Au bimetallic structure (identified as sample-3), ii) quartz/35-nm-Ag/50-nm-Si_3N_4/28-nm-Au (sample-4), iii) quartz/35-nm-Ag/100-nm-Si_3N_4/28-nm-Au (sample-5), and iv) quartz/35-nm-Ag/150-nm-Si_3N_4/28-nm-Au (sample-6). Our Kretschmann configuration optical system uses $\lambda = 632.8$ nm beam from 10-mW He–Ne laser, high index prism (Edmund optics, N-SF11, n=1.7847 at 632.8nm), silicon detectors mounted on (θ, 2θ) goniometer, and LabView data acquisition software. The relative intensity of the reflected beam is measured

as a function of the incident angle θ_i at the base of the prism. For $\theta_i > \theta_c$ (where θ_c is the critical angle for total internal reflection), the incident beam suffers total internal reflection and its intensity is measured by one of the detectors.

5.3.4 Resolution and sensitivity comparisons for multilayer structures

In order to assess the influence of the Si_3N_4 waveguide thickness on SPR curves, we have made measurements, for ambient air by using samples-4, -5, and -6. In these samples, the thickness of Ag and Au layers are fixed at 35 nm and 28 nm, respectively. The thickness of the Si_3N_4 dielectric however varies from 50 nm for sample-4, to 100 nm for sample-5, to 150 nm for sample-6. The resulting data are shown in figure 5.15. The smooth curves drawn through the data points represent MATLAB simulations for air in

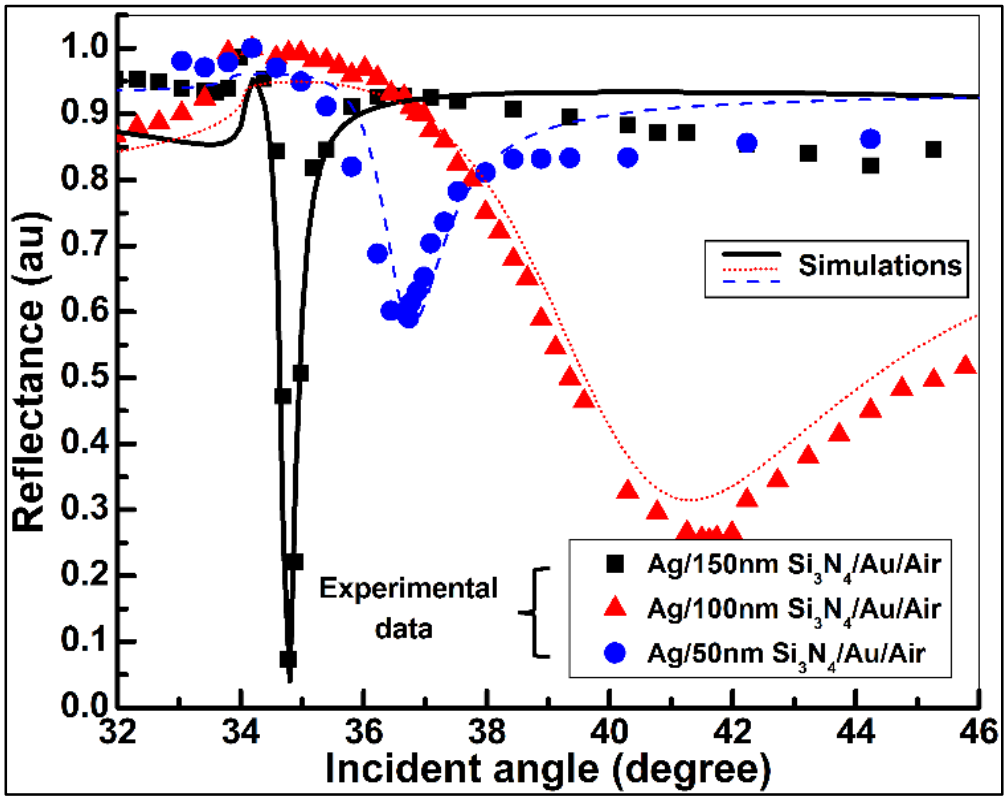

Figure 5.15. SPR curves for air measured using multilayer structures (sample # 4, 5 and 6). The curves represent MATLAB simulations [6].

contact with the outermost Au layer of sample-4, sample-5, and sample-6 (there are no fitting parameters in the simulations, exact values of the refractive indices and thickness were used for each sample). For each one of these samples, there is excellent agreement between SPR measurements and MATLAB simulations. We observe dramatic changes in FWHM and loss of reflectivity at $\theta_i = \theta_{SPR}$. The FWHM changes from approximately 8^0 for sample-5 to 1.5^0 for sample-4 and 0.29^0 for sample-6. The loss in reflectivity at resonance (magnitude of the resonance dip) increases systematically from about 40% for sample-4, to 75% for sample-5, and to 93% for sample-6. Remarkably, our experiments corroborate MATLAB simulations in that the sample with 150 nm thick dielectric exhibits the sharpest resonance (highest resolution) with over 93% loss in reflectivity at θ_{SPR}.

It is logical and desirable to compare the performance of the Bi-WCSPR sensor (sample-6) against the performances of the single-metal and bi-metal sensors (sample-1, sample-2, and sample-3). Figure 5 shows SPR curves measured for air by using sample-1, sample-2, sample-3, and sample-6. The SPR curve for the conventional single layer Au film sensor (sample-1) is the broadest and hence shows the poorest resolution. The SPR curves of the single layer Ag sensor (sample-2) and the bi-metallic sensor (sample-3) are much sharper. The overall performance of the Bi-WCSPR sensor (sample-6), in terms of sharpness and magnitude of the resonance dip, is remarkably superior to the performance of the other five samples studied in this work. For example: (1) the resonance angle θ_{SPR} shifts from about 36.5^0 for the conventional single-layer Au sensor to about 34.7^0 for Bi-WCSPR sample-6. This amounts to having access to much wider dynamic angular range

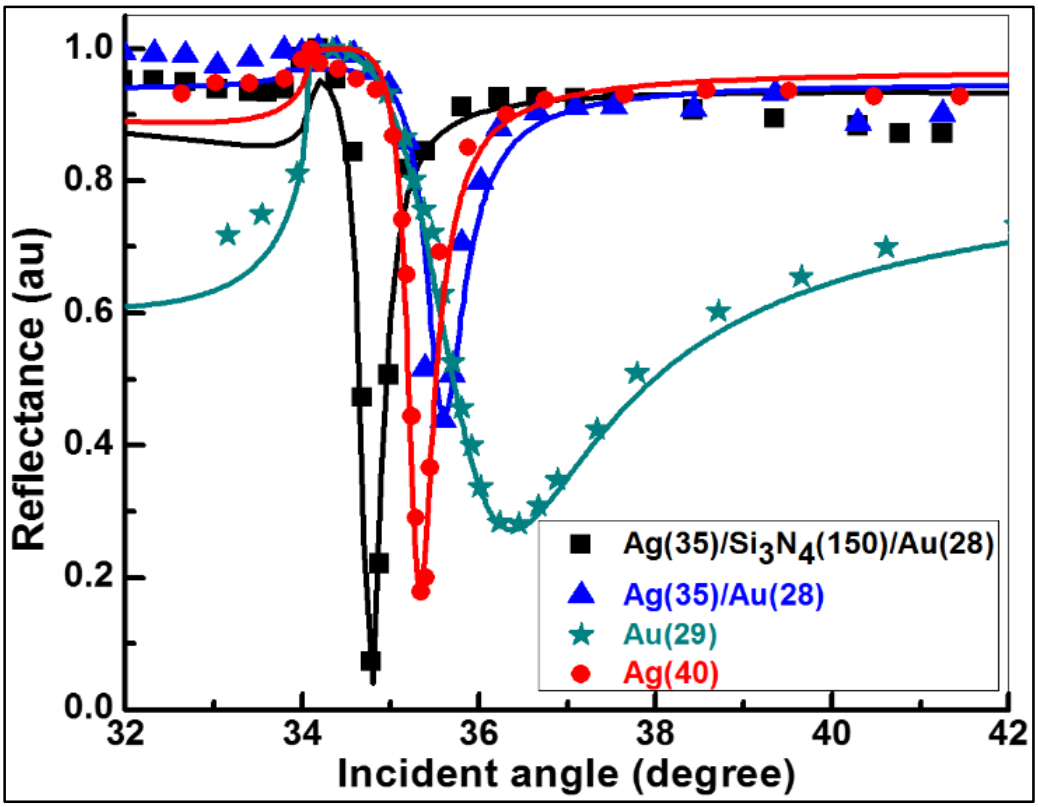

Figure 5.16 Experimental SPR data for sample-1, 2, 3 and 6 for air. Smooth curves represent MATLAB simulations [6].

for sensing applications, (2) the slope of the resonance curve $\left[{}^{\partial R}/_{\partial\theta} = 3.9\right]$ for sample-6 is about 7-times higher than the slope of the resonance curve for sample-1, and (3) being the sharpest (FWHM = 0.29^0), the SPR curve of sample-6 yields a resolution, which is 13 times higher than the resolution of sample-1.

In order to compare the refractive index sensitivities, $S_n = {}^{\partial\theta_{SPR}}/_{\partial n}$ of the single-metal (sample-1) and Bi-WCSPR (sample-6) sensors, we have measured SPR curves for air and distilled water. The resulting data are shown in figure 5.17. In case of sample-6, the resonance angle θ_{SPR} changes from 34.7° (when measured for air) to 51.9° (when measured for water), yielding $S_n = 52\ {}^{\deg ree}/_{RIU}$. Interestingly this exceeds an optimal

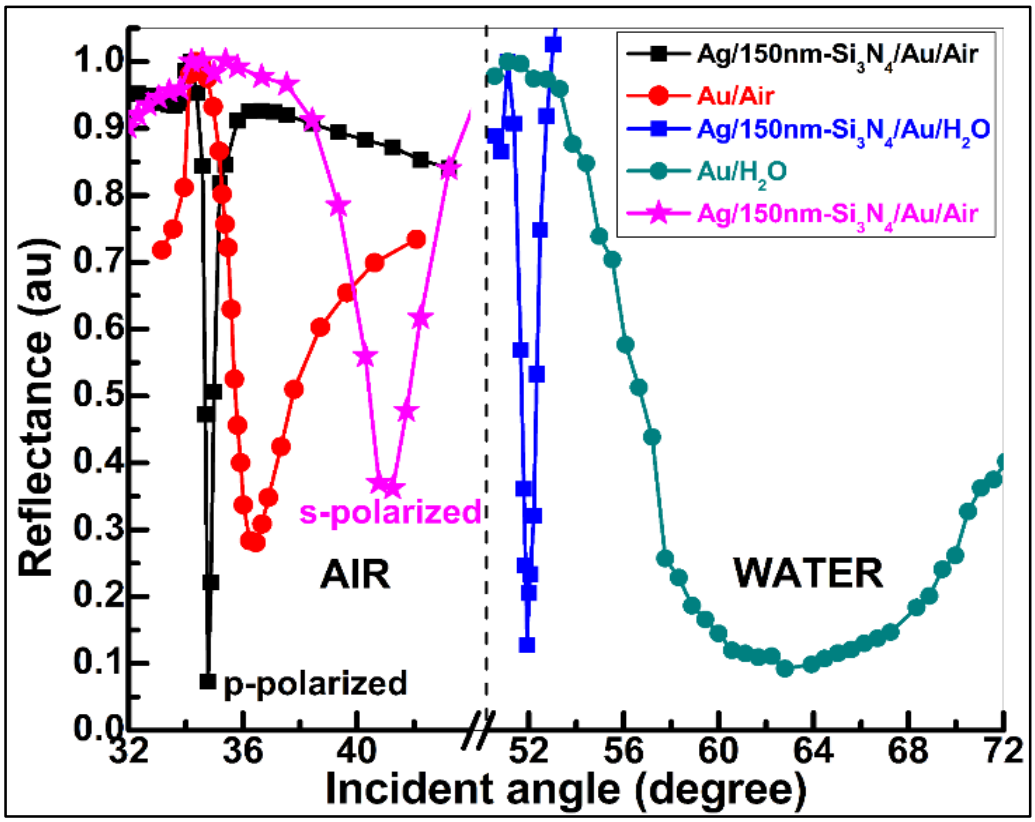

Figure 5.17. Experimental SPR data for air and water using single metal Au and optimized multilayered structure. Smooth curves are drawn to aid the eyes. Notice the high sensitivity of multilayered structure for change in refractive index and also the waveguide mode for s-polarized incident beam [6].

sensitivity of 41.8 obtained from MATLAB simulations. The other characteristics of the resonance curve of sample-6, $^{\partial R}/_{\partial \theta} = 1.324$ and FWHM = 0.86^0, measured for water also exceed MATLAB predicted values of 0.8, and 1.25, respectively. Additionally, in the case of sample-6, the angular separation between the angle at which total internal reflection occurs (θ_{TIR}) and the resonance dip (θ_{SPR}) is only about 0.7^0. In comparison, the value of this angular separation for MATLAB simulations is $\geq 2^0$. The role of the Si_3N_4 dielectric in the multilayer structure used in this work is further accentuated by SPR curves measured using *p*- and *s*-polarized incident beams. In this context, it is known that the resonance excitation of the SPPs and resulting field enhancements due to SPPs coupling with guided

modes in a waveguide occur only with *p*-polarized incident beam. Not only do we see a sharp resonance at 34^0 for *p*-polarized beam, but also see loss in reflectivity at 41^0, which is known to occur only for an *s*-polarized incident beam [42]. The position of the resonance dip changes with the refractive index of the medium only when *p*-polarized incident beam is used. However the position of the dip (41^0), identified with losses in the waveguide and seen only when an *s*-polarized beam is used, does not change with the refractive index of the material in contact with sensor surface. The observation of a dip at 41^0 provides added credence to the fact that the Si_3N_4 dielectric does indeed act as a waveguide in the multilayer structure of sample-6.

5.4 Effects of surface plasmon excitations on photoluminescence by CdSe/ZnS QDs

The CdSe/ZnS core/shell type nanostructures have attracted significant attention because of high quantum yields of their size tunable PL and stability against photo-oxidation. Having learnt the advantages of fixed detector Kretschmann configuration optical system (section 4.1.5) and the high performance SPR sensors (section 5.3), we hereby integrate the two concepts for investigating the effects of strong surface plasmon related fields on the photo-luminescent properties of CdSe/ZnS QDs. We begin by investigating the effect of externally applied ac fields on the PL characteristics of these QDs, and the results from this are considered as a reference data, before understanding the more complicated plasmon-exciton interaction system. The SPR characteristics of the sensor structure employed for this investigation, Ag(35)/Si_3N_4(100)/Au(28), is already established in our recent publication [6].

5.4.1 Calibration of the 1250M JY-Horiba spectrometer

For the simultaneous measurements of surface plasmon resonance and its effects on the photo-luminescence emission of QDs, it is necessary to calibrate the spectrometer for the characteristic wavelengths of the three different laser sources. The figure 5.18 shows the nature and the peak position of the He-Ne laser used as a probe beam for the excitation of surface plasmons throughout this investigation. The peak position for this laser source is observed at λ = 632.77 nm with a full-width half maximum (FWHM) of 0.2693 degree. Similarly, figure 5.19 shows the nature and peak position of the Ar-ion laser used as a pump beam for the excitation of photoluminescence from QDs, and figure 5.20 shows the peak position for a 532 nm solid state laser, as a part of calibration.

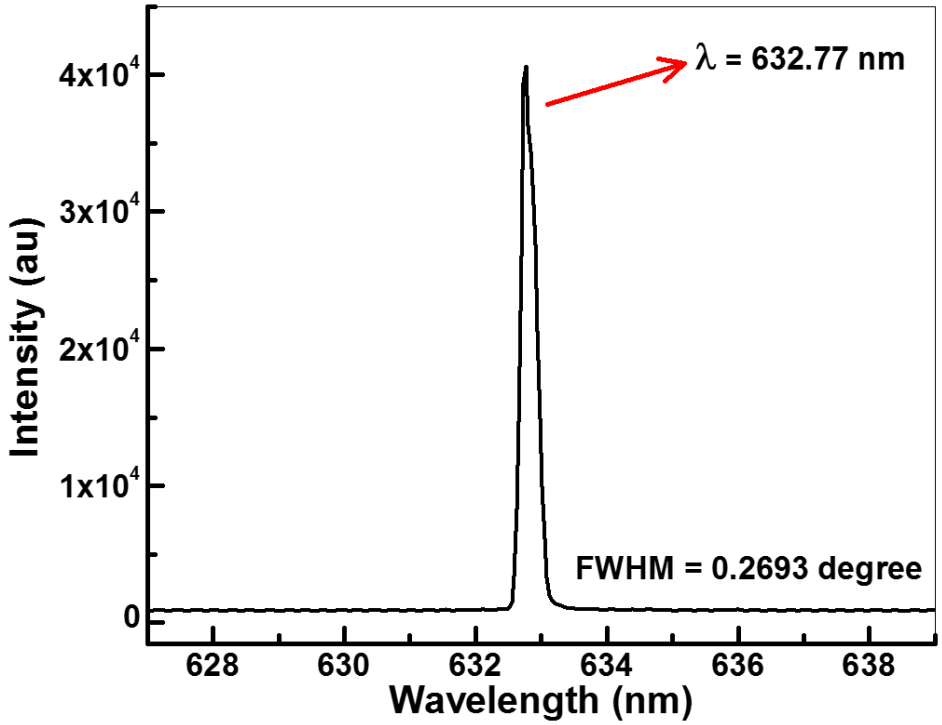

Figure 5.18 Calibration of the spectrometer for He-Ne laser used (λ = 632.8nm).

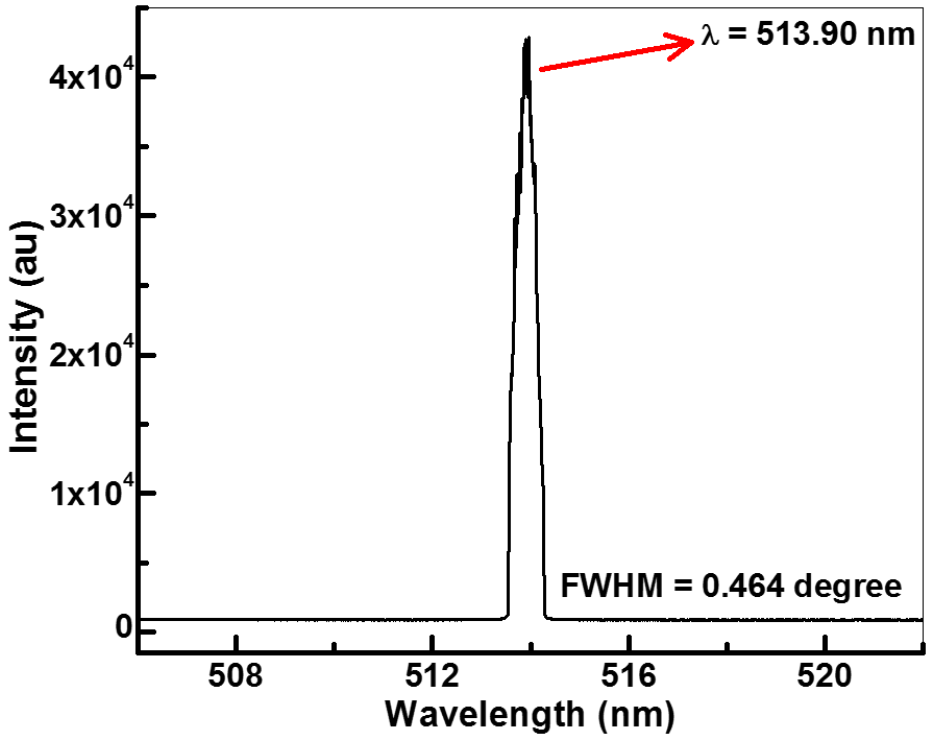

Figure 5.19 Calibration of spectrometer for an Ar-ion laser used (λ = 514 nm).

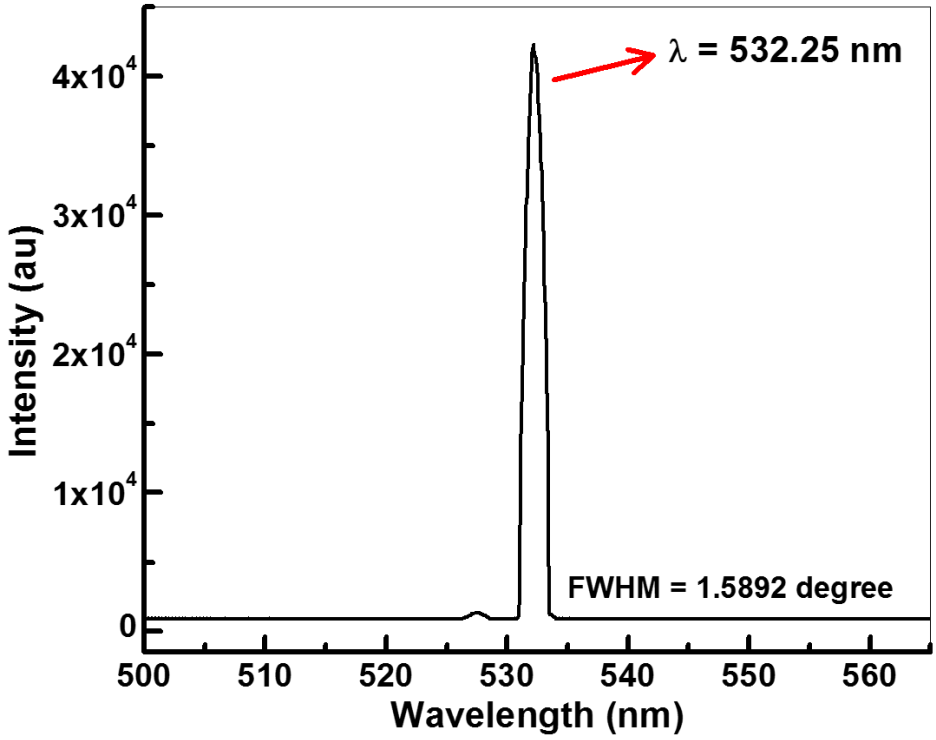

Figure 5.20 Calibration of spectrometer for an solid state laser (λ = 532 nm).

5.4.2 Photoluminescence of CdSe/ZnS QDs

The photoluminescence of CdSe/ZnS QDs coated on the SPR sensor surface, is excited by irradiating the 514 nm water cooled Spectra physics Ar-ion laser (termed as pump beam). The laser power and the spot size of the incident beam are set constant, having values of 0.083 mW and 2 mm, throughout all the set of measurements presented here. The pump beam is known to have very low thermal effects (shown later) on the QD emission at such a low power density of 0.00264 W/cm^2 [79].

Figure 5.21, shows a sample PL curve of the QD thin film coated on the sensor surface, excited by the Ar-ion laser. For each of the measured PL curve, the spectrometer was made to collect the PL emission signals for 60 seconds and 3 accumulations, in order to get a better averaging of the data collected and elimination of background noise (cosmic signals). All the PL spectrum collected in this investigation were analyzed by fitting a smooth Gaussian curve through the data points, using the non-linear square fit tool in Origin-Pro. Figure 5.21 shows a typical data of the PL emission from these QDs and the methodology of peak analysis done throughout this investigation. As seen in figure 5.21, the PL curve for the CdSe/ZnS QDs has its emission peak position centered at 618.8 nm with a FWHM of 29.74 nm. The parameters of the Gaussian curve fitted over the sample PL spectrum is also tabulated as shown in figure 5.22.

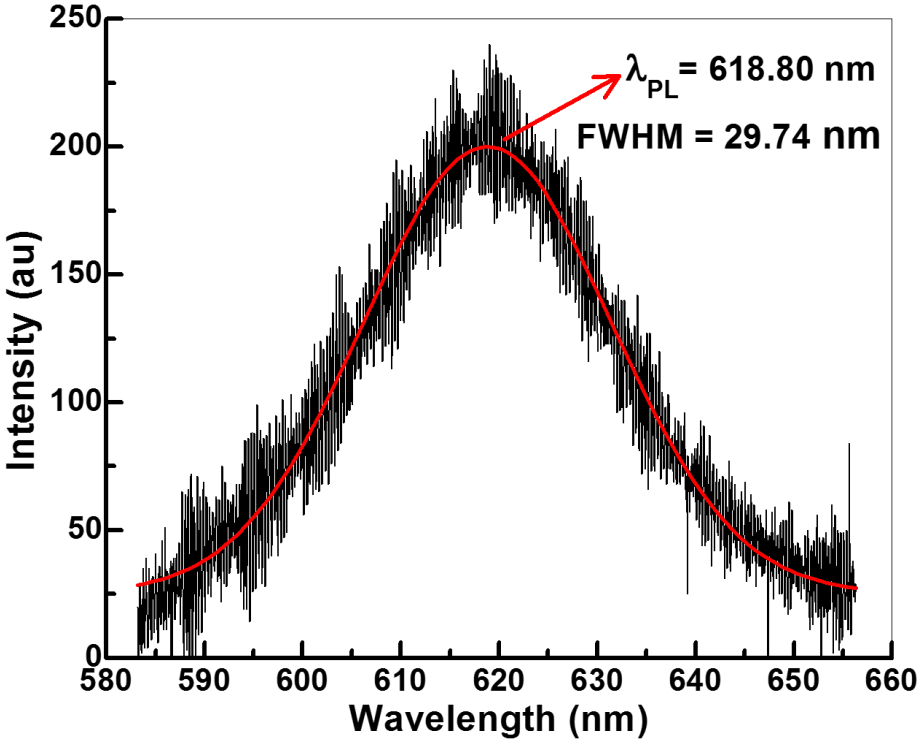

Figure 5.21. Nature and peak position of the PL from CdSe/ZnS QDs.

Equation	y=y0 + (A/(w*sqrt(PI/2)))*exp(-2*((x-xc)/w)^2)		
Adj. R-Square	0.93363		
		Value	Standard Error
Math Y1	y0	25.2563	0.99676
Math Y1	xc	618.80415	0.06598
Math Y1	w	25.26049	0.23157
Math Y1	A	5532.69736	69.92545
Math Y1	sigma	12.63025	
Math Y1	FWHM	29.74196	
Math Y1	Height	174.75723	

Figure 5.22 Fit parameters of the Gaussian curve over PL data.

5.4.3 Temporal evolution of PL from QDs

A set of PL spectra of the QDs, irradiated by the 514 nm Ar-ion laser beam with the laser power density of 2.64 W/cm^2 at the 2mm focus spot, for different exposure times were collected. The wavelengths of the PL emission peak observed for this set of measurements are plotted against the time of exposure by the incident laser, as shown in figure 5.28. It is pretty evident from the plotted results, that the PL emission wavelengths (λ_{peak}) are blue-shifted linearly with the irradiation times, although the magnitude of the blue shift is very small. Similar effects in these QDs have been reported in the past from our group [79], wherein a 532 nm laser beam irradiated with a power density of ~100 W/cm^2 for different exposure times, is observed to induce a blue shift of magnitude $\Delta\lambda_{peak}$ ~ 0.75 nm in the PL emission of these QDs. The small blue shift observed in the present

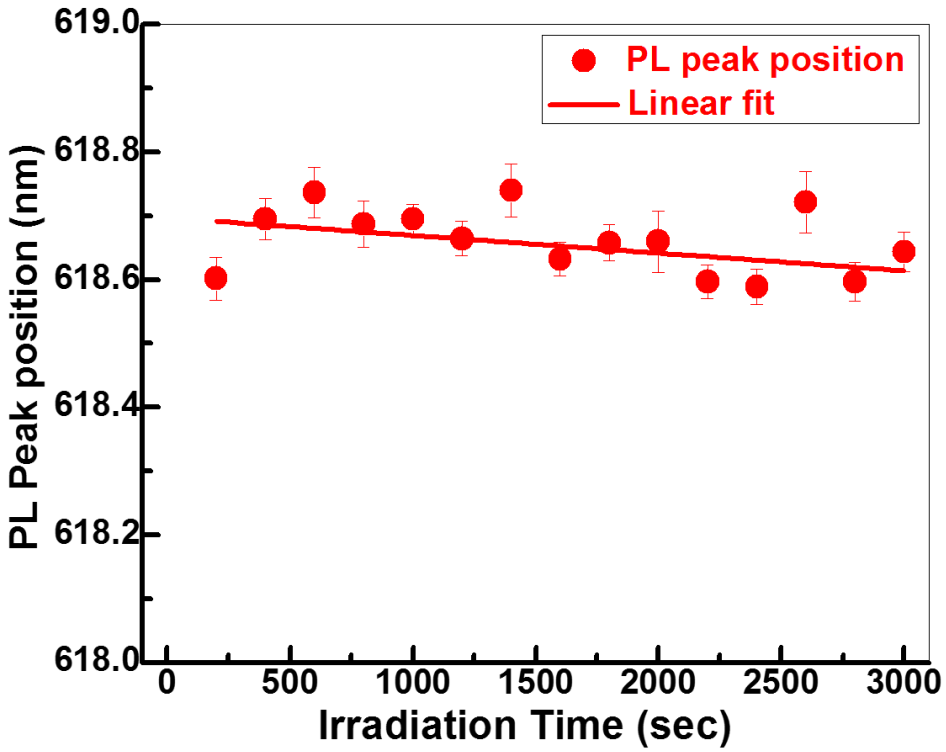

Figure 5.23 PL emission wavelength from CdSe/ZnS QDs as a function of irradiation times.

case, $\Delta\lambda_{peak}$ ~ 0.08 nm, in comparison to our previously reported work could be due to the very low power density of incident laser at the sample spot. Such a linear blue shift in the PL emission of CdSe/ZnS QDs, is known to occur due to the laser irradiation induced electric fields around the excitons in the QDs [79].

5.4.4 PL of QDs in presence of external ac fields

It is significant to understand how the nature of photoluminescence from these semiconducting core-shell quantum dots get affected when placed directly under the influence of externally applied *AC* electric fields at a fixed frequency. The small blue shift observed in case of temporal evolution of PL due to the laser induced electric fields should also be taken into consideration over here. The QD thin film sample preparation and the schematic of the experimental arrangement used for carrying out PL measurements under the influence of externally applied *AC* electric fields, is all described in section 4.1.6. The magnitude of field applied across the QD cell is determined from the SiO_2 spacer beads of diameter ≈10 μm, used to keep the two electrodes insulated from each other.

Figure 5.24 shows the results for the dependence of PL peak wavelengths from these QDs, when measured as a function of ac fields, ranging from 0 to 9 x 10^5 V/m at a fixed frequency of 1 kHz, applied across the QD cell. As observed from the data, the PL peak positions are shifted towards the low wavelengths (blue-shifted) with the increase in the applied ac field across the thin film sample cell (≈10 μm). Due to relatively high magnitude of externally applied ac fields (10^5 V/m), the blue shift observed in this case,

i.e. $\Delta\lambda_{peak}$ ~ 0.61 nm, is significantly enhanced in comparison to the laser induced electric field effects observed in figure 5.24.

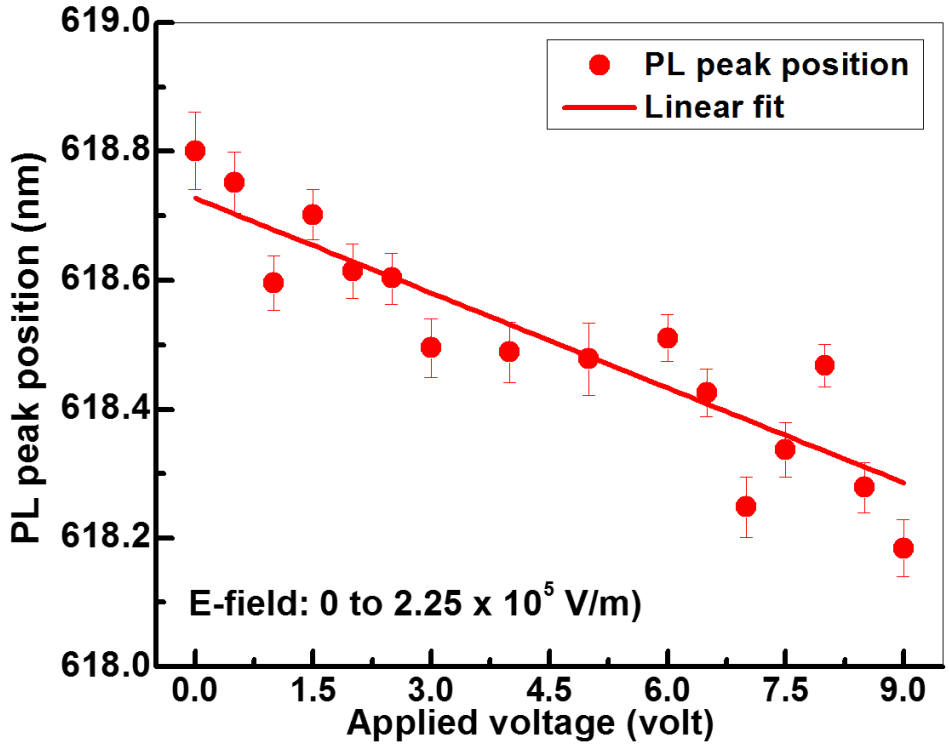

Figure 5.24 Dependence of PL peak position on applied ac fields

The electric field induced blue shift in the two cases, can be supported by the quadratic quantum confinement Stark effect in QDs. The shifts in the electron and the hole quantum well levels in a QD in the interband absorption range under the action of uniform external electric field is known to occur due to the quadratic quantum confinement Stark effect [79]. The blue shift observed in the emission wavelength can then be used to estimate the strength of the irradiation-induced electric fields (in former case), and the externally applied ac fields (in latter case), albeit qualitatively, around the QDs. The detail understanding and theoretical modeling of such a system is yet to be achieved.

5.4.5 SPR measurements for a thin QD film

A very thin film of CdSe/ZnS QD dispersions, coated over the Bi-WC SPR sensor surface is characterized for its SPR response. As mentioned earlier, the reflectivity (SPR) spectrum in all the results are normalized by the incident beam intensity, and each data point is averaged from 100 samplings with a 100 ms integration time between them. Also, the SPR measurement carried out by using the fixed detector system is in close agreement with that of rotating detector system, and so the predictions made by MATLAB simulations for this sensor structure can be readily extended for the experimental results observed on this system.

The refractive index n of such a thin film of QD dispersions, related to the density and polarizability of the given material, is known to increase with increasing the film thickness [80]. In case if the deposited QD film is too thick (more density of QDs), it increases the effective index of the QD layer to such a value that the surface plasmons cannot be excited at Au/QD interface. A QD film, with an optimized thickness for efficient excitation of surface plasmons, was achieved by washing the sensor surface several times with water and chloroform, and measured for its SPR and PL response simultaneously. A separate set of measurements were performed with a mere drop of chloroform (without QDs) on the same sensor structure to confirm that the chloroform itself does not affect the SPR curve in any ways. For the sake of comparison, figure 5.25 shows two sets of SPR curves, measured using the fixed detector optical system. The SPR curve measured for ambient air is shown to be in close agreement with the simulated SPR curve for the same sensor structure using MATLAB. The SPR angle observed, $\theta_{SPR} \approx 41.6^{o}$, indicates the

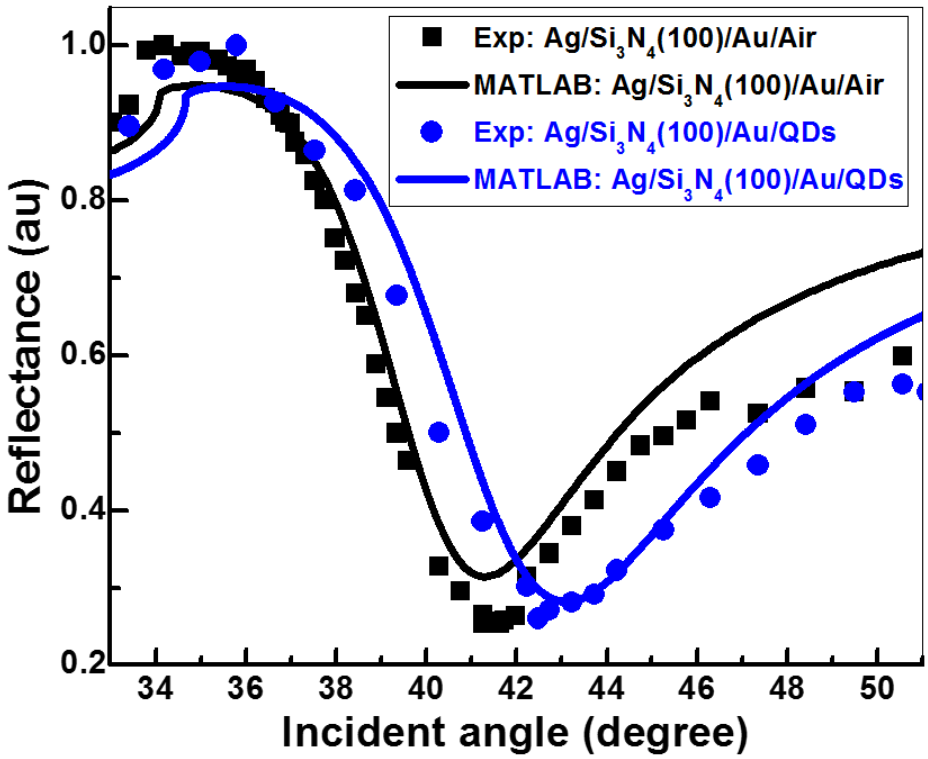

Figure 5.25. SPR measurement of the ambient air in close agreement with the MATLAB simulations. Also, the two experimental curves, with and without QD film, indicating a shift in the SPR angle.

resonant excitation of surface plasmons at the sensor surface, and it can be used to monitor the SPR related effects at the surface. The SPR measurements carried out after coating a thin film of QD dispersions on the sensor surface, is indicated here in blue colored data points. Again, simulations were carried out in order to fit a smooth SPR curve through the experimental data for QD thin film. The small shift in SPR angle $\delta\theta \approx 1.4^{o}$, allows us to calculate the effective refractive index of QD layer through simulations. The simulated SPR curve fits very well with the experimental SPR data measured for the QD film, and the value of refractive index obtained, n = 2.4, is close-by the measured n value of CdSe QDs and ZnS QDs, reported separately by M´arquez et al [80] and Chen et. al [81]. The HR-SEM images collected for these QDs coated on the sensor surface, shows the average

QD particle size distribution of around 125-150 nm. A small shift in the SPR angle, $\delta\theta_{SPR}$ $\approx$ 1.4^{o}, indicates that the thickness of QD film is appropriate enough for the surface plasmons excited at the sensor surface to interact with the coated quantum dots. In other words, the shift in probe beam reflectivity curve (SPR) exhibits an interaction between the QD local dipoles and surface plasmon modes at the sensor surface [81].

5.4.6. PL measurements in presence of surface plasmons (SPs)

In order to investigate the effects of surface plasmons on the PL characteristics of QDs, the full functionality of fixed detector Kretschman configuration optical system for carrying out pump-probe spectroscopic measurements was employed. The SPs are excited at the surface of sensor structure coated with QD film, using a p-polarized probe beam (He-Ne laser). As shown by the probe beam reflectivity curves (with and without QDs) in figure 5.28, the reflected intensity was measured as a function of incident angle at the prism base coupled to the sensor structure. The loss in the reflected intensity at θ_{SPR}, corresponds to resonant excitation of surface plasmons. More loss in reflected intensity means higher value of SP related electric fields. Since the shift in probe beam reflectivity curve (figure 5.28) exhibits an interaction between the QD local dipoles and surface plasmon modes at the sensor surface [81], change in the PL characteristics of these QDs measured in presence of varying intensity of surface plasmon related fields, can exhibit the modulations in the interaction of QD exciton with surface plasmon modes.

The PL measurements of the CdSe/ZnS QD film coated at the sensor surface were carried out simultaneously, for all the angles of excitation of surface plasmons (probe

beam), using the pump-probe spectroscopy technique. The results of these measurements are shown in figure 5.29, with the intensity of PL plotted on the left Y-axis and the PL peak position plotted on the right Y-axis, both as a function of incident angle of probe beam exciting SPs. The laser intensity, beam spot size, and the exact incident position of the pump beam (Ar-ion) exciting PL on the QD film, were all kept constant throughout the SPR measurement (for $\theta = 33^{o}$ to 51^{o} on the base of prism). The position of probe beam spot is carefully monitored through the microscope (as shown in figure 4.6) while changing the angles of excitation of surface plasmons. This arrangement allows us to accurately align the pump and the probe beam at the same spot on both sides of the sensor structure.

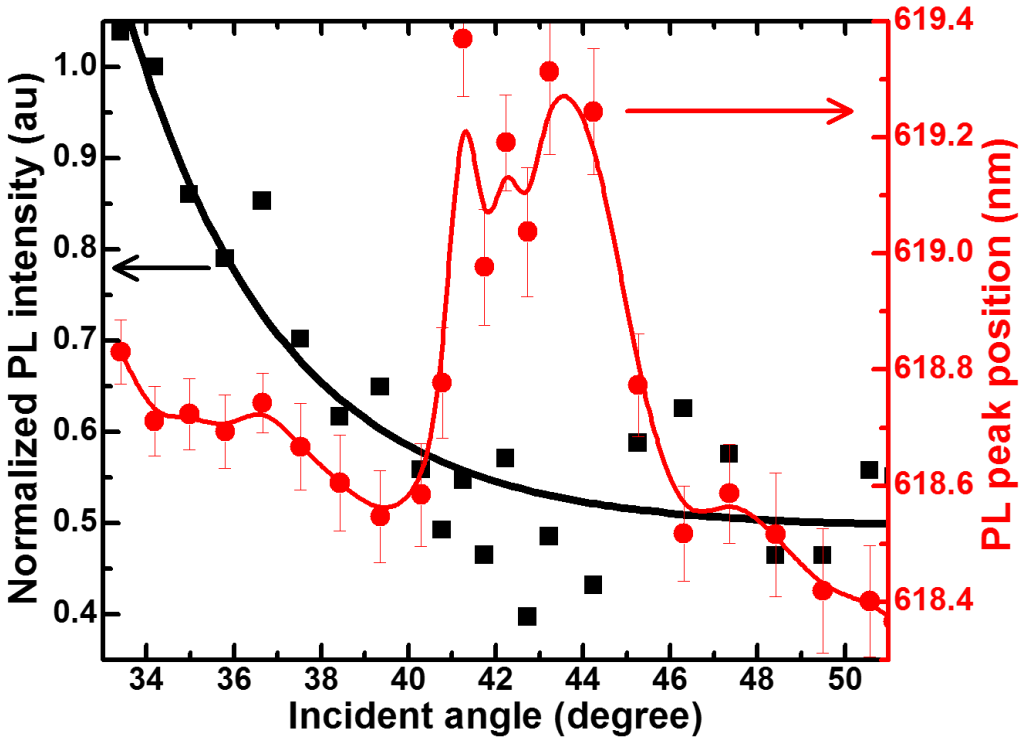

Figure 5.26 PL intensity and peak wavelength position as a function of incident angle of excitation of SPPs.

As observed in the data in figure 5.26, the intensity of PL emission from these QDs coated on the sensor surface, quenches exponentially with the increase in angle of SP excitation. The quenching of PL intensity as a function of SP excitation angle can be again attributed to the increase in the electric field associated with surface plasmons excitation in the vicinity of QD excitons. Whereas, the peak position (wavelength) of the collected PL spectra over the same angles, observes an overall blue shift at all the angles of excitation of probe beam, except where the resonant excitation of SPs are known to occur. At the angles close enough to the resonant excitation of SPs, the wavelength of the emitted PL observes a dramatic red-shift.

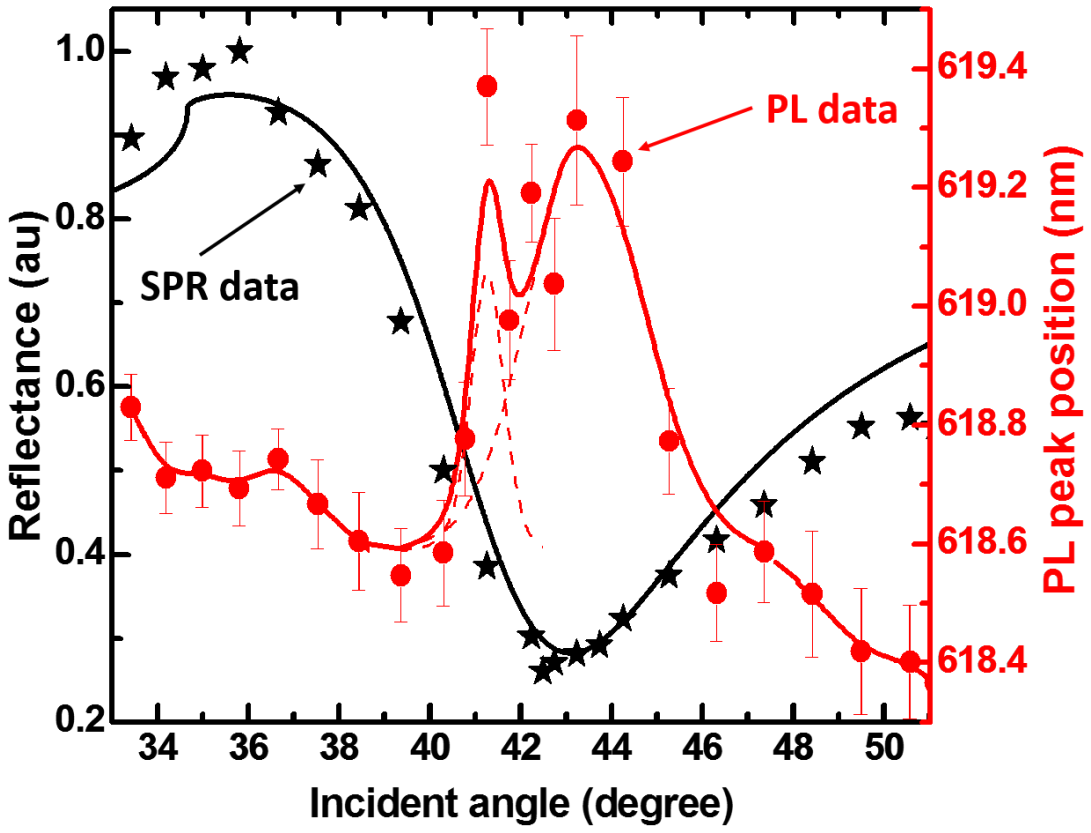

Figure 5. 27 SPR and PL curve for QD thin film coated at the Bi-WC SPR sensor.

The figure 5.27 shows the PL peak position of the collected spectra only, when plotted against the SPR curve of the sensor structure, for one on one comparison between the two effects. The exponential decline in the PL intensity signals the dominance of non-radiative recombination (NR) over the radiative recombination (RR) processes, i.e., competition between PL emission by electron-hole recombination and light induced radiation-less recombination involving either one or combination of several effects, e.g., radiation-less recombination including Auger effect, laser induced electric field quenching of the PL emission, and carrier trapping at defects [79].

The strong coupling between QD molecules and SPs has been interpreted from many different perspectives. The overall effect of strong SP related fields on the PL characteristics of QDs observed in this investigation is intriguing and could be an attribute of one or many competing quantum mechanical phenomena. For instance, Forster resonant energy transfer (FRET), considered as a weak coupling between the donor and the acceptor molecules could be a channel of energy transfer between the donor and acceptor molecule, provided the donor emission and acceptor absorption has to overlap in energy [82]. In a similar manner, plasmon resonant energy transfer (PRET) between the plasmonic nanostructures and fluorescent molecules is another interpretation of strong coupling [83]. In analogy to the FRET, for PRET a match between the plasmon resonance and the electron transition energy of the molecule is needed, whereas the energy is transferred through the dipole-dipole interaction between the resonating plasmon dipole and the molecular dipole. In another case, plasmonic splitting, an analogy to the Rabi splitting, is another perspective

in strong coupling literature [84]. This process can take place because of an exchange of photons between the plasmonic nanoparticle and the fluorescent molecules.

A better understanding of the overall effect of SPs on the PL characteristics of these QDs needs much more work to be done.

Chapter 6

CONCLUSIONS AND FUTURE WORK

In conclusion, we have presented evidence for surface plasmon excitations at Au NPs/LC interfaces in nematic liquid crystal (E44) having relatively small concentrations of 14-nm diameter gold NPs. The evidence is derived from the observations of loss in reflection of p-polarized light at angles greater than the critical angle for total internal reflection from interfaces between a high-index prism and LC composite samples, using the Kretschmann geometry. These findings are important towards understanding the effects of doping polymer-dispersed liquid crystals with Au NPs.

The unique property of the nematic liquid crystalline materials that their dielectric constant can be tuned by externally applied electric fields, has been utilized towards the development of SPR sensor for monitoring changes in the dielectric environment at the metal/dielectric interface. In conclusion, we have carried out series of measurements of the SPR curves for different materials and as functions of applied ac electric field in nematic liquid crystal (E44) by using the Kretschmann configuration system. Both the surface plasmon resonance angle and overall shape of the resonance curve are sensitive to changes in the refractive index of the material at the interface. The baseline sensitivity of the device (high-index prism/30 nm gold/E44/ITO-coated glass), to changes in the refractive index ($\delta\theta_{SPR}/\delta n$) is in excellent agreement with theoretically predicted optimal sensitivity. Remarkably these measurements showed that the sensitivity of the LC based device to changes in the refractive index at the metal/dielectric interface could be as much as (77±3) degree RIU^{-1}, which is an order-of-magnitude higher than sensitivity of another known

similar sensor [$$]. However, the sensitivity of the device to electric field induced changes in the refractive index of the material at the interface ($\delta\theta_{SPR}/\delta E$) is 28-times higher than previously known value for a similar sensor. For fields applied upto 2.5×10^5 V/m, we observe rather large changes in the refractive index of E44 LC, which can be characterized almost equally well, within the statistics of the data, by the Pockels and Kerr effects with coefficients of about 1.85×10^{-7} m/V and 7×10^{-13} m^2/V^2 for the Pockels and Kerr coefficients, respectively. These are extremely large values for the Pockels and Kerr coefficients and they can only be understood by assuming that the local electric field in the material is much larger than the applied field. In fact, our data suggest that the local electric field in our device could be as much as 60-times higher than externally applied fields. We present arguments supporting the possibility of the buildup of such large fields in the device. The high sensitivity of our device to applied ac fields, in conjunction with the observed surface plasmon mediated diffraction from periodic alignment of the liquid crystal on gold surface may facilitate development of highly sensitive opto-electronic sensors for phenomena occurring at metal/dielectric interfaces.

Further to enhance the sensor characteristics of such devices and for more efficient investigation of the events occurring at metal/dielectric interfaces, we have utilized computer simulations and optical measurements to study the performance of bi-metallic (Ag/Au) structures and waveguide-coupled multilayered ($Ag/Si_3N_4/Au$) thin-film structures. The computer simulations were made by using the Transfer Matrix Method in MATLAB and SPR measurements were carried out by using the Kretschmann configuration optical system. Both the simulations and SPR measurements were carried

out as functions of thicknesses of the metal (Ag and Au) and the waveguide dielectric (Si_3N_4). We observe excellent agreement between simulations and experiments for the SPR resonance angle $\left(\theta_{SPR}\right)$, magnitude of the loss-in-reflectivity at resonance, and FWHM of the SPR curves. We have also presented simulations, as well as experiments on sensor sensitivity, resolution, and stability over periods ranging from days to months. A sensor with optimized thickness of Si_3N_4 waveguide (150 nm), sandwiched between 35 nm Ag and 28 nm Au, exhibits the highest sensitivity to changes in the refractive index ($S_n \approx 52^o$/RIU), narrow SPR curve (FWHM $\leq 0.28^0$), yielding high figure-of-merit of (60-180), and extended range of the evanescent fields into the material at the interface, $\delta \approx 305$ nm.

Computational modelling of such multilayered structures for its SPR characteristics can be efficiently achieved using the famous transfer matrix method in MATLAB. Current research involves a parametric investigation of another dielectric material hafnia (HfO_2), for its use as a waveguide media.

With the long decay lengths of the SP related electric fields, it becomes possible to design experiments by which the influence of evanescent fields on materials in contact with the sensor can be examined at such penetration depths. The local optical fields are known to be significantly enhanced in the presence of SP excitations. As an important application of the developed Bi-WCSPR sensor, it is highly desirable to investigate the influence of the strong plasmon fields on the photoluminescence spectra of CdSe/ZnS quantum dots, which would give an approximate idea of the resulting field enhancements. A unique fixed detector Kretschmann configuration optical system is employed for SPR measurements,

which is capable of carrying out *pump-probe* spectroscopy to assess the influence of strong plasmon related fields (excited at the sensor surface) on several other optical properties of materials, e.g., photoluminescence, scattering, surface enhanced RAMAN effect, etc. In this system, neither the prism nor the detector is rotated and the incident angles are scanned simply by steering the incident beam using a translatable stage. Moreover, this also eliminates the inconsistency of the detection efficiency of the detector when measured at different points along the radius of the detector. By eliminating the requirement for $(\theta,2\theta)$ goniometer, this technique simplifies measurements on samples, which, for example, should be maintained under vacuum conditions.

The PL emission from the CdSe/ZnS QDs has been observed in the presence of strong SP related fields, excited at the surface of thus developed Bi-WCSPR structure. The intensity of PL emission signals are found to decrease with the increase in magnitude of the strong electric field associated with surface plasmon, which is attributed to the quadratic quantum confinement Stark effect. The shift in the PL peak wavelength of these QDs is governed by many competing quantum mechanical phenomena controlling the rate of radiative and non-radiative transition processes in such systems. A better understanding of the overall effect of SPs on the PL characteristics of these QDs needs much more work to be done.

REFERENCES

[1] A. Hinojosa and S. C. Sharma, Appl. Phys. Lett. **97**, 081114 (2010).

[2] K. Tiwari, A. K. Singh, and S. C. Sharma, Appl. Phys. Lett. **101**, 253103 (2012).

[3] http://large.stanford.edu/courses/2007/ap272/white1/

[4] H.B. Li, S.P. Xu, Y.J. Gu, K. Wang, W.Q. Xu, Appl. Phys. Lett. **102**, 051107 (2013).

[5] K. Tiwari and S. C. Sharma, Sens. Actuators, A **216**, 128 (2014).

[6] K. Tiwari, S. C. Sharma and N. Hozhabri, J. Appl. Phys. **118**, 093105 (2015).

[7] R. H. Ritchie, Phys. Rev. **106**, 874 (1957)

[8] https://en.wikipedia.org/wiki/Surface_plasmon

[9] http://www.ece.rice.edu/~daniel/262/pdf/lecture10.pdf

[10] J. R. Sambles, G. W. Bradbery and F. Yang, *Contemporary Physics* **32**, 173 (1991)

[11] E. Kretschmann, Z. Phys. **241**, 313 (1971)

[12] A. Otto, Z. Phys. **216**, 398 (1968)

[13] F. Reinitzer, Monatsch. Chem. **9**, 421 (1888).

[14] O. Lehmann, Z. Phys. Chem. **4**, 462 (1889).

[15] E. B. Priestley, P. J. Wojtowiez, and P. Sheng, *Introduction to Liquid Crystals* (Plenum Press, New York, 1975).

[16] B. Bahadur, *Liquid Crystals, Applications and Uses. Vol. 1* (World Scientific, 1990).

[17] I. C. Khoo, *Liquid Crystals*, 2nd Edition (John Wiley & Sons (Interscience), New York, (2007)).

[18] S. J. Woltman, G. D. Jay, G. P. Crawford, *Liquid Crystals, Frontiers in Biomedical Applications*, (World Scientific, New Jersey, (2007)).

[19] P. G. D. Gennes and J. Prost, *The Physics of Liquid Crystals 2nd Ed.* (Oxford University Press, United Kingdom, 1995).

[20] G. Vertogen and W. H. de Jeu, *Thermotropic Liquid Crystals, Fundamentals* (Springer-Verlag, Berlin, 1988).

[21] H. Okamoto, Japanese Journal of Aplied Physics **26**, 315 (1987).

[22] D. S. Chamla and D. A. B. Miller, Journal of Optical Society of America B **2**, 1155 (1985).

[23] R. Rossetti, S. Nakahara, and L. E. Brus, J. Chem. Phys. **79** (2), 1086 (1983).

[24] D. Ioannou, and D. Griffin, Nano Reviews 2010, **1**:5117.

[25] J. Lim, W. K. Bae, J. Kwak, S. Lee, C. Lee, and K. Char, Optical Materials Express **594**, Vol.2, No.5 (2012).

[26] Evident Technologies, Inc.

[27] P. Reiss, M. Protière, and L. Li, *Small* **5**, 154 (2009).

[28] http//cms.uni-konstanz.de/en/physik/leitenstorfer/research/ultrafast-quantum-photonics/quantum-physics-with-single-electron-systems-on-molecular-time-scales/

[29] J. Lia, J. Z. Zhang, *Coordination Chemistry Reviews* **253**, 3015 (2009)

[30] http//micro.magnet.fsu.edu/primer/java/jablonski/lightandcolor/

[31] http//en.wikipedia.org/wiki/Photoluminescence

[32] G. Kloos, *Matrix methods for optical layout* (SPIE Press, Bellingham, Wash., 2007).

[33] M. Born and E. Wolf, *Principles of Optics: Electromagnetic Theory of Propagation, Interference, and Diffraction of Light* (Pergamon Press, Oxford, New York, 1975).

[34] H. Raether, Springer Tr Mod Phys **111**,1-133, (1988).

[35] A. K. Singh and S. C. Sharma, Opt Laser Technol **56**, 256-262, (2014).

[36] C. T. Li, K. C. Lo, H. Y. Chang, H. T. Wu, J. H. Ho, and T. J. Yen, Biosens Bioelectron **36**,192-198, (2012).

[37] B. H. Ong, X. C. Yuan, S. C. Tjin, J. W. Zhang, and H. M. Ng, Sensor Actuat B-Chem **114**,1028-1034, (2006).

[38] X. Chen and K. Jiang, Opt Express **18**,1105-1112, (2010).

[39] D. Sarid, Phys Rev Lett **47**,1927-1930, (1981).

[40] F. Y. Kou and T. Tamir, Opt Lett **12**,367-369, (1987).

[41] K. Matsubara, S. Kawata, and S. Minami, Opt Lett **15**,75-77, (1990).

[42] S. Toyama, N. Doumae, A. Shoji, and Y. Ikariyama, Sensor Actuat B-Chem **65**,32-34, (2000).

[43] A. K. Singh and S. C. Sharma, Opt Laser Technol **56**,256-262, (2014).

[44] Y. S. Ha, H. J. Kim, H. G. Park, and D. S. Seo, Opt. Express **20**, 6448 (2012).

[45] M. Inam, G. Singh, A. M. Biradar, and D. S. Mehta, AIP Adv. **1**, 042162 (2011).

[46] M. Jamil, F. Ahmad, J. T. Rhee, and Y. J. Jeon, Curr. Sci. India **101**, 1544 (2011).

[47] N. Toshima, Macromol. Symp. **304**, 24 (2011).

[48] A. S. Pandey, R. Dhar, S. Kumar, and R. Dabrowski, Liq. Cryst. **38**, 115 (2011).

[49] J. S. Evans, C. N. Beier, and I. I. Smalyukh, J. Appl. Phys. **110**, 033535 (2011).

[50] L. M. Lopatina and J. V. Selinger, Phys. Rev. Lett. **102**, 197802 (2009).

[51] J. W. Doane, A. Golemme, J. L. West, J. B. Whitehead, and B. G. Wu, Mol. Cryst. Liq. Cryst. **165**, 511 (1988).

[52] F. Simoni, Nonlinear Optical Properties of Liquid Crystals and Polymer Dispersed Liquid Crystals (World Scientific, Singapore, 1997), pp. xvii.

[53] S. C. Sharma, Mater. Sci. Eng., B **168**, 5 (2010).

[54] S. Kaur, S. P. Singh, A. M. Biradar, A. Choudhary, and K. Sreenivas, Appl. Phys. Lett. **91**, 023120 (2007).

[55] W. C. Hung, W. H. Cheng, M. S. Tsai, Y. C. Juan, I. M. Jiang, and P. Yeh, Appl. Phys. Lett. **90**, 183115 (2007).

[56] L. A. Holt, R. J. Bushby, S. D. Evans, A. Burgess, and G. Seeley, J. Appl. Phys. **103**, 063712 (2008).

[57] R. A. Innes, S. P. Ashworth, and J. R. Sambles, Phys. Lett. A **135**, 357(1989).

[58] J. Li, G. Baird, Y. H. Lin, H. W. Ren, and S. T. Wu, J. Soc. Inf. Disp. **13**, 1017 (2005).

[59] L. R. Painter, R. D. Birkhoff, and E. T. Arakawa, J. Chem. Phys. **51**, 243 (1969).

[59] D. Coursault, J. Grand, B. Zappone, H. Ayeb, G. Levi, N. Felidj, and E. Lacaze, Adv. Mater. **24**, 1461 (2012).

[60] R. Basu and G. S. Iannacchione, Phys. Rev. E **80**, 010701 (2009).

[61] M. J. Weber, *Handbook of Optical Materials*, CRC Press, Boca Raton, 2003.

[62] S. Roh, T. Chung, B. Lee, Sensors **11**, 1565-1588 (2011).

[63] J. H. Gu, Z. Q. Cao, Q. S. Shen, G. Chen, J. Phys. D: Appl. Phys. **41**, 155309 (2008).

[64] P. B. Johnson, R. W. Christy, Phys. Rev. B **6**, 4370-4379 (1972).

[65] T. S. Lin, C. P. Pang, J. T. Lue, Appl. Phys. B: Lasers Opt. **74**, 401-405 (2002).

[66] R. A. Ramsey, S. C. Sharma, Opt. Lett. **29**, 2237-2239 (2004).

[67] R. A. Ramsey, S. C. Sharma, Opt. Lett. **30**, 592-594 (2005).

[68] R. A. Ramsey, S. C. Sharma, J. Phys. B: Lasers Opt **93**, 481-489 (2008).

[69] R. W. Boyd, *Nonlinear Optics*, Academic Press, Amsterdam, Boston, 2008.

[70] B. E. A. Saleh, M. C. Teich, *Fundamentals of Photonics*, Wiley Interscience, Hoboken, NJ, 2007.

[71] N. Pereda, J. Etxebarria, C. L. Folcia, J. Ortega, C. Artal, M. B. Ros, J. L. Serrano, J. Appl. Phys. **87**, 217-222 (2000).

[72] Y. C. Yang, D. K Yang, Appl. Phys. Lett. **98**, 023502 (2011).

[73] J. Yan, M. Jiao, L. Rao, S. T. Wu, Opt. Express **18**, 11450-11455 (2010).

[74] K. Kneipp, Y. Wang, H. Kneipp, L. T. Perelman, I. Itzkan, R. Dasari, M. S. Feld, Phys. Rev. Lett. **78**, 1667-1670 (1997).

[75] K. R. Li, M. I. Stockman, D. J. Bergman, Phys. Rev. Lett. **91**, 227402 (2003).

[76] H. Choo, M. K. Kim, M. Staffaroni, T. J. Seok, J. Bokor, S. Cabrini, P. J. Schuck, M. C. Wu, E. Yablonovitch, Nat. Photon. **6**, 837-843 (2012).

[77] D. K. Gramotnev, D. F. P. Pile, M. W. Vogel, X. Zhang, Phys. Rev. B **75**, 035431 (2007).

[78] M. Bera, J. Banerjee, and M. Ray, J. Mod. Opt. **61**, 182–196 (2014).

[79] S. C. Sharma, Jay Murphree, T. Chakraborty, Journal of Luminescence, Volume **128**, Issue 11, November 2008, Pages 1771–1776.

[80] E. M´arquez, E. R. Shaaban, and A. M. Abousehly, Int. J. New. Hor. Phys. 1, No. 1, 17-24 (2014).

[81] H. S. Chen, J. Y. Wang, S. S. Yeh, C. D. Chen, H. Y. Lin, Appl. Phys. Lett. **100**, 011102 (2012).

[82] L. Novotny, American Journal of Physics **78** (2010) 1199.

[83] G.L. Liu, Y. Long, Y. Choi, T. Kang, L.P. Lee, Nature Methods. **4** (2007) 1015–1017.

[84] H. Chen, L. Shao, K.C. Woo, J. Wang, H.-Q. Lin, The Journal of Physical Chemistry C. 116 (2012) 14088–14095.

[85] K. M. Chen, Ph.D. dissertation, "Submillisecond-response blue phase liquid crystals for display applications"

[86] E. R. Jette, F. Foote, Journal of Chemical Physics **3**, 605-616 (1935).

[87] R. W. G. Wyckoff, Crystal Structures **1**, 7-83 (1963).

BIOGRAPHICAL INFORMATION

Kunal K. Tiwari was born in Udaipur (Rajasthan, India) but was brought up in Vadodara (Gujarat, India), where he received his Bachelor's degree in Physics (2006) and a Master's degree in Solid State Physics (2008) at the Maharaja Sayajirao University (MSU) of Baroda. His research during the Master's degree was on the experimental studies of Bi-Sb single crystal growth by applying a melt growth technique for obtaining a good quality crystal. After the completion of his Master's degree, Kunal worked as a Teaching Assistant at the M. S. University for a year (2008-2009), to gain some hands on teaching experience.

In Fall 2009, Kunal came to the USA for pursuing doctoral studies at the Physics department of the University of Texas, Arlington. Kunal joined the research group of Dr. Suresh C. Sharma in Fall 2010, where he worked on various projects involving; electro-optic applications of liquid crystals, fabrication & characterization of thin films, surface plasmon resonant sensors, waveguide sensors, and photoluminescence of semiconductor quantum dots. He received a PhD in Physics in December 2015, and wishes to apply his education & interests in the regime of integrated electro-optical devices and sensors.